

3-1-2019

Optical Fiber Communication with Vortex Modes

Du'a Al-Zaleq
University of Wisconsin-Milwaukee

Follow this and additional works at: <https://dc.uwm.edu/etd>



Part of the [Computer Sciences Commons](#), and the [Electrical and Electronics Commons](#)

Recommended Citation

Al-Zaleq, Du'a, "Optical Fiber Communication with Vortex Modes" (2019). *Theses and Dissertations*. 2038.
<https://dc.uwm.edu/etd/2038>

This Dissertation is brought to you for free and open access by UWM Digital Commons. It has been accepted for inclusion in Theses and Dissertations by an authorized administrator of UWM Digital Commons. For more information, please contact scholarlycommunicationteam-group@uwm.edu.

OPTICAL FIBER COMMUNICATION WITH VORTEX MODES

by

Du'a Alzaleq

A Dissertation Submitted in
Partial Fulfillment of the
Requirements for the Degree of

Doctor of Philosophy
in Engineering

at

The University of Wisconsin-Milwaukee

May 2019

ABSTRACT

SPATIAL MULTIPLEXING OF VORTEX MODE

by

Du'a Alzaleq

The University of Wisconsin-Milwaukee, 2019
Under the Supervision of Professor Chiu Law

Internet data traffic's capacity is rapidly reaching limits imposed by optical fiber nonlinearities [5]. Optical vortices appear in high order fiber optical mode. In this thesis, we consider multimode fibers (MMFs) that are capable of transmitting a few vortex modes. Certain types of fibers have a spatial dimension leads to space-division-multiplexing (SDM), where information is transmitted with cores of multicore fibers (MCFs) or mode-division-multiplexing (MDM), where information is transmitted via different modes of multimode fibers (MMFs). SDM by employing few-mode fibers in optical networks is expected to efficiently enhance the capacity and overcome the capacity crunch owing to fast increasing capacity demand. For generation of vortex modes, we investigate computer-generated holograms (CGHs) that are fabricated by interference technique. These components constitute the potential backbone for the high-speed network of the future.

To address the capacity crunch, we study the possibility of applying modes with OAM or helicity in optical fiber communication systems. First, novel fibers (known as vortex fibers) are investigated for their maximum transmission speed and energy guiding capacities. We study the mode properties of these fibers with wave transfer matrix (TMM) method such that the number of guided modes, material and waveguide dispersions are determined. We optimize these fibers by changing their sizes and

structures with various concentrations and types of doping for the index profile. Then an optimized profile is determined for guiding of vortex or higher order modes with a minimum total dispersion and maximum bandwidth to address the capacity crunch. During this process, the waveguide dispersion is computed from numerical results that are applied for generating fitting equations. Similarly, fitting equations are formulated for estimation of number of modes in vortex fibers. Then, the use of computer generated hologram (CGH) technique for encoding vortex modes onto signals is investigated.

TABLE OF CONTENTS

LIST OF FIGURES	VII
LIST OF TABLES	X
LIST OF ACRONYMS	XI
ACKNOWLEDGEMENTS	XII
CHAPTER 1 INTRODUCTION.....	1
1.1 Opticl Fiber Communications	1
1.2 Computer Generated Hologram (CGH)	6
1.3 Research Questions	6
1.4 Research Approach	7
1.5 Thesis Organozation.....	7
CHAPTER 2 LITERATURE REVIEW.....	9
2.1 Maxwell’s Equations.....	9
2.1.1 Derivation of Maxwell Equations	9
2.1.2 Vector Wave equation in Cartesian Coordinates	12
2.1.3 Vector Wave Equation in Cylindrical Coordinates.....	14
2.2 Numerical Implementation using Finite Deference Method.....	16
2.2.1 Finite Difference Scheme.....	16
2.2.2 Eigenvalue Problem	18
CHAPTER 3 GUIDED MODES OF OPTICAL FIBER	24
3.1 Mode Descriptions	24
3.2 Modes in Optical Fibers	26

3.3	Transfer Matrix Method (TMM) for Layered Fiber.....	30
3.4	Numerical Solution Using Transfer Matrix Method.....	32

CHAPTER 4 SIMULATIONS OF MODEL PROPERTIES OF OPTICAL FIBER...41

4.1	Difference between Finite Difference Method and Transfer Matrix Method.....	42
4.2	Number of Guided Modes.....	50
4.3	Dispersions in Optical Fibers	53
4.3.1	Material Dispersion.....	56
4.3.2	Waveguide Dispersion	57
4.3.3	Polarization Mode Dispersion (D_{PMD}).....	58
4.4	Optimizing the Fiber	59
4.4.1	Dispersion -Profile A	66
4.4.2	Dispersion -Profile B.....	67
4.4.3	Dispersion Profile C.....	68
4.5	Bandwidth of Fiber C.....	69

CHAPTER 5 COMPUTER GENERATED HOLOGRAM..... 70

5.1	Computer Generated Hologram (CGH)	70
5.2	Encoding LP_{21} Beam using CGHs Technique	75
5.3	Signal to Noise Ratio (SNR).....	81

CHAPTER 6 PERFORMANCE OF THE VORTEX MODES BESED OPTICAL COMMUNICATION SYSTEM.....84

6.1	Dense Wavelength Division Multiplexing (DWDM) Technique	86
6.2	Mode Coupling.....	86

6.3	Optical Fiber Budget	87
CHAPTER 7 CONCLUSION.....		89
7.1	Conclusion.....	89
7.2	Future Work	90
REFERENCES.....		92
CURRICULUM VITAE.....		96

LIST OF FIGURES

1.1 North American internet traffic.	2
1.2 Data transmission capacity of fiber transmission systems as a function of year.	3
1.3 Nonlinear capacity curves for a range of transmission distances.	4
1.4 Different types of fibers to increase the network capacity.	5
1.5 Example of conversion between LG_{00} and higher order LG_{10} beam using a spiral phase plate.....	6
3.1 Standard step-index fiber geometry.....	29
3.2 An optical microscope image of the end facet of the vortex fiber dk11OD100.....	31
3.3 Measured refractive index profiles for the fiber dk11OD100 and dk11OD1160.....	31
3.4 Measured and Approximated profile for the fiber dk11OD160..	33
4.1 Vortex fiber refractive index profile from experiment and its approximation where the difference in index Δn is calculated with respect to the refractive index of silica $n_{SiO_2}=1.444$	43
4.2 Error between the structure of Vortex profile and it's Approximated.....	44
4.3 Effective index of the Approximated Profile with 5 layers..	45
4.4 Field distribution for LP_{01} , LP_{11} and LP_{21} modes..	45
4.5 Difference among simulated fields from vector and scalar wave for LP_{01} , LP_{11} and LP_{21} modes.....	46
4.6 Effective index error between vortex fiber profile and approximated profile..	46
4.7 Effective index of the approximated profile with 20 layers in core region..	47
4.8 Difference between the approximated profile with 6 layers and the one with eight layers.....	48

4.9 Difference between the approximated profile with 15 layers and the one with eighteenlayers.....	49
4.10 Measured and approximated profiles at $\lambda=1.55\mu\text{m}$..	50
4.11 Number of guided modes (Exact M) using Eq. (4.4) and (Approximated M) with approximated profile with 10 layers at $\lambda=1.55\mu\text{m}$..	52
4.12 Error in M using approximated profile with 10 layers at $\lambda=1.55\mu\text{m}$..	52
4.13 Index profile of fiber A, 4-layers step index profile..	60
4.14 Index profile of fiber B, 4-layers index profile with a graded index core...	61
4.15 Index profile of fiber C, 3-layers with a graded index core.....	63
5.1 Diagram of different modes.....	72
5.2 Computer generated holograms for $l=0,1$ and 2 ..	73
5.3 Function $f(a)$ versus a for the type 2 CGH of a LG_{2l}	75
5.4 Phase distribution of type 2 CGH for LG_{2l} beam.....	76
5.5 Intensity of LG_{2l} and intensity distribution of the encoded LG_{2l} beam..	76
5.6 Phase distribution of the type 2 CGH that encodes LP_{21}	77
5.7 Intensity of the LP_{21} beam and its replicate with the type 2 CGH.....	78
5.8 Function $f(a(x,y))$ versus $a(x,y)$ of the type3 CGH for a LG_{2l} beam..	79
5.9 Phase distribution of the type3 CGH for encoding LG_{21} beam.....	79
5.10 Intensity of LG_{21} beam and Intensity of the encoded LG_{21} with the type3 CGH..	80
5.11 Phase distribution of the type3 CGH for encoding the LP_{21} beam.....	80
5.12 Intensity of original LP_{21} beam and intensity of the encoded LP_{21} with type3 .. CGH.....	81

5.13 SNR versus the normalized waist $w_0/\delta x$ for type 2 and 3 CGHs for encoding
LP21 beam..... 82

6.1 System diagram of a multi-channel optical communication system.. 85

LIST OF TABLES

4.1 Ratio between longitudinal and transverse components of the fields.....	44
4.2 Differences among approximated profile at $\lambda=1.55\mu\text{m}$	49
4.3 Coefficient of Sellmeier equation at certain doping concentration of GeO_2 [41,45]..	54
4.4 Refractive indices values with different doping concentrations	55
4.5 Coefficients of Claussius-Mossotti interpolation [46].....	55
4.6 Material dispersion with different concentrations using A, B and C models	57
4.7 Total dispersion in fiber A; $d = [13.9\% \ 0\% \ 19.7\%]$	64
4.8 Total dispersion in fiber A; $d = [13.7\%, \ 0\%, \ 19\%]$	64
4.9 Total dispersion in fiber B; $d = [13.9\% \ 0\% \ 19.7\%]$	64
4.10 Total dispersion in fiber B; $d = [13.7\%, \ 0\%, \ 19\%]$	64
4.11 Total dispersion in fiber C; $d = [13.9\% \ 13.9\% \ 19.7\%]$	64
4.12 Total dispersion in fiber C; $d = [13.7\%, \ 13.7\%, \ 19\%]$	66
4.13 GVD in fiber A, B and C	66
4.14 Calculated and approximated waveguide dispersion for fiber A.....	67
4.15 Calculated and approximated waveguide dispersion for fiber B.....	67
4.16 Calculated and approximated waveguide dispersion for fiber C.....	68
4.17 Constants of waveguide dispersion for fibers A, B and C.....	69
6.1 Losses for the DWDM system	87

LIST OF ACRONYMS AND ABBREVIATIONS

MINTS	Minnesota Internet Traffic Study
AWGN	Additive White Gaussian Noise
SNR	Signal to Noise Ratio
SMF	Single Mode Fiber
WDM	Wavelength Division Multiplexing
TDM	Time Division Multiplexing
SDM	Space-Division-Multiplexing
MCFs	Multicore Fibers
MDM	Mode-Division-Multiplexing
MCVD	Modified Chemical Vapor Deposition
FEM	Finite Element Method
FDM	Finite Difference Method
HOM	Higher Order Mode
CGHs	Computer Generated Holograms
GVD	Group Velocity Dispersion
MMF	Multimode Fiber
PMD	Polarization Mode Dispersion
DWDM	Dense Wavelength Division Multiplexing
OAM	Optical Angular Momentum
LG	Laguerre Gaussian

ACKNOWLEDGEMENTS

First and foremost, I would like to thank my advisor Chiu Law, a professor in Electrical Engineering at UWM. It has been an honor to be his Ph.D. student. He has taught me; how good Electrical Engineers are. I really appreciate all his contributions of time, ideas, encouragement to make my Ph.D. experience productive and stimulating. The joy and enthusiasm he has for his research were motivational for me, even during tough times in the Ph.D. pursuit. I am also thankful for the excellent example he has provided as a successful Electrical Engineer and professor.

I am the most grateful to my brilliant husband: Dr.Suboh Alkushayni, he is currently an assistant professor in the Computer Science and Software Engineering Department at UW-Platteville. There is no way to express how much it meant to me, my greatest thanks must go to him, for his understanding, patience and valuable support to me at all times. I am the happiest wife in the world to have you as my partner for life and to be blessed with a wonderful two boys, Wesam and Muhammad, and two girls Aseel and Hala. I want to say that you have been my best friends and great companions, loved, supported, encouraged, entertained, and helped me get through this journey in the most positive way.

For this dissertation, I would like to thank my thesis and exam committee: Prof.Pashaie, Prof.Hosseini, Prof.Zhang and Prof.El Hajjar for their time, interest, helpful comments and insightful questions.

I deeply thank my parents, Mahmoud Alzaleq and Aishah Alzoubi for their unconditional trust, timely encouragement, and endless patience. It was their generous love that raised me up, they have also been generous with their encouragement despite the long distance between us.

Chapter 1

Introduction

1.1 Optical Fiber Communications

In the last decades, global network traffic increased exponentially, the reason for that is due to the rapid Internet evolution. With the increasing use of voice over IP, video on demand, cloud storage and computing, and the emerging Internet of things, the trends show no sign of decline. Optical fibers are the most important component in modern telecommunications and computer networking because of their high channel capacity. An optical vortex corresponds to a phase singularity that carries orbital angular momentum (OAM) in the light field. They have a variety of applications in optical trapping and tweezing, micromachining, communication and imaging. The laser is a primary light source that can differ from other light sources in terms of coherence. The fundamental mode of a laser has a Gaussian profile. As we see in (Figure 1.1), the internet traffic in Petabytes/month in optical communication networks is steadily increasing by a factor of 100 every decade according to several studies, such as Minnesota Internet Traffic Study (MINTS) and Cisco. The capacity evolution for various generations of communication systems, such as single mode optical fiber, can lead to a 10,000-fold increase in communication speed for the last three decades [11]. The reason for such an increase can be partially attributed to the employment of various multiplexing techniques in wavelength, amplitude, phase, and polarization of light to encode the information [7].

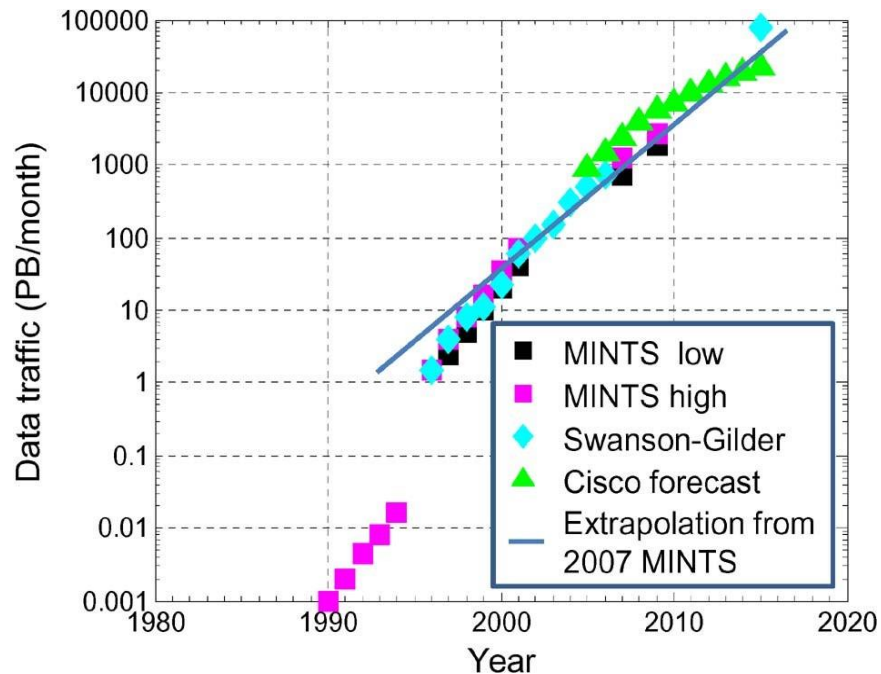


Figure 1.1: North American internet traffic [11]

Owing to the losses caused by impurities in the glass, the first generation of glass optical fibers can have attenuation as high as 200 dB/km at $1\ \mu\text{m}$ [8]. Then researchers in the early 80's developed the single mode fiber (SMF) to reduce the pulse dispersion. In early 90's, they invented the erbium-doped fiber amplifiers, which was the biggest step to improve the capacity in 10 years. At the same time, the development of photodiodes with Indium Gallium Arsenide material enables the adaptation of signal transmission to be focused on the near infrared wavelengths (1550nm) where the optical loss is the lowest, i.e. a window for transmission. (Figure 1.2) shows that the vast improvement in the 2000's was due to the introduction of various modulation formats for the transmission of complex signals, including the encoding information onto the phase of light.

Most of this data traffic is now supported by optical fiber systems. Due to the Internet traffic demand, the capacity of fiber transmission systems also increased exponentially during the last decades. This increase was caused by successive technology improvements: low losses single

mode fibers, fiber amplifiers (EDFAs), wavelength multiplexing (WDM), and high-efficiency spectral coding, as shown in (Figure 1.2). We will have a capacity crunch in a few years since the current systems are reaching the capacity limit, if no new technologies are developed due to the trend for the system's capacity increasing ten times every four years is maintained [11].

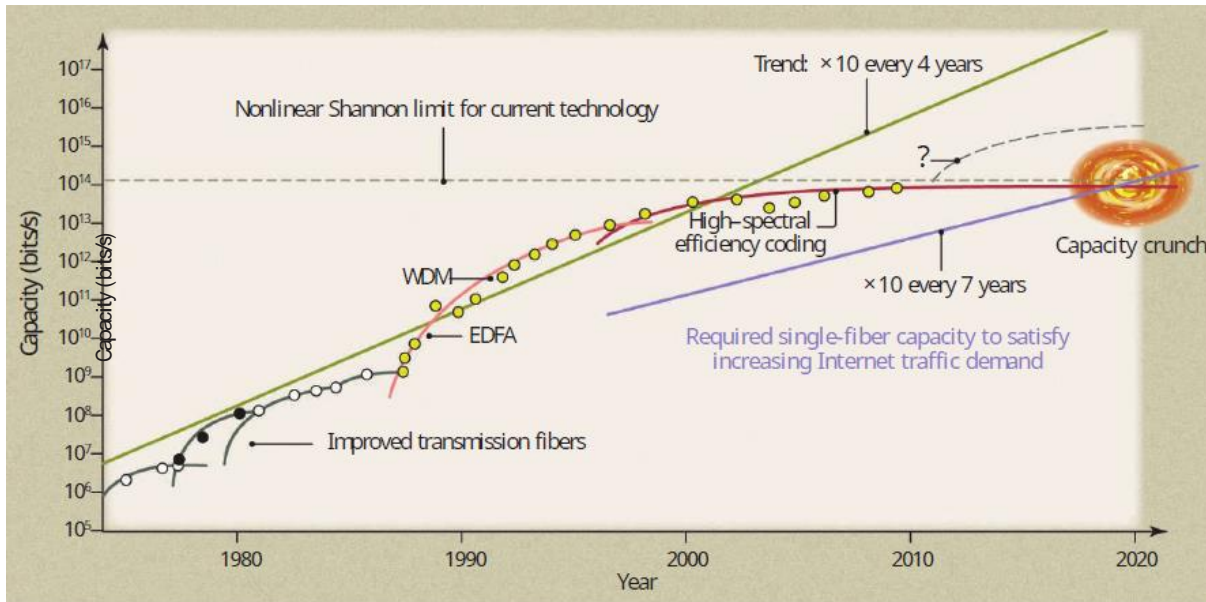


Figure 1.2: Data transmission capacity of fiber transmission systems as a function of year [11]

Typically, there are some limitations for the capacity of a channel [12], e.g. noise which is usually modeled as additive white Gaussian noise (AWGN). It is convenient to characterize a channel in terms of the capacity per unit of bandwidth or spectral efficiency. To get fixed noise level, we should have a higher signal power to get higher spectral efficiency. Based on (Figure 1.3), Shannon limit is the maximum spectral efficiency we can achieve for a given SNR.

In optical fiber channels, it is not that simple to increase the spectral efficiency because optical fibers are nonlinear medium. When the signal power increases, nonlinear effects occur and decrease the spectral efficiency, especially for long the fiber length. The spectral efficiency has

some limitations based on the nonlinear Shannon limit due to the fiber parameters, such as loss coefficient, and effective area. In (Figure 1.3), we can see that as SNR increases, the nonlinear effects dominate on the fiber capacity limit for the capacity curves for different lengths of standard single-mode fiber.

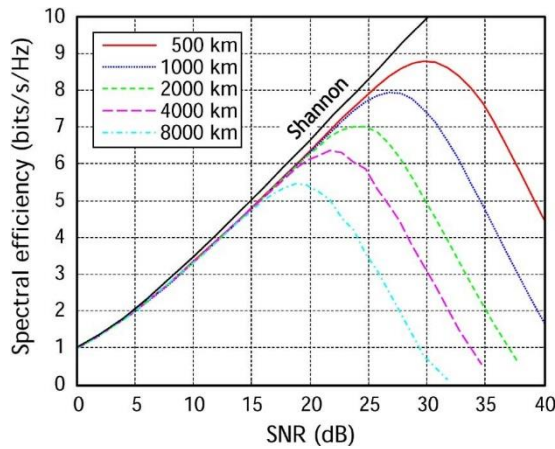


Figure 1.3: Nonlinear capacity curves for a range of transmission distances [10]

To avoid reaching system capacities that are very close to this nonlinear capacity limit and to increase the capacity, we use multiple optical fibers or a new dimension for multiplexing, by fabricating systems with spectral efficiency almost reaching the theoretical limit. In fiber communications, the researchers ran into the limitation of the SMF. The accumulative effect of Kerr nonlinearity in silica renders SMF useless for long-haul multi-channels transmission if meticulous compensation schemes are not implemented owing to the crosstalk (cross-phase modulation) among channels created by the nonlinear refractive index in SMF [9].

This situation can be alleviated by multiplexing optical data, not only in wavelength (WDM), but also in polarization (PDM), in time (TDM), and in phase (quadrature). Hence, the total number of channels is the product of the number of channels in each dimension.

Subsequently, researchers had numerous attempts in developing new fibers to replace SMFs. In one of their approaches, one of the dimensions is space. In space division multiplexing, they explore spatial dimension in the new fibers, such as the transmission of multi-channel information with multicore fibers (MCFs) [12], several modes in few-mode fibers (FMF), or modes in a multimode fiber based on mode-division-multiplexing (MDMs) [13]. (Figure 1.4) below shows different types of optical fibers in communication systems to boost the network capacity.

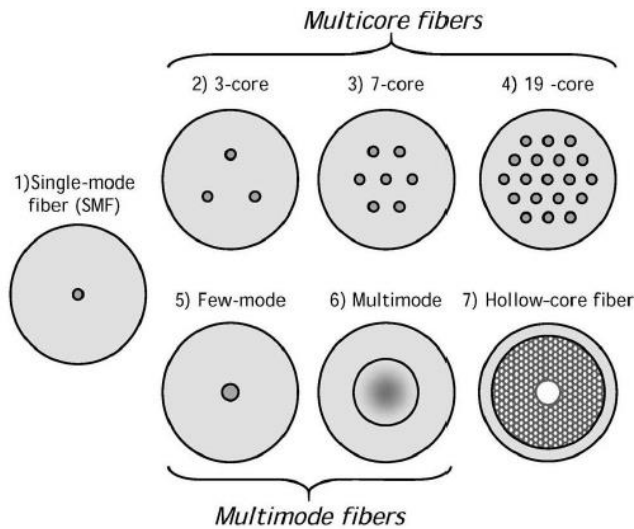


Figure 1.4: Different types of fibers to increase the network capacity. [13]

These new types of fibers have their own limitations based on the structures, e.g. the complicated structure of MCFs requires elaborative manufacturing process. In addition, MMFs suffer from mode coupling caused by both random perturbations in fibers [14] and in modal (de)multiplexers [15].

1.2 Computer Generated Hologram (CGH)

Most of the conventional light sources, coherent or incoherent, emit light in a fundamental mode Laguerre-Gaussian (LG_{00}) beam and conversion to high order modes (HOMs) is needed in order to create an OAM beam. Methods for vortex mode generation include the use of phase plates [22] (see fig 1.5), cylindrical lenses [23], computer-generated holograms [24], fiber gratings [25], q-plates [26] and specialty phase plates [27]. Photons that carry OAM have a helical phase of electric field proportional to $\exp(jl\theta)$, where l is the topological charge, and θ is the azimuthal angle [67]. There are several classical and quantum experiments in free space used the inherent OAM modes by multiplexing information to increase the capacity of free space communications links [68,69].

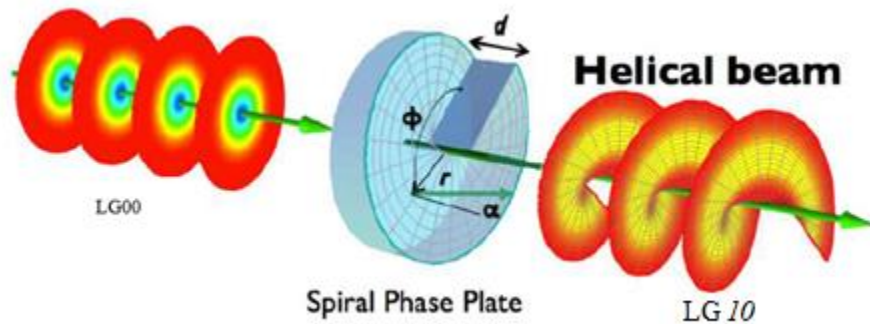


Figure 1.5: Example of conversion between LG_{00} and LG_{10} beams using a spiral phase plate [29]

1.3 Research Questions

In this thesis, we answer the following questions:

- What kind of mode can propagate in those fibers?
- What is the appropriate way in designing the fibers to address the transmission capacity?
- How can we encode LP_{21} mode or other high order modes with the CGH technique?

1.4 Research approach

Based on the fiber, known as vortex fiber) in Ref. 5, we optimize that kind of fiber by finding a profile that can minimize the dispersion and increase the energy mode coupling. We numerically encode the LP_{21} mode with Computer Generated Hologram (CGH) method.

1.5 Thesis Organization

In this thesis, we started with chapter 2, where we studied the mathematical description of MMFs with electromagnetic theory. Then we solved vector wave equation with finite difference method (FDM). In chapter 3, we derived the numerical solution of Helmholtz equations based on transfer matrix method (TMM) for vortex modes.

Chapter 4 we presented the simulations results based on TMM for the vortex fiber in Ref. 5 and compared them with the results from FDM. Then we studied the mode properties of this fiber such that number of guided modes, and various dispersions. Moreover, we presented a fitting equation to predict the number of modes in vortex fibers. We optimized the vortex fiber numerically by changing its size and structure to minimize the GVD value for three different models. Finally, we presented the final profile with a minimum GVD value for the LP_{21} mode. To simplify calculation, we formulated some fitting equations to predict the waveguide dispersion value for LP_{01} , LP_{11} , and LP_{21} modes.

We encode the LP_{21} mode with CGH technique in chapter 5. We presented two types of CGH for encoding the higher order modes (HOMs) i.e LG_{21} and LP_{21} modes. Type 3 CGH is demonstrated to have the best performance for encoding LP_{21} mode. In chapter 6, we presented the performance of optical communication systems based on vortex modes, we considered a dense wavelength

division multiplexing (DWDM) system with vortex mode for transmission of 3.6 Tb/s data over 24 channels and 8 quadrature amplitude modulations (8-QAM).

Chapter 2

Literature Review

2.1 Maxwell's Equations

In this chapter, we look into the mathematical description for multimode fibers. The derivation in this section can be found in many reference books, for instance [17] or [18].

2.1.1 Derivation of Maxwell Equations

A fiber mode is a solution or eigenstates of the waveguide equation. The waveguide equation describes the field distribution of a wave propagating in a fiber under certain boundary conditions.

Electromagnetic fields are governed by Maxwell's equations:

$$\nabla \times \vec{E} = - \frac{\partial \vec{B}}{\partial t} \quad (2.1)$$

$$\nabla \times \vec{H} = \vec{J}_f + \frac{\partial \vec{D}}{\partial t} \quad (2.2)$$

$$\nabla \cdot \vec{D} = \rho_f \quad (2.3)$$

$$\nabla \cdot \vec{B} = 0 \quad (2.4)$$

where \vec{E} is the electric field intensity, \vec{B} is the magnetic flux density, \vec{D} is the electric flux density, \vec{H} is the magnetic field intensity, \vec{J}_f is the free charge current density vector, ρ_f is the free charge density, t is the time, $\nabla \times$ is the curl operator and $\nabla \cdot$ is the divergence operator.

The flux densities \vec{D} and \vec{B} are related to field intensities \vec{E} and \vec{H} by the constitutive relations. For linear and isotropic medium, such as glass, these relations are:

$$\vec{D} = \varepsilon_0 \varepsilon_r \vec{E} \quad (2.5)$$

$$\vec{B} = \mu_0 \mu_r \vec{H} \quad (2.6)$$

where $\varepsilon_0 = 8.85 \times 10^{-12} \text{ Fm}^{-1}$ is the vacuum permittivity, ε_r is the relative permittivity, $\mu_0 = 4\pi \times 10^{-7} \text{ Hm}^{-1}$ is the vacuum permeability, and μ_r is the relative permeability. For glass, it is reasonable to assume:

$$\rho_f = 0 \quad (2.7)$$

$$\vec{J}_f = 0 \quad (2.8)$$

$$\mu_r = 1 \quad (2.9)$$

as glass is non-magnetic and dielectric. Maxwell's equations can then be written as

$$\nabla \times \vec{E} = -\mu_0 \frac{\partial \vec{H}}{\partial t} \quad (2.10)$$

$$\nabla \times \vec{H} = \varepsilon_0 \varepsilon_r \frac{\partial \vec{E}}{\partial t} \quad (2.11)$$

$$\nabla \cdot (\varepsilon_r \vec{E}) = 0 \quad (2.12)$$

$$\nabla \cdot \vec{B} = 0 \quad (2.13)$$

where ε_r is relative permittivity dependent on the frequency. In the following equations, it is assumed that the optical signal is monochromatic with an angular frequency ω . Then the fields can be written as:

$$\vec{E}(\vec{r}, t) = \vec{E}(\vec{r}) \exp(-j\omega t) \quad (2.14)$$

$$\vec{H}(\vec{r}, t) = \vec{H}(\vec{r}) \exp(-j\omega t) \quad (2.15)$$

Here the dependence on the position in space \vec{r} and in time t is written explicitly and $j = \sqrt{-1}$.

Substituting (Eqs. (2.14) - (2.15)) into (Eqs. (2.10) - (2.11)), the Maxwell's equations become:

$$\nabla \times \vec{E}(\vec{r}) = j\omega\mu_0\vec{H}(\vec{r}) \quad (2.16)$$

$$\nabla \times \vec{H}(\vec{r}) = -j\omega\varepsilon_0\varepsilon_r\vec{E}(\vec{r}) \quad (2.17)$$

Taking the curl of the last equation:

$$\nabla \times \nabla \times \vec{H}(\vec{r}) = -j\omega\varepsilon_0\nabla \times (\varepsilon_r(\vec{r})\vec{E}(\vec{r})) \quad (2.18)$$

The following vector identities are used to expand the vector operators:

$$\nabla \times \nabla \times \vec{V}(\vec{r}) = \nabla(\nabla \cdot \vec{V}(\vec{r})) - \nabla^2\vec{V}(\vec{r}) \quad (2.19)$$

$$\nabla \times (\Psi(\vec{r})\vec{V}(\vec{r})) = \Psi(\vec{r})\nabla \times \vec{V}(\vec{r}) + \nabla\Psi(\vec{r}) \times \vec{V}(\vec{r}) \quad (2.20)$$

Here $\vec{V}(\vec{r})$ is a vector and $\Psi(\vec{r})$ is a scalar both dependent on the position in space. With the vector identities, the equation for \vec{H} can be rewritten as:

$$\nabla(\nabla \cdot \vec{H}(\vec{r})) - \nabla^2\vec{H}(\vec{r}) = -j\omega\varepsilon_0(\varepsilon_r(\vec{r})\nabla \times \vec{E}(\vec{r}) + \nabla\varepsilon_r(\vec{r}) \times \vec{E}(\vec{r})) \quad (2.21)$$

It can be further reduced with (Eqs. (2.13) - (2.16)) to:

$$-\nabla^2\vec{H}(\vec{r}) = \omega^2\varepsilon_0\mu_0\varepsilon_r(\vec{r})\vec{H}(\vec{r}) + -j\omega\varepsilon_0\nabla\varepsilon_r(\vec{r}) \times \vec{E}(\vec{r}) \quad (2.22)$$

The last \vec{E} in Eq. (2.22) is eliminated with Eq. (2.17). This gives the following equation:

$$-\nabla^2\vec{H}(\vec{r}) = k_0^2\varepsilon_r(\vec{r})\vec{H}(\vec{r}) + \frac{\nabla\varepsilon_r(\vec{r})}{\varepsilon_r(\vec{r})} \times (\nabla \times \vec{H}(\vec{r})) \quad (2.23)$$

where $c = \frac{1}{\sqrt{\varepsilon_0\mu_0}}$ is the speed of light in vacuum and the wavenumber in vacuum is $k_0 = \frac{\omega}{c}$. The

problem is now given entirely as an equation of \vec{H} . The reason why the problem is not formulated with the \vec{E} can be explained by considering the boundary conditions for the electromagnetic field [19]:

$$E_1^{\parallel} - E_2^{\parallel} = 0 \quad \varepsilon_1 E_1^{\perp} - \varepsilon_2 E_2^{\perp} = \sigma_f \quad (2.24)$$

$$\frac{1}{\mu_1} B_1^{\parallel} - \frac{1}{\mu_2} B_2^{\parallel} = (\vec{K}_f \times \hat{n}_{2 \rightarrow 1}^{\perp})_{\parallel} \quad B_1^{\perp} - B_2^{\perp} = 0 \quad (2.25)$$

Where E^{\perp} , H^{\perp} are the electric and magnetic fields perpendicular to the boundary respectively, E^{\parallel} , H^{\parallel} are the electric and magnetic fields parallel to the boundary respectively, σ_f is the free surface charge density, \vec{K}_f is the free surface current density and $\hat{n}_{2 \rightarrow 1}^{\perp}$ is the normal pointing from medium 2 into medium 1. As it is assumed that there are no free charges and no free currents and $\mu_r = 1$ for both mediums, the boundary conditions for the given problem can be written as:

$$E_1^{\parallel} = E_2^{\parallel} \quad \varepsilon_1 E_1^{\perp} = \varepsilon_2 E_2^{\perp} \quad (2.26)$$

$$H_1^{\parallel} = H_2^{\parallel} \quad H_1^{\perp} = H_2^{\perp} \quad (2.27)$$

It can be seen that \vec{H} is continuous over the interface, and it is, therefore, preferable to solve for \vec{H} and then use Eq. (2.17) to obtain \vec{E} .

2.1.2 Vector wave equation in Cartesian Coordinates

By assuming that a fiber is a straight waveguide and placing the coordinate system such that the fiber is a straight waveguide in the z -direction, then \vec{H} can be written as:

$$\vec{H}(\vec{r}) = \vec{H}(x, y) \exp(j\beta z) \quad (2.28)$$

where β is the propagation constant inside the fiber. Applying this to Eq. (2.23) gives an eigenvalue equation for β^2 :

$$\nabla_{\perp}^2 \vec{H}(x, y) + k_0^2 \varepsilon_r(x, y) \vec{H}(x, y) + \frac{\nabla \varepsilon_r(x, y)}{\varepsilon_r(x, y)} \times (\nabla \times \vec{H}(x, y)) = \beta^2 \vec{H}(x, y) \quad (2.29)$$

where $\nabla_{\perp}^2 = \frac{\partial^2}{\partial x^2} + \frac{\partial^2}{\partial y^2}$ is the transverse Laplacian. Since the fiber is straight, we can assume ε_r is only a function of x and y , we can write the x and the y components of the last term on the left-hand side respectively as:

$$\begin{aligned} [\nabla \varepsilon_r(x, y) \times (\nabla \times \vec{H}(x, y))]_x &= \frac{\partial \varepsilon_r(x, y)}{\partial y} [\nabla \times \vec{H}(x, y)]_z \\ &= \frac{\partial \varepsilon_r(x, y)}{\partial y} \left(\frac{\partial H_y(x, y)}{\partial x} - \frac{\partial H_x(x, y)}{\partial y} \right) \end{aligned} \quad (2.30)$$

$$\begin{aligned} [\nabla \varepsilon_r(x, y) \times (\nabla \times \vec{H}(x, y))]_y &= -\frac{\partial \varepsilon_r(x, y)}{\partial x} [\nabla \times \vec{H}(x, y)]_z \\ &= \frac{\partial \varepsilon_r(x, y)}{\partial x} \left(\frac{\partial H_x(x, y)}{\partial y} - \frac{\partial H_y(x, y)}{\partial x} \right) \end{aligned} \quad (2.31)$$

where the subscript on the square brackets indicates which component to use. It is now possible to write up an equation for the x and the y components of the \vec{H} :

$$\begin{aligned} \nabla_{\perp}^2 H_x(x, y) + \varepsilon_r(x, y) k_0^2 H_x(x, y) + \frac{1}{\varepsilon_r(x, y)} \frac{\partial \varepsilon_r(x, y)}{\partial y} \left(\frac{\partial H_y(x, y)}{\partial x} - \frac{\partial H_x(x, y)}{\partial y} \right) \\ = \beta^2 H_x(x, y) \end{aligned} \quad (2.32)$$

$$\begin{aligned} \nabla_{\perp}^2 H_y(x, y) + \varepsilon_r(x, y) k_0^2 H_y(x, y) + \frac{1}{\varepsilon_r(x, y)} \frac{\partial \varepsilon_r(x, y)}{\partial x} \left(\frac{\partial H_x(x, y)}{\partial y} - \frac{\partial H_y(x, y)}{\partial x} \right) \\ = \beta^2 H_y(x, y) \end{aligned} \quad (2.33)$$

The x and the y components are decoupled from the z component, so it is possible to solve for these components alone. In order to obtain the full solution, it is also necessary to determine the z component. This can be done by invoking that the \vec{H} is divergence free and Eq. (2.13), after applying Eq. (2.28), becomes:

$$\nabla \cdot \vec{H}(\vec{r}) = \frac{\partial H_x(x, y)}{\partial x} + \frac{\partial H_y(x, y)}{\partial y} + j\beta H_z(x, y) = 0 \quad (2.34)$$

$$H_z(x, y) = \frac{j}{\beta} \left[\frac{\partial H_x(x, y)}{\partial x} + \frac{\partial H_y(x, y)}{\partial y} \right] \quad (2.35)$$

With a full solution for the $\vec{H}(\vec{r})$, it is possible to solve for $\vec{E}(\vec{r})$ with Eq. (2.17) and hence obtain the complete solution for the electromagnetic field.

2.1.3 Vector wave equation in Cylindrical Coordinates

For a straight waveguide in the z -direction such as a fiber, its modes assume cylindrical symmetry and it is convenient to use cylindrical coordinates, where $\vec{H}(\vec{r})$ is written as:

$$\vec{H}(\vec{r}) = \vec{H}(\rho, \theta) \exp(j\beta z) \quad (2.36)$$

In cylindrical coordinates, Eq. (2.16) becomes:

$$j\omega\mu_0 H_\rho(\rho, \theta) = -j\beta E_\theta(\rho, \theta) + \frac{1}{\rho} \frac{\partial E_z(\rho, \theta)}{\partial \theta} \quad (2.37)$$

$$j\omega\mu_0 H_\theta(\rho, \theta) = j\beta E_\rho(\rho, \theta) - \frac{\partial E_z(\rho, \theta)}{\partial \rho} \quad (2.38)$$

$$j\omega\mu_0 H_z(\rho, \theta) = -\frac{1}{\rho} \frac{\partial E_\rho(\rho, \theta)}{\partial \theta} + \frac{\partial E_\theta(\rho, \theta)}{\partial \rho} + \frac{1}{\rho} E_\theta(\rho, \theta) \quad (2.39)$$

Also Eq. (2.17) in cylindrical coordinates becomes:

$$-j\omega\varepsilon_0\varepsilon_r E_\rho(\rho, \theta) = -j\beta H_\theta(\rho, \theta) + \frac{1}{\rho} \frac{\partial H_z(\rho, \theta)}{\partial \theta} \quad (2.40)$$

$$-j\omega\varepsilon_0\varepsilon_r E_\theta(\rho, \theta) = j\beta H_\rho(\rho, \theta) - \frac{\partial H_z(\rho, \theta)}{\partial \rho} \quad (2.41)$$

$$-j\omega\varepsilon_0\varepsilon_r E_z(\rho, \theta) = -\frac{1}{\rho} \frac{\partial H_\rho(\rho, \theta)}{\partial \theta} + \frac{\partial H_\theta(\rho, \theta)}{\partial \rho} + \frac{1}{\rho} H_\theta(\rho, \theta) \quad (2.42)$$

The angular part can either be $\cos(l\theta)$ or $\sin(l\theta)$. From Eq. (2.38) it is seen that $H_\rho(\rho, \theta)$ and $E_\theta(\rho, \theta)$ have the same angular dependence e.g. sine and that $E_z(\rho, \theta)$ then has to be cosine. By doing this for all the components of the electromagnetic field, the following relations are obtained:

$$H_\rho(\rho, \theta) \propto \sin(l\theta + a) \quad E_\rho(\rho, \theta) \propto \cos(l\theta + a) \quad (2.43)$$

$$H_\theta(\rho, \theta) \propto \cos(l\theta + a) \quad E_\theta(\rho, \theta) \propto \sin(l\theta + a) \quad (2.44)$$

$$H_z(\rho, \theta) \propto \sin(l\theta + a) \quad E_z(\rho, \theta) \propto \cos(l\theta + a) \quad (2.45)$$

where a is an arbitrary constant. Owing to these observations, $\vec{H}(\rho, \theta)$ can be written as:

$$\vec{H}(\rho, \theta) = H_\rho(\rho) \sin(l\theta) \hat{\rho} + H_\theta(\rho) \cos(l\theta) \hat{\theta} + H_z(\rho) \sin(l\theta) \hat{z} \quad (2.46)$$

where l is the eigenvalue for the angular part, which is a non-negative integer. Now, it is possible to get an equation for the radial component of the $\vec{H}(\rho, \theta)$ from Eq. (2.23) as:

$$\begin{aligned} \frac{\partial^2 H_\rho(\rho)}{\partial \rho^2} + \frac{1}{\rho} \frac{\partial H_\rho(\rho)}{\partial \rho} - \frac{l^2}{\rho^2} H_\rho(\rho) - \frac{1}{\rho^2} H_\rho(\rho) + \frac{2l}{\rho^2} H_\theta(\rho) + \varepsilon_r(\rho) k_0^2 H_\rho(\rho) \\ + \frac{1}{\varepsilon_r(\rho)} \left[\nabla \varepsilon_r(\rho) \times (\nabla \times \vec{H}(\vec{r})) \right]_\rho \frac{\exp(-j\beta z)}{\sin(l\theta)} = \beta^2 H_\rho(\rho) \end{aligned} \quad (2.47)$$

And with the angular component of the \vec{H} given as:

$$\begin{aligned} \frac{\partial^2 H_\theta(\rho)}{\partial \rho^2} + \frac{1}{\rho} \frac{\partial H_\theta(\rho)}{\partial \rho} - \frac{l^2}{\rho^2} H_\theta(\rho) - \frac{1}{\rho^2} H_\theta(\rho) + \frac{2l}{\rho^2} H_\rho(\rho) + \varepsilon_r(\rho) k_0^2 H_\theta(\rho) \\ + \frac{1}{\varepsilon_r(\rho)} \left[\nabla \varepsilon_r(\rho) \times (\nabla \times \vec{H}(\vec{r})) \right]_\theta \frac{\exp(-j\beta z)}{\cos(l\theta)} = \beta^2 H_\theta(\rho) \end{aligned} \quad (2.48)$$

As ε_r only has a ρ dependence, it is possible to express the last term on the left-hand side on (Eqs.

(2.47) - (2.48)) as:

$$\left[\nabla \varepsilon_r(\rho) \times (\nabla \times \vec{H}(\vec{r})) \right]_\rho = 0 \quad (2.49)$$

$$\left[\nabla \varepsilon_r(\rho) \times (\nabla \times \vec{H}(\vec{r})) \right]_\theta \quad (2.50)$$

$$= \frac{\partial \varepsilon_r(\rho)}{\partial \rho} \left[-\frac{\partial H_\theta(\rho)}{\partial \rho} - \frac{1}{\rho} H_\theta(\rho) + \frac{1}{\rho} l H_\rho(\rho) \right] \cos(l\theta) \exp(j\beta z)$$

Hence, (Eqs. (2.47) - (2.48)) can be written as:

$$\begin{aligned} \frac{\partial^2 H_\rho(\rho)}{\partial \rho^2} + \frac{1}{\rho} \frac{\partial H_\rho(\rho)}{\partial \rho} - \frac{l^2}{\rho^2} H_\rho(\rho) - \frac{1}{\rho^2} H_\rho(\rho) + \frac{2l}{\rho^2} H_\theta(\rho) + \varepsilon_r(\rho) k_0^2 H_\rho(\rho) \\ = \beta^2 H_\rho(\rho) \end{aligned} \quad (2.51)$$

$$\begin{aligned} \frac{\partial^2 H_\theta(\rho)}{\partial \rho^2} + \frac{1}{\rho} \frac{\partial H_\theta(\rho)}{\partial \rho} - \frac{l^2}{\rho^2} H_\theta(\rho) - \frac{1}{\rho^2} H_\theta(\rho) + \frac{2l}{\rho^2} H_\rho(\rho) + \varepsilon_r(\rho) k_0^2 H_\theta(\rho) \\ + \frac{1}{\varepsilon_r(\rho)} \frac{\partial \varepsilon_r(\rho)}{\partial \rho} \left[-\frac{\partial H_\theta(\rho)}{\partial \rho} - \frac{1}{\rho} H_\theta(\rho) + \frac{l}{\rho} H_\rho(\rho) \right] = \beta^2 H_\theta(\rho) \end{aligned} \quad (2.52)$$

The ρ and the θ components are decoupled from the z component, so it is possible to solve for these components alone. In order to obtain the full solution, it is also necessary to determine the z component. This can be done by invoking Eq. (2.13):

$$\nabla \cdot \vec{H}(\vec{r}) = \frac{1}{\rho} H_\rho(\vec{r}) + \frac{\partial H_\rho(\vec{r})}{\partial \rho} + \frac{1}{\rho} \frac{\partial H_\theta(\vec{r})}{\partial \theta} + \frac{\partial H_z(\vec{r})}{\partial z} = 0 \quad (2.53)$$

and by inserting Eq. (2.37) into the equation above then it is possible to write:

$$H_z(\rho) = \frac{j}{\beta} \left[\frac{1}{\rho} H_\rho(\rho) + \frac{\partial H_\rho(\rho)}{\partial \rho} - \frac{l}{\rho} H_\theta(\rho) \right] \quad (2.54)$$

With a full solution for the \vec{H} , it is possible to get the full solution for the \vec{E} by using Eq. (2.17) and thereby obtaining a complete solution for the electromagnetic field.

2.2 Numerical Implementation Using Finite Difference Method

Analytical solutions to the differential equations (Eqs. (2.32) - (2.33)) or (Eqs. (2.51) - (2.52)) are only available for a limited number of cases, e.g. the step-index fiber. It is possible to obtain numerical solutions to a wide number of cases. One of the numerical methods is finite difference scheme and the problem can be written as an eigenvalue problem.

2.2.1 Finite Difference Scheme

In the finite difference scheme [29, 30], the spatial domain is divided into an equidistantly spaced grid. As the spacing is finite the derivatives have to be approximated. The first order derivative is approximated as:

$$\frac{\partial H_i(p \Delta\rho)}{\partial\rho} \approx \frac{H_i(\Delta\rho (p + 1)) - H_i(\Delta\rho (p - 1))}{2\Delta\rho} \quad (2.55)$$

where $p=1,2, \dots, p_t$ is the grid point index, p_t is the number of grid points, the spacing is $\Delta\rho$, and the subscript $i = \rho, \theta$ and z indicates the field component. If one expands $H_i(p \Delta\rho)$ in a Taylor series around the p^{th} grid point, then the two neighboring grid points can be written as:

$$H_i((p \pm 1)\Delta\rho) = H_i(p \Delta\rho) + \sum_{n=1}^{\infty} \frac{\partial^n H_i(p \Delta\rho)}{\partial\rho^n} \frac{(\pm\Delta\rho)^n}{n!} \quad (2.56)$$

Subtracting the two neighboring points in the Taylor approximation gives:

$$H_i((p + 1)\Delta\rho) - H_i((p - 1)\Delta\rho) = \frac{\partial H_i(p \Delta\rho)}{\partial\rho} 2\Delta\rho + O(\Delta\rho^3) \quad (2.57)$$

It is seen that the error by doing the approximation of the first order derivative is of the order $(\Delta\rho)^2$ by inserting Eq. (2.57) into Eq. (2.55). The second order derivative can be approximated, in the same manner, as a difference between two first order derivatives:

$$\frac{\partial^2 H_i(p \Delta\rho)}{\partial\rho^2} \approx \frac{\frac{\partial H_i((p + \frac{1}{2})\Delta\rho)}{\partial\rho} - \frac{\partial H_i((p - \frac{1}{2})\Delta\rho)}{\partial\rho}}{\Delta\rho} \quad (2.58)$$

The reason for choosing the non-integer grid point of $p \pm \frac{1}{2}$ will be clear when the approximations of the first order derivatives are made:

$$\frac{\partial H_i((p + \frac{1}{2})\Delta\rho)}{\partial\rho} \approx \frac{H_i((p + 1)\Delta\rho) - H_i(p\Delta\rho)}{\Delta\rho} \quad (2.59)$$

$$\frac{\partial H_i((p - \frac{1}{2})\Delta\rho)}{\partial \rho} \approx \frac{H_i((p \Delta\rho)\Delta\rho) - H_i((p - 1)\Delta\rho)}{\Delta\rho} \quad (2.60)$$

as this will give an estimate for the second order derivative given as:

$$\frac{\partial^2 H_i(p \Delta\rho)}{\partial \rho^2} \approx \frac{H_i((p + 1)\Delta\rho) - 2H_i(p \Delta\rho) + H_i((p - 1)\Delta\rho)}{(\Delta\rho)^2} \quad (2.61)$$

The accuracy of the second order derivative approximation can again be determined by expanding the grid point in a Taylor series around the grid point [30]:

$$\begin{aligned} & H_i((p + 1)\Delta\rho) - 2H_i(p \Delta\rho) + H_i((p - 1)\Delta\rho) \\ &= \left(H_i(p \Delta\rho) + \sum_{n=1}^{\infty} \frac{\partial^n H_i(p \Delta\rho)}{\partial \rho^n} \frac{(\Delta\rho)^n}{n!} \right) - 2H_i(p \Delta\rho) \\ &+ \left(H_i(p \Delta\rho) + \sum_{n=1}^{\infty} \frac{\partial^n H_i(p \Delta\rho)}{\partial \rho^n} \frac{(-\Delta\rho)^n}{n!} \right) \\ &= \frac{\partial^2 H_i(p \Delta\rho)}{\partial \rho^2} (\Delta\rho)^2 + O([\Delta\rho]^4) \end{aligned} \quad (2.62)$$

By inserting Eq. (2.62) into Eq. (2.61), it is seen that the error is of the order $(\Delta\rho)^2$. The consequence of both the first and the second order derivatives to be of the order $(\Delta\rho)^2$ is that the accuracy is improved four times by making $\Delta\rho$ twice as small. This is of course only valid if it is possible to approximate the derivatives by a Taylor series.

2.2.2 Eigenvalue Problem

(Eqs. (2.32) - (2.33)) or (Eqs. (2.51) - (2.52)) define an eigenvalue problem for β^2 . In conjunction with the finite difference scheme, there are two difference equations for each grid point and this can be formulated as a matrix eigenvalue problem:

$$\Phi \mathbf{V} = \beta^2 \mathbf{V} \quad (2.63)$$

where Φ is the matrix operator, also referred to as the discretization matrix for the finite difference problem, which gives the eigenvalue when applied to the eigenvector V . Considering e.g. (Eqs (2.51) - (2.52)), as the method is equivalent to (Eqs. (2.32) - (2.33)), then one way to write the eigenvector is:

$$\mathbf{V} = [H_\rho(\Delta\rho), H_\rho(2\Delta\rho), H_\rho(3\Delta\rho), \dots, H_\rho(p_t \Delta\rho) \quad (2.64)$$

$$H_\theta(\Delta\rho), H_\theta(2\Delta\rho), H_\theta(3\Delta\rho), \dots, H_\theta(p_t \Delta\rho)]^T$$

where p_t is the number of grid point, so the eigenvector has $2p_t$ elements. For example $p_t = 7$,

Then the $2p_t \times 2p_t$ matrix operator can be written as:

$$\Phi = \begin{pmatrix} a_2 & a_3 & 0 & 0 & 0 & 0 & 0 & a_4 & 0 & 0 & 0 & 0 & 0 & 0 \\ a_1 & a_2 & a_3 & 0 & 0 & 0 & 0 & 0 & a_4 & 0 & 0 & 0 & 0 & 0 \\ 0 & a_1 & a_2 & a_3 & 0 & 0 & 0 & 0 & 0 & a_4 & 0 & 0 & 0 & 0 \\ 0 & 0 & a_1 & a_2 & a_3 & 0 & 0 & 0 & 0 & 0 & a_4 & 0 & 0 & 0 \\ 0 & 0 & 0 & a_1 & a_2 & a_3 & 0 & 0 & 0 & 0 & 0 & a_4 & 0 & 0 \\ 0 & 0 & 0 & 0 & a_1 & a_2 & a_3 & 0 & 0 & 0 & 0 & 0 & a_4 & 0 \\ 0 & 0 & 0 & 0 & 0 & a_1 & a_2 & 0 & 0 & 0 & 0 & 0 & 0 & a_4 \\ b_4 & 0 & 0 & 0 & 0 & 0 & 0 & b_2 & b_3 & 0 & 0 & 0 & 0 & 0 \\ 0 & b_4 & 0 & 0 & 0 & 0 & 0 & b_1 & b_2 & b_3 & 0 & 0 & 0 & 0 \\ 0 & 0 & b_4 & 0 & 0 & 0 & 0 & 0 & b_1 & b_2 & b_3 & 0 & 0 & 0 \\ 0 & 0 & 0 & b_4 & 0 & 0 & 0 & 0 & 0 & b_1 & b_2 & b_3 & 0 & 0 \\ 0 & 0 & 0 & 0 & b_4 & 0 & 0 & 0 & 0 & 0 & b_1 & b_2 & b_3 & 0 \\ 0 & 0 & 0 & 0 & 0 & b_4 & 0 & 0 & 0 & 0 & 0 & b_1 & b_2 & b_3 \\ 0 & 0 & 0 & 0 & 0 & 0 & b_4 & 0 & 0 & 0 & 0 & 0 & b_1 & b_2 \end{pmatrix} \quad (2.65)$$

where the non-zero elements are given as:

$$a_1 = \frac{1}{(\Delta\rho)^2} - \frac{1}{p \Delta\rho} - \frac{1}{2\Delta\rho} \quad (2.66)$$

$$a_2 = \frac{-2}{(\Delta\rho)^2} - \frac{l^2}{(p \Delta\rho)^2} - \frac{1}{(p \Delta\rho)^2} + \varepsilon_r (\Delta\rho p) k_0^2 \quad (2.67)$$

$$a_3 = \frac{1}{(\Delta\rho)^2} + \frac{1}{p \Delta\rho} \frac{1}{2\Delta\rho} \quad (2.68)$$

$$a_4 = \frac{2l}{(p \Delta\rho)^2} \quad (2.69)$$

$$b_1 = \frac{1}{(\Delta\rho)^2} - \frac{1}{p \Delta\rho} \frac{1}{2\Delta\rho} \quad (2.70)$$

$$+ \frac{2}{\varepsilon_r \left((p + \frac{1}{2})\Delta\rho \right) + \varepsilon_r \left((p - \frac{1}{2})\Delta\rho \right)} \frac{\varepsilon_r \left((p + \frac{1}{2})\Delta\rho \right) - \varepsilon_r \left((p - \frac{1}{2})\Delta\rho \right)}{\Delta\rho} \frac{1}{2\Delta\rho}$$

$$b_2 = \frac{-2}{(\Delta\rho)^2} - \frac{l^2}{(p \Delta\rho)^2} - \frac{1}{((p-1) \Delta\rho)^2} + \varepsilon_r(p \Delta\rho)k_0^2 \quad (2.71)$$

$$- \frac{1}{\varepsilon_r(p \Delta\rho)} \frac{\varepsilon_r((p+1)\Delta\rho) - \varepsilon_r((p-1)\Delta\rho)}{2\Delta\rho} \frac{1}{p\Delta\rho}$$

$$b_3 = \frac{1}{(\Delta\rho)^2} + \frac{1}{p \Delta\rho} \frac{1}{2\Delta\rho} \quad (2.72)$$

$$- \frac{2}{\varepsilon_r \left((p + \frac{1}{2})\Delta\rho \right) + \varepsilon_r \left((p - \frac{1}{2})\Delta\rho \right)} \frac{\varepsilon_r \left((p + \frac{1}{2})\Delta\rho \right) - \varepsilon_r \left((p - \frac{1}{2})\Delta\rho \right)}{\Delta\rho} \frac{1}{2\Delta\rho}$$

$$b_4 = \frac{2l}{(p \Delta\rho)^2} + \frac{1}{\varepsilon_r(p \Delta\rho)} \frac{\varepsilon_r(p+1)\Delta\rho - \varepsilon_r(p-1)\Delta\rho}{2\Delta\rho} \frac{1}{p\Delta\rho} \quad (2.73)$$

It is worth noting that in Eq. (2.65) the field values at the boundary points are set to zero e.g. the first row reads:

$$a_1 + a_2 H_\rho(\Delta\rho) + a_3 H_\rho(2\Delta\rho) + a_4 H_\theta(\Delta\rho) = \beta^2 H_\rho(\Delta\rho) \quad (2.74)$$

which corresponds to Eq. (2.51) applied to the first grid point. For the last grid point, which is the p_i^{th} row, it looks like:

$$a_1 H_\rho(p_t \Delta\rho) + a_2 H_\rho(p_t \Delta\rho) + a_3 0 + a_4 H_\theta(p_t \Delta\rho) = \beta^2 H_\rho(p_t \Delta\rho) \quad (2.75)$$

The similar boundary equation can be applied to Eq. (2.52). It is fair enough to set the field to zero at the boundary at the last grid point as the field has to go to zero at infinity. The only problem is if the computational domain is not large enough and the field is forced to zero too early, which would result in a non-physical boundary condition. The first grid point requires a little more attention as $\rho = 0$ and at first glance, the differential equations seem to be singular. When $\rho \ll 1$ then (Eqs. (2.51) - (2.52)) reduces to [29]:

$$\frac{\partial^2 H_\rho(\rho)}{\partial \rho^2} + \frac{1}{\rho} \frac{\partial H_\rho(\rho)}{\partial \rho} - \frac{l^2}{\rho^2} H_\rho(\rho) - \frac{1}{\rho^2} H_\rho(\rho) + \frac{2l}{\rho^2} H_\theta(\rho) = 0 \quad (2.76)$$

$$\frac{\partial^2 H_\theta(\rho)}{\partial \rho^2} + \frac{1}{\rho} \frac{\partial H_\theta(\rho)}{\partial \rho} - \frac{l^2}{\rho^2} H_\theta(\rho) - \frac{1}{\rho^2} H_\theta(\rho) + \frac{2l}{\rho^2} H_\rho(\rho) = 0 \quad (2.77)$$

These two equations are identical. The solution for $H_\rho(\rho)$ and $H_\theta(\rho)$ is the same by using the argument that it is possible to decouple the two equations and get a differential equation solely for $H_\rho(\rho)$ and another one solely for $H_\theta(\rho)$, which would be identical. It is then possible to write the two differential equations as one:

$$\frac{\partial^2 H_i(\rho)}{\partial \rho^2} + \frac{1}{\rho} \frac{\partial H_i(\rho)}{\partial \rho} - \frac{l^2}{\rho^2} H_i(\rho) - \frac{1}{\rho^2} H_i(\rho) + \frac{2l}{\rho^2} H_i(\rho) = 0 \quad (2.78)$$

which can be simplified as:

$$\frac{\partial^2 H_i(\rho)}{\partial \rho^2} + \frac{1}{\rho} \frac{\partial H_i(\rho)}{\partial \rho} - \frac{(l-1)^2}{\rho^2} H_i(\rho) = 0 \quad (2.79)$$

The equation with $(l-1)^2$ can be solved with a trial solution, $H_i \propto \rho^q$. Then for $q \geq 2$:

$$q(q - 1) + q - (l - 1)^2 = 0 \quad (2.80)$$

$$q^2 = (l - 1)^2 \quad (2.81)$$

For $q = 1$:

$$1 - (l - 1)^2 = 0 \quad (2.82)$$

$$l = 0 \quad \text{and} \quad l = 2 \quad (2.83)$$

For $q = 0$:

$$-(l - 1)^2 = 0 \quad (2.84)$$

$$l = 1 \quad (2.85)$$

As the physical boundary condition requires the field to be bounded at $\rho = 0$, only real non-negative values of q are valid. It is seen that $m \neq l$ implies that $q > 0$ and the solution actually goes to zero at $\rho = 0$. For $m = l$, then q has to be zero and the field value is a constant at $\rho = 0$ so the first order derivative of H_i is zero.

For the fundamental mode $l = 1$ the field value at $\rho = 0$ is non-zero. The field is symmetric around $\rho = 0$, which also means that the first order derivative is zero and as argued above the field of the two components are identical so it is possible to write (Eqs. (2.51) - (2.52)) in the finite difference scheme as:

$$\frac{H_i(2\Delta\rho) - 2H_i(\Delta\rho) + H_i(0)}{(\Delta\rho)^2} + \varepsilon_r(\Delta\rho)k_0^2 H_i(\Delta\rho) = \beta^2 H_i(\Delta\rho) \quad (2.86)$$

As the field is symmetric around the first grid point $\rho = 0$, then $H_i((i=1)+1) = H_i((i=1) - 1)$ and the equation for $\rho = 0$ becomes:

$$\frac{2H_i(2\Delta\rho) - 2H_i(\Delta\rho)}{(\Delta\rho)^2} + \varepsilon_r(\Delta\rho)k_0^2 H_i(\Delta\rho) = \beta^2 H_i(\Delta\rho) \quad (2.87)$$

$$H(0) = \frac{2H(\Delta\rho)}{\varepsilon_r(0)k_0^2 + \frac{2}{(\Delta\rho)^2}} \quad (2.88)$$

This will modify the non-zero matrix element for the first grid point for both of the components:

$$a_2^{mod} = \frac{2 a_1}{\varepsilon_r(0)k_0^2 + \frac{2}{(\Delta\rho)^2}} + a_2 \quad (2.89)$$

$$a_1 H_\rho(0) + a_2^{mod} H_\rho(\Delta\rho) + a_3 H_\rho(2\Delta\rho) + a_4 H_\theta(\Delta\rho) = \beta^2 H_\rho(\Delta\rho) \quad (2.90)$$

Chapter 3

Guided Modes of Optical Fiber

3.1 Mode Descriptions

In this section, we started with Maxwell equation and we followed the procedure on Ref.17 to derive the wave equation. However, we start from the derivation of step-index fiber, as we use slightly different notation.

As we mentioned before (chapter 2), electromagnetic fields are governed by Maxwell's equations (Eqs. (2.1)-(2.4)). However, within telecommunication wavelengths in the case of silica fibers, we can neglect nonlinear effects and material absorption, without loss of accuracy [37]. Therefore, we assume Eq. (2.5) is:

$$\vec{D} = \epsilon_0 n^2 \vec{E} \quad (3.1)$$

where n is the frequency dependent refractive index of the material. If the material is inhomogeneous, n is also spatial dependent.

The time dependency of the fields is given by:

$$\vec{E} = \vec{E}(\vec{r}, t) = \vec{E}(\vec{r})e^{-j\omega t} \quad (3.2)$$

$$\vec{H} = \vec{H}(\vec{r}, t) = \vec{H}(\vec{r})e^{-j\omega t} \quad (3.3)$$

where \vec{r} is the position vector, ω is the angular frequency, t is time and $\vec{E}(\vec{r})$ and $\vec{H}(\vec{r})$ are the envelopes of a rapidly oscillating signal.

Similar to chapter 2, the wavenumber is $k_0 = \frac{\omega}{c} = \frac{2\pi}{\lambda}$, $\mu_0 \epsilon_0 = \frac{1}{c^2}$ and the free-space impedance

is given by $\eta_0 = \sqrt{\frac{\mu_0}{\epsilon_0}}$.

$$\nabla \times \vec{E} = -\mu_0 \frac{\partial \vec{H}}{\partial t} = j\omega\mu_0 \vec{H}(\vec{r})e^{-j\omega t} = j\eta_0 k_0 \vec{H}(\vec{r})e^{-j\omega t} \quad (3.4)$$

$$\nabla \times \vec{H} = \epsilon_0 \epsilon_r \frac{\partial \vec{E}}{\partial t} = -j\omega\epsilon_0 n^2 \vec{E}(\vec{r})e^{-j\omega t} = -jn^2 \frac{k_0}{\eta_0} \vec{E}(\vec{r})e^{-j\omega t} \quad (3.5)$$

We take the curl of each equation, we obtained:

$$\nabla(\nabla \cdot \vec{E}) - \nabla^2 \vec{E} = [\nabla(jk_0\eta_0) \times \vec{H}(\vec{r}) + jk_0\eta_0 \nabla \times \vec{H}(\vec{r})]e^{-j\omega t} \quad (3.6)$$

$$\nabla(\nabla \cdot \vec{H}) - \nabla^2 \vec{H} = [\nabla\left(-j\frac{k_0}{\eta_0}n^2\right) \times \vec{E}(\vec{r}) - j\frac{k_0}{\eta_0}n^2 \nabla \times \vec{E}(\vec{r})]e^{-j\omega t} \quad (3.7)$$

Using divergence product rule identity:

$$\nabla \cdot (\varphi \mathbf{F}) = (\nabla\varphi) \cdot \mathbf{F} + \varphi(\nabla \cdot \mathbf{F}) \quad (3.8)$$

And since $\nabla \cdot (\epsilon_0 n^2 \vec{E}) = 0$, we got:

$$\nabla \cdot \vec{E} = -\vec{E} \cdot \frac{\nabla n^2}{n^2} \quad (3.9)$$

The gradient of $jk_0\eta_0$ is zero since it does not vary over space. Maxwell's equations (Eqs. (3.6)

- (3.7)) are reduced to:

$$\nabla(\nabla \cdot \vec{E}) - \nabla^2 \vec{E} = jk_0\eta_0 \nabla \times \vec{H}(\vec{r})e^{-j\omega t} \quad (3.10)$$

$$\nabla^2 \vec{H} = j\frac{k_0}{\eta_0} \left(\nabla n^2 \times \vec{E}(\vec{r}) + n^2(\nabla \times \vec{E}(\vec{r})) \right) e^{-j\omega t} \quad (3.11)$$

By substituting (Eqs. (3.4) - (3.5)) into (Eqs. (3.10) - (3.11)), we got the wave equation:

$$\nabla^2 \vec{E}(\vec{r}) + \nabla \left(\vec{E}(\vec{r}) \cdot \frac{\nabla n^2}{n^2} \right) + k_0^2 c_0^2 n^2 \vec{E}(\vec{r}) = 0 \quad (3.12)$$

$$\nabla^2 \vec{H}(\vec{r}) + \frac{\nabla n^2}{n^2} \times \nabla \times \vec{H}(\vec{r}) + k_0^2 c_0^2 n^2 \vec{H}(\vec{r}) = 0 \quad (3.13)$$

3.2 Modes in Optical Fibers

When we study the propagation of light in optical fiber, we can make further simplifications. We assume fiber is perfectly circular, infinitely long, and that the cladding is infinitely thick.

In this chapter, we use cylindrical coordinates (ρ, θ, z) , because the refractive index is only dependent on the ρ coordinate and the fiber is aligned in length along the z -axis. Vector fields in cylindrical coordinates are given by:

$$\vec{E}(\vec{r}) = \vec{E}(\rho, \theta) \exp\{j\beta z\} \quad (3.14)$$

$$\vec{H}(\vec{r}) = \vec{H}(\rho, \theta) \exp\{j\beta z\} \quad (3.15)$$

where β is the propagation constant. Based on that definition of the fields, the $\partial/\partial z$ operator is equivalent to multiplication by $j\beta$. We can rewrite (Eqs. (3.4) - (3.5)) with the determinant operator as:

$$\vec{E}(\rho, \theta) = j\eta_0 \frac{1}{k_0 n^2} \begin{vmatrix} \hat{\rho} & \hat{\theta} & \hat{z} \\ \frac{\partial}{\partial \rho} & 1/\rho (\partial/\partial \theta) & j\beta \\ H_\rho(\rho, \theta) & H_\theta(\rho, \theta) & H_z(\rho, \theta) \end{vmatrix} \quad (3.16)$$

$$\vec{H}(\rho, \theta) = -j \frac{1}{k_0 \eta_0} \begin{vmatrix} \hat{\rho} & \hat{\theta} & \hat{z} \\ \frac{\partial}{\partial \rho} & 1/\rho (\partial/\partial \theta) & j\beta \\ E_\rho(\rho, \theta) & E_\theta(\rho, \theta) & E_z(\rho, \theta) \end{vmatrix} \quad (3.17)$$

Separating the components, this gives:

$$E_\rho(\rho, \theta) = \eta_0 \frac{1}{k_0 n^2} \left(\frac{1}{\rho} \frac{\partial j H_z(\rho, \theta)}{\partial \theta} + \beta H_\theta(\rho, \theta) \right) \quad (3.18)$$

$$E_\theta(\rho, \theta) = -\eta_0 \frac{1}{k_0 n^2} \left(\beta H_\rho(\rho, \theta) + \frac{\partial j H_z(\rho, \theta)}{\partial \rho} \right) \quad (3.19)$$

$$j E_z(\rho, \theta) = -\eta_0 \frac{1}{k_0 n^2 \rho} \left(\frac{\partial(\rho H_\theta(\rho, \theta))}{\partial \rho} - \frac{\partial H_\rho(\rho, \theta)}{\partial \theta} \right) \quad (3.20)$$

$$H_\rho(\rho, \theta) = -\frac{1}{\eta_0} \frac{1}{k_0} \left(\frac{1}{\rho} \frac{\partial j E_z(\rho, \theta)}{\partial \theta} + \beta E_\theta(\rho, \theta) \right) \quad (3.21)$$

$$H_\theta(\rho, \theta) = \frac{1}{\eta_0} \frac{1}{k_0} \left(\beta E_\rho(\rho, \theta) + \frac{\partial j E_z(\rho, \theta)}{\partial \rho} \right) \quad (3.22)$$

$$j H_z(\rho, \theta) = \frac{1}{\eta_0} \frac{1}{k_0 \rho} \left(\frac{\partial(\rho E_\theta(\rho, \theta))}{\partial \rho} - \frac{\partial E_\rho(\rho, \theta)}{\partial \theta} \right) \quad (3.23)$$

Then we can rewrite all transverse components as functions of longitudinal components [17], i.e. transverse fields in ρ ($E_\rho(\rho, \theta)$ and $H_\rho(\rho, \theta)$) and θ ($E_\theta(\rho, \theta)$ and $H_\theta(\rho, \theta)$) directions can be represented in terms of $E_z(\rho, \theta)$ and $H_z(\rho, \theta)$ [35]:

$$E_\rho(\rho, \theta) = \frac{j\beta}{\omega^2 \mu \varepsilon - \beta^2} \left(\frac{\partial}{\partial \rho} E_z(\rho, \theta) + \frac{\omega \mu}{\beta} \frac{\partial}{\rho \partial \theta} H_z(\rho, \theta) \right) \quad (3.24)$$

$$E_\theta(\rho, \theta) = \frac{j\beta}{\omega^2 \mu \varepsilon - \beta^2} \left(\frac{\partial}{\rho \partial \theta} E_z(\rho, \theta) - \frac{\omega \mu}{\beta} \frac{\partial}{\partial \rho} H_z(\rho, \theta) \right) \quad (3.25)$$

$$H_\rho(\rho, \theta) = \frac{j\beta}{\omega^2 \mu \varepsilon - \beta^2} \left(\frac{\partial}{\partial \rho} H_z(\rho, \theta) - \frac{\omega \varepsilon}{\beta} \frac{\partial}{\rho \partial \theta} E_z(\rho, \theta) \right) \quad (3.26)$$

$$H_\theta(\rho, \theta) = \frac{j\beta}{\omega^2 \mu \varepsilon - \beta^2} \left(\frac{\partial}{\rho \partial \theta} H_z(\rho, \theta) + \frac{\omega \varepsilon}{\beta} \frac{\partial}{\partial \rho} E_z(\rho, \theta) \right) \quad (3.27)$$

We see that longitudinal components $E_z(\rho, \theta)$ and $H_z(\rho, \theta)$ are purely imaginary in those equations, while transverse components are real. This convention comes from the definition of the

propagation constant in (Eqs. (3.14) - (3.15)). It shows that longitudinal and transverse components are expressed on an orthogonal basis.

Modes are eigen solutions of the optical waveguide. They are parametrized by two quantities: a non-negative integer l that is the mode order relating to the number of symmetry axes in the azimuthal dependency of the fields. Moreover, a positive integer m that is the radial order relating to the number of zeros in the radial dependency of the fields. Modes could be either *TE* (azimuthal E and radial H field) or *TM* (radial E and azimuthal H field) when the mode is purely radial or purely azimuthal ($l=0$). On the other hand, either *EH* or *HE*, determined by whether the $E_z(\rho, \theta)$ or $H_z(\rho, \theta)$ component is dominant when $l > 0$.

Based on the profile of optical fiber, we can find the modes. In the case of step index fiber (Figure 3.1). We can say, it has 2 layers, the core region with refractive index n_{co} and radius ρ_1 and the cladding region with refractive index n_{cl} . We can say the radius in the cladding region to be infinite since its refractive index does not vary with position. Therefore, $\nabla n^2 = 0$, and the wave equations (Eqs. (3.12) - (3.13)) take the form of Helmholtz equations:

$$\left[\nabla_t^2 + (\omega^2 \mu \epsilon - \beta^2) \right] \begin{Bmatrix} \bar{E}_z(\rho, \theta) \\ \bar{H}_z(\rho, \theta) \end{Bmatrix} = 0 \quad (3.28)$$

where $\nabla_t^2 = \frac{\partial^2}{\partial \rho^2} + \frac{1}{\rho} \frac{\partial}{\partial \rho} + \frac{1}{\rho^2} \frac{\partial^2}{\partial \theta^2}$ is the transverse Laplacian operator.

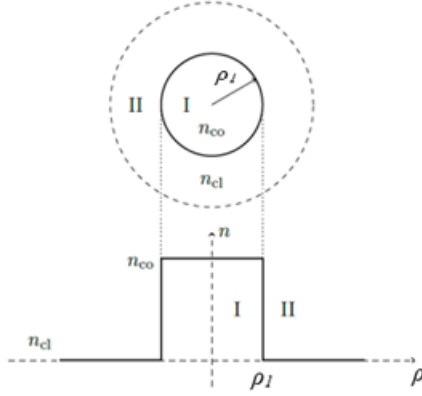


Figure 3.1: Standard step-index fiber geometry (top view, and profile).

We can write Eq. (3.28) explicitly as:

$$\left(\frac{\partial^2}{\partial \rho^2} + \frac{1}{\rho} \frac{\partial}{\partial \rho} + \frac{1}{\rho^2} \frac{\partial^2}{\partial \theta^2} + (n^2 k_0^2 - \beta^2) \right) \begin{Bmatrix} E_z(\rho, \theta) \\ H_z(\rho, \theta) \end{Bmatrix} = 0 \quad (3.29)$$

Because of (Eqs. (3.24)-(3.27)), we only need to solve for longitudinal components $E_z(\rho, \theta)$ and $H_z(\rho, \theta)$ to get the complete solution for the E and H fields,. The general solutions are formed from the linear combination of Hankel function of first and second kind, and it can be written as:

$$E_z(\rho, \theta) = E_z(\rho) \cos(l\theta + \phi_i) = [A_i H_l^{(1)}(k_s \rho) + B_i H_l^{(2)}(k_s \rho)] \cos(l\theta + \phi_i) \quad (3.30)$$

$$H_z(\rho, \theta) = H_z(\rho) \cos(l\theta + \psi_i) = [C_i H_l^{(1)}(k_s \rho) + D_i H_l^{(2)}(k_s \rho)] \cos(l\theta + \psi_i) \quad (3.31)$$

where $H_l^{(1)}$ and $H_l^{(2)}$ are Hankel functions with $H_l^{(1)}$ representing outgoing radial wave and $H_l^{(2)}$ representing an incoming radial wave. A_i , B_i , C_i , D_i , ϕ_i and ψ_i are the constants at the i th layer, l is an integer, the transverse propagation constant:

$$k_s = \sqrt{(\omega^2 \mu \epsilon_s - \beta^2)} = \sqrt{(n_s^2 k_0^2 - \beta^2)} \quad (3.32)$$

where $s = 1, 2$ represents the two media in the core and cladding.

In a medium of refractive index n , the light travels at speed c/n . However, in a waveguide, the material index is not uniform, and light does not travel in a straight line. For a given mode in a given waveguide, the equivalent index of a material where the light would travel in a straight line at the same speed as that mode within the waveguide is called the effective index (n_{eff}). Effective index for each mode is related to the propagation constant by the following relation:

$$\beta = k_0 n_{eff} \quad (3.33)$$

In an optical fiber, each n_{eff} is located between the refractive index of the fiber core material (n_{co}), and the refractive index of the cladding (n_{cl}):

$$n_{cl} < n_{eff} < n_{co} \quad (3.34)$$

3.3 Transfer Matrix Method (TMM) for Layered Fiber

In the proposed research, we will focus on optimizing a special type of MMF, which was introduced by Ramachandran et al [16]. This vortex fibers have a cladding diameter from 80 μm to 160 μm in 5 μm steps. These fibers were all drawn from the same preform with the ID 'dk110127' (where 'dk' is short for Denmark and '110127' indicates the date the preform was made). The preform was made with an industry standard Modified Chemical Vapor Deposition (MCVD) method, which was then used to create fibers with different cladding diameters. Different cladding sizes correspond to different core sizes since the fibers were drawn from the same preform. (Figure 3.2) shows the optical microscope image and the fiber core region surrounded by a ring region.

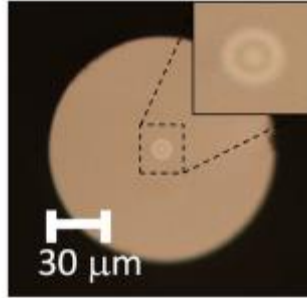


Figure 3.2: An optical microscope image of the end facet of the vortex fiber dk11OD100. [16]

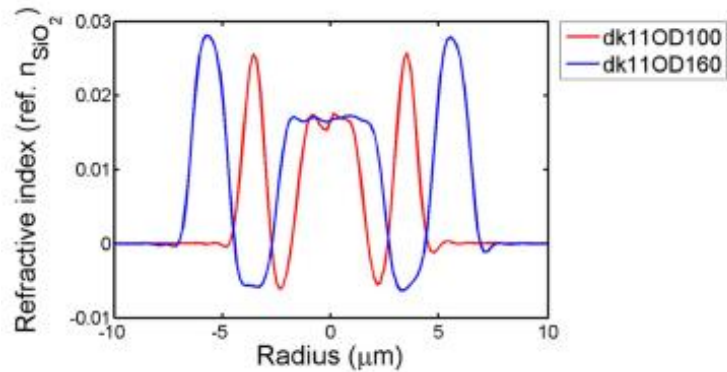


Figure 3.3: Measured refractive index profiles for the fiber dk11OD100 and dk11OD1160. [16]

In this research, we simulate this fiber with the Transfer Matrix Method (TMM) and increase the size of these vortex fibers in order to enable the propagation of more modes inside these fibers. This task is an extension of previous work in [16] where vortex fibers with the diameter cladding sizes varying from $80 \mu\text{m}$ to $160 \mu\text{m}$ were investigated for 9 propagating modes.

Although some commercial software packages are available to solve for modes numerically in optical fibers, in this chapter we develop our own software. The goal was two-fold: first, implementing the algorithms by ourselves is the best way to enhance our understanding; second, we have no limitations on the customizations that can be done to solve for particular

problems when we use our own software. Although our program may not be more accurate than commercial ones, we believe that it is usable, and most customizable.

To solve for effective index of step-index fiber or fiber with multi-layers, we use the algorithm of transfer matrix method [34, 35]. The advantages of the TMM, compared to other numerical methods such as finite element methods (FEM), is its speed and accuracy, ability to locate and identify certain modes easily.

3.4 Numerical Solution with Transfer Matrix Method

The four field components (E_z , H_θ , H_z , E_θ) in each uniform cylindrical layer can be expressed as a linear combination of any two types of Bessel functions [35]. In matrix form, they can be written as:

$$\begin{bmatrix} E_z(\rho) \\ H_z(\rho) \\ H_\theta(\rho) \\ E_\theta(\rho) \end{bmatrix}_{ith \text{ layer}} = M(i, \rho) \begin{bmatrix} A_i \\ C_i \\ B_i \\ D_i \end{bmatrix} \quad (3.35)$$

where $E_z(\rho)$ and $E_\theta(\rho)$ are electrical field components and $H_z(\rho)$ and $H_\theta(\rho)$ are magnetic field components of the guided mode in a fiber which is discretized into radial regions with constant refractive indices, i.e. multi-layered fiber. Here, i denotes the layer number. A_i , B_i , C_i and D_i are the coefficients at the ith layer. $M(i, \rho)$ is a 4×4 matrix at the ith layer that involves Hankel functions. Usually, the modal characteristics of multilayered fiber are calculated by the transfer-matrix method [36]. We can approximate the measured profile with multilayered fiber having 6 layers as we see in (Figure 3.4), so we call it the approximated profile or multi-layered profile.

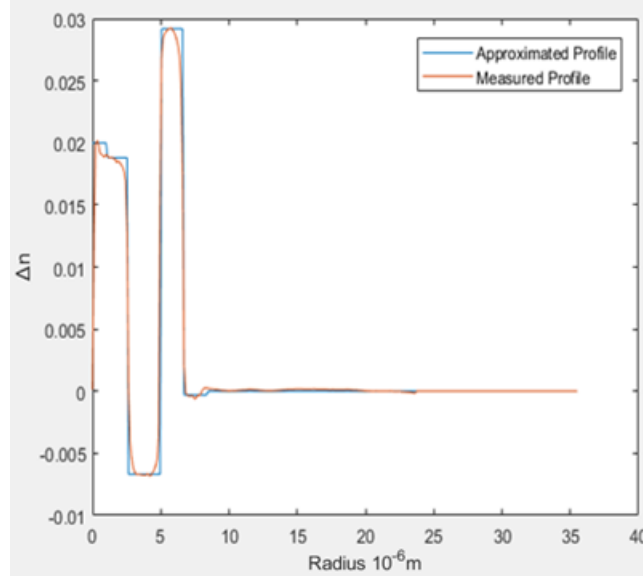


Figure 3.4: Measured and approximated profile for the fiber dk11OD160.

Now we consider the boundary conditions at the general cladding interface between the i th and $(i+1)$ th layers at $\rho = \rho_i$, where the i th cladding layer has a medium with index (say $s=1$) and the $(i+1)$ th cladding layer has a medium with index (say $s=2$), we can apply (Eqs. (3.28) - (3.30)) to the both sides of the interface:

$$E_z(\rho, \theta) = [A_i H_l^{(1)}(k_1 \rho) + B_i H_l^{(2)}(k_1 \rho)] \cos(l\theta + \phi_i), \quad \rho < \rho_i \quad (3.36)$$

$$E_z(\rho, \theta) = [A_{i+1} H_l^{(1)}(k_1 \rho) + B_{i+1} H_l^{(2)}(k_1 \rho)] \cos(l\theta + \phi_{i+1}), \quad \rho > \rho_i \quad (3.37)$$

And

$$H_z(\rho, \theta) = [C_i H_l^{(1)}(k_1 \rho) + D_i H_l^{(2)}(k_1 \rho)] \cos(l\theta + \psi_i), \quad \rho < \rho_i \quad (3.38)$$

$$H_z(\rho, \theta) = [C_{i+1} H_l^{(1)}(k_2 \rho) + D_{i+1} H_l^{(2)}(k_2 \rho)] \cos(l\theta + \psi_{i+1}), \quad \rho > \rho_i \quad (3.39)$$

The boundary conditions representing continuity of $E_z(\rho, \theta)$, $H_z(\rho, \theta)$, $E_\theta(\rho, \theta)$ and $H_\theta(\rho, \theta)$ at the interface $\rho = \rho_i$ can be expressed as a 4×4 matrix $T_{21}(\rho_i)$ which relates the coefficients in two adjacent layers:

$$\begin{pmatrix} A_{i+1} \\ C_{i+1} \\ B_{i+1} \\ D_{i+1} \end{pmatrix} = T_{21}(\rho_i) \begin{pmatrix} A_i \\ C_i \\ B_i \\ D_i \end{pmatrix} \quad (3.40)$$

In terms of field solutions in (Eqs. (3.36) - (3.37)), the continuity of E_z gives:

$$[A_i H_l^{(1)}(k_1 \rho_i) + B_i H_l^{(2)}(k_1 \rho_i)] \cos(l\theta + \phi_i) = [A_{i+1} H_l^{(1)}(k_2 \rho_i) + B_{i+1} H_l^{(2)}(k_2 \rho_i)] \cos(l\theta + \phi_{i+1}) \quad (3.41)$$

This equation is satisfied for all θ , which means:

$$\phi_i = \phi_{i+1} \quad (3.42)$$

Similarly, the continuity of H_z gives us

$$\psi_i = \psi_{i+1} \quad (3.43)$$

Now we normalize the (Eqs. (3.36) - (3.39)) with $k_a = 2\pi/a$

$$\tilde{\beta} = \beta/k_a \quad (3.44)$$

$$\tilde{k}_o = a/\lambda = \tilde{\omega} \quad (3.45)$$

$$\tilde{\rho}_i = \rho_i/a \quad (3.46)$$

$$\tilde{k}_m = k_m/k_a \quad (3.47)$$

$$\tilde{x}_{mi} = 2\pi\tilde{k}_m\tilde{\rho}_i \quad (3.48)$$

$$\eta_o = \sqrt{\frac{\mu_o}{\epsilon_o}} \quad (3.49)$$

$$n_s = \sqrt{\mu_{rs}\epsilon_{rs}} \quad (3.50)$$

where $s=0$ and $s=1, 2, 3, 4, 5$ represent the core index and cladding indices for layers 1, 2, ..., 5 respectively.

Thus, we can write the continuity of (ρ, θ) and (ρ, θ) in terms of (Eqs. (3.36) - (3.39)) as follows:

$$[A_i H_l^{(1)}(\tilde{x}_{1i}) + B_i H_l^{(2)}(\tilde{x}_{1i})] = [A_{i+1} H_l^{(1)}(\tilde{x}_{2i}) + B_{i+1} H_l^{(2)}(\tilde{x}_{2i})] \quad (3.51)$$

$$[C_i H_l^{(1)}(\tilde{x}_{1i}) + D_i H_l^{(2)}(\tilde{x}_{1i})] = [C_{i+1} H_l^{(1)}(\tilde{x}_{2i}) + D_{i+1} H_l^{(2)}(\tilde{x}_{2i})] \quad (3.52)$$

The continuity of (ρ, θ) in Eqs. (3.25) in terms of (Eqs. (3.38) - (3.39)) gives:

$$\begin{aligned} & \frac{1}{\tilde{k}_1^2} \left(\begin{aligned} & \frac{-l}{a\tilde{\rho}_i} [A_i H_l^{(1)}(\tilde{x}_{1i}) + B_i H_l^{(2)}(\tilde{x}_{1i})] \sin(l\theta + \phi_i) \\ & - \frac{2\pi\tilde{\omega}\eta_o\mu_{r1}}{a\tilde{\beta}} \tilde{k}_1 [C_i H_l^{(1)'}(\tilde{x}_{1i}) + D_i H_l^{(2)'}(\tilde{x}_{1i})] \cos(l\theta + \psi_i) \end{aligned} \right) \\ & = \frac{1}{\tilde{k}_2^2} \left(\begin{aligned} & \frac{-l}{a\tilde{\rho}_i} [A_{i+1} H_l^{(1)}(\tilde{x}_{2i}) + B_{i+1} H_l^{(2)}(\tilde{x}_{2i})] \sin(l\theta + \phi_{i+1}) \\ & - \frac{2\pi\tilde{\omega}\eta_o\mu_{r2}}{a\tilde{\beta}} \tilde{k}_2 [C_{i+1} H_l^{(1)'}(\tilde{x}_{2i}) + D_{i+1} H_l^{(2)'}(\tilde{x}_{2i})] \cos(l\theta + \psi_{i+1}) \end{aligned} \right) \end{aligned} \quad (3.53)$$

where the primed quantities are the derivatives with respect to their own argument. This has to be satisfied for all θ . From (Eqs. (3.51) - (3.52)), we get:

$$\begin{aligned} & \left(\frac{1}{\tilde{k}_1^2} \right) \{A_i H_l^{(1)}(\tilde{x}_{1i}) + B_i H_l^{(2)}(\tilde{x}_{1i})\} \\ & \neq \left(\frac{1}{\tilde{k}_2^2} \right) \{A_{i+1} H_l^{(1)}(\tilde{x}_{2i}) + B_{i+1} H_l^{(2)}(\tilde{x}_{2i})\} \end{aligned} \quad (3.54)$$

$$\begin{aligned} & \left(\frac{\mu_{r1}}{\tilde{k}_1} \right) \{C_i H_l^{(1)'}(\tilde{x}_{1i}) + D_i H_l^{(2)'}(\tilde{x}_{1i})\} \\ & \neq \left(\frac{\mu_{r2}}{\tilde{k}_2} \right) \{C_{i+1} H_l^{(1)'}(\tilde{x}_{2i}) + D_{i+1} H_l^{(2)'}(\tilde{x}_{2i})\} \end{aligned} \quad (3.55)$$

provided $\tilde{k}_1 \neq \tilde{k}_2$. Thus, we can say from (Eqs. (3.54) - (3.55)) that:

$$\sin(l\theta + \phi_i) = \pm \cos(l\theta + \psi_i) \quad (3.56)$$

or equivalently,

$$\phi_i = \psi_i \pm \pi/2 \quad (3.57)$$

The continuity of $H_\theta(\rho, \theta)$ in Eq. (3.27) in terms of (Eqs. (3.38) - (3.39)) gives:

$$\begin{aligned} & \frac{1}{\tilde{k}_1^2} \left(\begin{array}{l} \frac{-l}{a\tilde{\rho}_i} [C_i H_l^{(1)}(\tilde{x}_{1i}) + D_i H_l^{(2)}(\tilde{x}_{1i})] \sin(l\theta + \psi_i) \\ -\frac{2\pi\tilde{\omega}\varepsilon_{r1}}{\eta_o a\tilde{\beta}} \tilde{k}_1 [A_i H_l^{(1)' }(\tilde{x}_{1i}) + B_i H_l^{(2)' }(\tilde{x}_{1i})] \cos(l\theta + \phi_i) \end{array} \right) \\ &= \frac{1}{\tilde{k}_2^2} \left(\begin{array}{l} \frac{-l}{a\tilde{\rho}_i} [C_{i+1} H_l^{(1)}(\tilde{x}_{2i}) + D_{i+1} H_l^{(2)}(\tilde{x}_{2i})] \sin(l\theta + \psi_{i+1}) \\ -\frac{2\pi\tilde{\omega}\varepsilon_{r2}}{\eta_o a\tilde{\beta}} \tilde{k}_2 [A_{i+1} H_l^{(1)' }(\tilde{x}_{2i}) + B_{i+1} H_l^{(2)' }(\tilde{x}_{2i})] \cos(l\theta + \phi_{i+1}) \end{array} \right) \end{aligned} \quad (3.58)$$

From (Eqs. (3.54) - (3.55)) or equivalently Eq. (3.57) we can classify the waves into two categories:

$$\text{I} \quad \begin{aligned} E_z(\rho_i, \theta) &= [A_i H_l^{(1)}(\tilde{x}_{si}) + B_i H_l^{(2)}(\tilde{x}_{si})] \cos(l\theta) \\ H_z(\rho_i, \theta) &= [C_i H_l^{(1)}(\tilde{x}_{si}) + D_i H_l^{(2)}(\tilde{x}_{si})] \sin(l\theta) \end{aligned} \quad (3.59)$$

$$\text{II} \quad \begin{aligned} E_z(\rho_i, \theta) &= [A_i H_l^{(1)}(\tilde{x}_{si}) + B_i H_l^{(2)}(\tilde{x}_{si})] \sin(l\theta) \\ H_z(\rho_i, \theta) &= [C_i H_l^{(1)}(\tilde{x}_{si}) + D_i H_l^{(2)}(\tilde{x}_{si})] \cos(l\theta) \end{aligned} \quad (3.60)$$

The boundary conditions for these two categories are summarized below:

For Category I,

$$A_i H_l^{(1)}(\tilde{x}_{1i}) + B_i H_l^{(2)}(\tilde{x}_{1i}) + 0 + 0 = A_{i+1} H_l^{(1)}(\tilde{x}_{2i}) + B_{i+1} H_l^{(2)}(\tilde{x}_{2i}) + 0 + 0 \quad (3.61)$$

$$\begin{aligned} & \frac{\tilde{\omega}\varepsilon_{r1}}{\eta_o \tilde{k}_1 \tilde{\beta} k_a} A_i H_l^{(1)' }(\tilde{x}_{1i}) + \frac{\tilde{\omega}\varepsilon_{r1}}{\eta_o \tilde{k}_1 \tilde{\beta} k_a} B_i H_l^{(2)' }(\tilde{x}_{1i}) \\ &+ \frac{l}{\tilde{k}_1 \tilde{x}_{1i} k_a} C_i H_l^{(1)}(\tilde{x}_{1i}) + \frac{l}{\tilde{k}_1 \tilde{x}_{1i} k_a} D_i H_l^{(2)}(\tilde{x}_{1i}) \vec{E} \\ &= \frac{\tilde{\omega}\varepsilon_{r2}}{\eta_o \tilde{k}_2 \tilde{\beta} k_a} A_{i+1} H_l^{(1)' }(\tilde{x}_{2i}) + \frac{\tilde{\omega}\varepsilon_{r2}}{\eta_o \tilde{k}_2 \tilde{\beta} k_a} B_{i+1} H_l^{(2)' }(\tilde{x}_{2i}) \\ &+ \frac{l}{\tilde{k}_2 \tilde{x}_{2i} k_a} C_{i+1} H_l^{(1)}(\tilde{x}_{2i}) + \frac{l}{\tilde{k}_2 \tilde{x}_{2i} k_a} D_{i+1} H_l^{(2)}(\tilde{x}_{2i}), \end{aligned} \quad (3.62)$$

$$0+0+C_i H_l^{(1)}(\tilde{x}_{1i})+D_i H_l^{(2)}(\tilde{x}_{1i})=0+0+C_{i+1} H_l^{(1)}(\tilde{x}_{2i})+D_{i+1} H_l^{(2)}(\tilde{x}_{2i}) \quad (3.63)$$

$$\begin{aligned} & \frac{l}{\tilde{k}_1 \tilde{x}_{1i} k_a} A_i H_l^{(1)}(\tilde{x}_{1i}) + \frac{l}{\tilde{k}_1 \tilde{x}_{1i} k_a} B_i H_l^{(2)}(\tilde{x}_{1i}) \\ & + \frac{\eta_o \tilde{\omega} \mu_{r1}}{\tilde{k}_1 \tilde{\beta} k_a} C_i H_l^{(1)'}(\tilde{x}_{1i}) + \frac{\eta_o \tilde{\omega} \mu_{r1}}{\tilde{k}_1 \tilde{\beta} k_a} D_i H_l^{(2)'}(\tilde{x}_{1i}) \\ & = \frac{l}{\tilde{k}_2 \tilde{x}_{2i} k_a} A_{i+1} H_l^{(1)}(\tilde{x}_{2i}) + \frac{l}{\tilde{k}_2 \tilde{x}_{2i} k_a} B_{i+1} H_l^{(2)}(\tilde{x}_{2i}) \\ & + \frac{\eta_o \tilde{\omega} \mu_{r2}}{\tilde{k}_2 \tilde{\beta} k_a} C_{i+1} H_l^{(1)'}(\tilde{x}_{2i}) + \frac{\eta_o \tilde{\omega} \mu_{r2}}{\tilde{k}_2 \tilde{\beta} k_a} D_{i+1} H_l^{(2)'}(\tilde{x}_{2i}), \end{aligned} \quad (3.64)$$

For Category II, there are similar equations except that the coefficient $\frac{l}{\tilde{k}_s \tilde{x}_{si} k_a}$ is replaced by $-\frac{l}{\tilde{k}_s \tilde{x}_{si} k_a}$. (Eqs. (3.61) - (3.64)) can be written as a matrix equation:

$$\underline{M}'_2(\tilde{\rho}_i) \begin{pmatrix} A_{i+1} \\ C_{i+1} \\ B_{i+1} \\ D_{i+1} \end{pmatrix} = \underline{M}'_1(\tilde{\rho}_i) \begin{pmatrix} A_i \\ C_i \\ B_i \\ D_i \end{pmatrix} \quad (3.65)$$

where the interface matrix is defined

$$\underline{M}'_s(\tilde{\rho}_i) = \underline{M}_s(\tilde{\rho}_i) \underline{\phi}_s(\tilde{\rho}_i) \quad (3.66)$$

with

$$\underline{M}_s(\tilde{\rho}_i) = \begin{pmatrix} h_l^{(1)}(\tilde{x}_{si}) & 0 & h_l^{(2)}(\tilde{x}_{si}) & 0 \\ 0 & h_l^{(1)}(\tilde{x}_{si}) & 0 & h_l^{(2)}(\tilde{x}_{si}) \\ \frac{\tilde{k}_o \varepsilon_{rs}}{\tilde{\beta} \tilde{k}_s \eta_o} h_l^{(1)'}(\tilde{x}_{si}) & \frac{l}{\tilde{k}_s \tilde{x}_{si}} h_l^{(1)}(\tilde{x}_{si}) & \frac{\tilde{k}_o \varepsilon_{rs}}{\tilde{\beta} \tilde{k}_s \eta_o} h_l^{(2)'}(\tilde{x}_{si}) & \frac{l}{\tilde{k}_s \tilde{x}_{si}} h_l^{(2)}(\tilde{x}_{si}) \\ \frac{l}{\tilde{k}_s \tilde{x}_{si}} h_l^{(1)}(\tilde{x}_{si}) & \frac{\tilde{k}_o \eta_o \mu_{rs}}{\tilde{\beta} \tilde{k}_s} h_l^{(1)'}(\tilde{x}_{si}) & \frac{l}{\tilde{k}_s \tilde{x}_{si}} h_l^{(2)}(\tilde{x}_{si}) & \frac{\tilde{k}_o \eta_o \mu_{rs}}{\tilde{\beta} \tilde{k}_s} h_l^{(2)'}(\tilde{x}_{si}) \end{pmatrix} \quad (3.67)$$

for s = 0, 1, 2, 3, 4, 5, and:

$$\underline{\phi}_s(\tilde{\rho}_i) = \begin{pmatrix} \exp(j\tilde{x}_{s_i})\underline{I} & \underline{0} \\ \underline{0} & \exp(-j\tilde{x}_{s_i})\underline{I} \end{pmatrix} \quad (3.68)$$

is the plane wave propagation matrix, \underline{I} is a 2×2 identity matrix and $\underline{0}$ is a 2×2 zero matrix. In Eq.

(3.66), Hankel functions are normalized by introducing $h_i^{(1)}(\tilde{x}_s) = H_i^{(1)}(\tilde{x}_s)/\exp(j\tilde{x}_s)$ and

$h_i^{(2)}(\tilde{x}_s) = H_i^{(2)}(\tilde{x}_s)/\exp(-j\tilde{x}_s)$. Moreover, field coefficients are re-grouped so that outgoing wave

coefficients form the outgoing vector:

$$\bar{u}_i = (A_i \ C_i)^T \quad (3.69)$$

and incoming wave coefficients forms another vector

$$\bar{d}_i = (B_i \ D_i)^T \quad (3.70)$$

i.e. $(A_i \ C_i \ B_i \ D_i)^T = (\bar{u}_i \ \bar{d}_i)$. In this way, the fast oscillating and decaying functions for outgoing and

incoming waves are factored out into $\underline{\phi}_s(\tilde{\rho}_i)$ and the transfer matrix can be expressed in terms of

2×2 matrices. The new formulation improves numerical stability significantly.

The transfer matrix $\underline{T}_{21}(\rho_i)$ in Eq. (3.40) can be generalized into matrix $\underline{T}_{s_1s_2}(\tilde{\rho}_i)$ with $s_2=1$ for

the input medium and $s_1=2$ for the output medium with Eq. (3.65) as

$$\underline{T}_{s_1s_2}(\tilde{\rho}_i) = \underline{\phi}_{s_1}^*(\tilde{\rho}_i) \underline{t}_{s_1s_2}(\tilde{\rho}_i) \underline{\phi}_{s_2}(\tilde{\rho}_i) \quad (3.71)$$

where $\underline{t}_{s_1s_2}(\tilde{\rho}_i) = \underline{M}_{s_1}^{-1}(\tilde{\rho}_i) \underline{M}_{s_2}(\tilde{\rho}_i)$ is the interface transfer matrix:

$$\underline{t}_{s_1s_2}(\tilde{\rho}_i) = \begin{pmatrix} [\underline{t}_{s_1s_2}(\tilde{\rho}_i)]_{11} & [\underline{t}_{s_1s_2}(\tilde{\rho}_i)]_{12} \\ [\underline{t}_{s_1s_2}(\tilde{\rho}_i)]_{21} & [\underline{t}_{s_1s_2}(\tilde{\rho}_i)]_{22} \end{pmatrix} \quad (3.72)$$

The elements of Eq. (3.72) are 2×2 matrices:

$$\begin{aligned}
\underline{[t_{s1s2}(\tilde{\rho}_i)]_{11}} &= j \frac{\pi \tilde{\alpha}_{s1i}}{4 \tilde{k}_{s2}} \\
&\times \left(\begin{array}{cc} \tilde{k}_{s2} h_l^{(2)'}(\tilde{x}_{s1i}) h_l^{(1)}(\tilde{x}_{s2i}) - \tilde{k}_{s1} h_l^{(1)'}(\tilde{x}_{s2i}) h_l^{(2)}(\tilde{x}_{s1i}) \frac{\varepsilon_{rs2}}{\varepsilon_{rs1}} & \frac{\tilde{\beta} \tilde{\eta}_o}{\tilde{\omega} \varepsilon_{s2}} l h_l^{(1)}(\tilde{x}_{s2i}) h_l^{(2)}(\tilde{x}_{s1i}) \left(\frac{\tilde{k}_{s2}}{\tilde{x}_{s1i}} - \frac{\tilde{k}_{s1}}{\tilde{x}_{s2i}} \right) \\ \frac{\tilde{\beta}}{\tilde{\omega} \tilde{\eta}_o \mu_{rs1}} l h_l^{(1)}(\tilde{x}_{s2i}) h_l^{(2)}(\tilde{x}_{s1i}) \left(\frac{\tilde{k}_{s2}}{\tilde{x}_{s1i}} - \frac{\tilde{k}_{s1}}{\tilde{x}_{s2i}} \right) & \tilde{k}_{s2} h_l^{(2)'}(\tilde{x}_{s1i}) h_l^{(1)}(\tilde{x}_{s2i}) - \tilde{k}_{s1} h_l^{(1)'}(\tilde{x}_{rs2}) h_l^{(2)}(\tilde{x}_{s1i}) \frac{\mu_{rs2}}{\mu_{rs1}} \end{array} \right) \quad (3.73)
\end{aligned}$$

$$\begin{aligned}
\underline{[t_{s1s2}(\tilde{\rho}_i)]_{12}} &= j \frac{\pi \tilde{\alpha}_{s1i}}{4 \tilde{k}_{s2}} \\
&\times \left(\begin{array}{cc} \tilde{k}_{s2} h_l^{(2)'}(\tilde{x}_{s2i}) h_l^{(2)}(\tilde{x}_{s2i}) - \tilde{k}_{s1} h_l^{(2)'}(\tilde{x}_{s2i}) h_l^{(2)}(\tilde{x}_{s1i}) \frac{\varepsilon_{rs2}}{\varepsilon_{rs1}} & \frac{\tilde{\beta} \tilde{\eta}_o}{\tilde{\omega} \varepsilon_{rs1}} l h_l^{(2)}(\tilde{x}_{s2i}) h_l^{(2)}(\tilde{x}_{rs1}) \left(\frac{\tilde{k}_{s2}}{\tilde{x}_{s1i}} - \frac{\tilde{k}_{s1}}{\tilde{x}_{s2i}} \right) \\ \frac{\tilde{\beta}}{\tilde{\omega} \tilde{\eta}_o \mu_{rs1}} l h_l^{(2)}(\tilde{x}_{s2i}) h_l^{(2)}(\tilde{x}_{s1i}) \left(\frac{\tilde{k}_{s2}}{\tilde{x}_{s1i}} - \frac{\tilde{k}_{s1}}{\tilde{x}_{s2i}} \right) & \tilde{k}_{s2} h_l^{(2)'}(\tilde{x}_{s1i}) h_l^{(2)}(\tilde{x}_{s2i}) - \tilde{k}_{s1} h_l^{(2)'}(\tilde{x}_{s2i}) h_l^{(2)}(\tilde{x}_{s1i}) \frac{\mu_{rs2}}{\mu_{rs1}} \end{array} \right) \quad (3.74)
\end{aligned}$$

$$\begin{aligned}
\underline{[t_{s1s2}(\tilde{\rho}_i)]_{21}} &= -j \frac{\pi \tilde{\alpha}_{s1i}}{4 \tilde{k}_{s2}} \\
&\times \left(\begin{array}{cc} \tilde{k}_{s2} h_l^{(1)'}(\tilde{x}_{s1i}) h_l^{(1)}(\tilde{x}_{s2i}) - \tilde{k}_{s1} h_l^{(1)'}(\tilde{x}_{s2i}) h_l^{(1)}(\tilde{x}_{s1i}) \frac{\varepsilon_{rs2}}{\varepsilon_{rs1}} & \frac{\tilde{\beta} \tilde{\eta}_o}{\tilde{\omega} \varepsilon_{rs1}} l h_l^{(1)}(\tilde{x}_{mi}) h_l^{(1)}(\tilde{x}_{mi}) \left(\frac{\tilde{k}_{s2}}{\tilde{x}_{s1i}} - \frac{\tilde{k}_{s1}}{\tilde{x}_{s2i}} \right) \\ \frac{\tilde{\beta}}{\tilde{\omega} \tilde{\eta}_o \mu_{rs1}} l h_l^{(1)}(\tilde{x}_{s2i}) h_l^{(1)}(\tilde{x}_{s1i}) \left(\frac{\tilde{k}_{s2}}{\tilde{x}_{s1i}} - \frac{\tilde{k}_{s1}}{\tilde{x}_{s2i}} \right) & \tilde{k}_{s2} h_l^{(1)'}(\tilde{x}_{s1i}) h_l^{(1)}(\tilde{x}_{s2i}) - \tilde{k}_{s1} h_l^{(1)'}(\tilde{x}_{s2i}) h_l^{(1)}(\tilde{x}_{s1i}) \frac{\mu_{rs2}}{\mu_{rs1}} \end{array} \right) \quad (3.75)
\end{aligned}$$

$$\begin{aligned}
\underline{[t_{s1s2}(\tilde{\rho}_i)]_{22}} &= -j \frac{\pi \tilde{\alpha}_{s1i}}{4 \tilde{k}_{s2}} \\
&\times \left(\begin{array}{cc} \tilde{k}_{s2} h_l^{(1)'}(\tilde{x}_{s1i}) h_l^{(2)}(\tilde{x}_{s2i}) - \tilde{k}_{s1} h_l^{(2)'}(\tilde{x}_{s2i}) h_l^{(1)}(\tilde{x}_{s1i}) \frac{\varepsilon_{rs2}}{\varepsilon_{rs1}} & \frac{\tilde{\beta} \tilde{\eta}_o}{\tilde{\omega} \varepsilon_{rs1}} l h_l^{(2)}(\tilde{x}_{s2i}) h_l^{(1)}(\tilde{x}_{s1i}) \left(\frac{\tilde{k}_{s2}}{\tilde{x}_{s1i}} - \frac{\tilde{k}_{s1}}{\tilde{x}_{s2i}} \right) \\ \frac{\tilde{\beta}}{\tilde{\omega} \tilde{\eta}_o \mu_{rs1}} l h_l^{(2)}(\tilde{x}_{s2i}) h_l^{(1)}(\tilde{x}_{s1i}) \left(\frac{\tilde{k}_{s2}}{\tilde{x}_{s1i}} - \frac{\tilde{k}_{s1}}{\tilde{x}_{s2i}} \right) & \tilde{k}_{s2} h_l^{(1)'}(\tilde{x}_{s1i}) h_l^{(2)}(\tilde{x}_{s2i}) - \tilde{k}_{s1} h_l^{(2)'}(\tilde{x}_{s2i}) h_l^{(1)}(\tilde{x}_{s1i}) \frac{\mu_{rs2}}{\mu_{rs1}} \end{array} \right) \quad (3.76)
\end{aligned}$$

For an multi-layered fiber with 6 layers, the transfer matrix \underline{T}_{total} relates coefficients at the first boundary ($i=0$) to those at the last boundary ($i=5$):

$$\begin{bmatrix} A_5 \\ C_5 \\ B_5 \\ D_5 \end{bmatrix} = \underline{T}_{total} \begin{bmatrix} A_0 \\ C_0 \\ B_0 \\ D_0 \end{bmatrix} \quad (3.77)$$

where:

$$T_{total} = \phi_5(\tilde{\rho}_5 - \tilde{\rho}_4)T_{54}(\tilde{\rho}_4)\phi_4(\tilde{\rho}_4 -$$
(3.78)

$$\tilde{\rho}_3)T_{43}(\tilde{\rho}_3)\phi_3(\tilde{\rho}_3 - \tilde{\rho}_2)T_{32}(\tilde{\rho}_2)\phi_2(\tilde{\rho}_2 - \tilde{\rho}_1)T_{21}(\tilde{\rho}_1)\phi_1(\tilde{\rho}_1 - \tilde{\rho}_0)T_{10}(\tilde{\rho}_0)\phi_0(\tilde{\rho}_0)$$

and $\rho_0 = a$ (i.e. $\tilde{\rho}_0 = 1$).

Chapter 4

Simulations of modal properties of optical fiber

The increases of the data capacity by four orders of magnitude in the past three decades has accelerated the pace of reaching limits by nonlinear effects [64] for current fiber optical systems. The use of multicore [65] and multimode [66] fibers in spatial division multiplexing (SDM) has emerged to address the capacity crunch.

We studied a class of specialty few mode fibers (FMFs) called vortex fiber, introduced by Ramachandran et al. [16]. This fiber had been successfully demonstrated to achieve 400Gb/sec data transmission over 1.1 kilometers with the fundamental mode LP_{01} and second mode LP_{11} [5]. It has attracted a lot of attention for its applications in SDM [32], optical sensing [36], optical tweezers, atom manipulation, and optical communications [44]. Its refractive index profile is very close to the annular intensity profile of orbital angular momentum (OAM) beams (doughnut shape) and supports these OAM modes [16,38,39], which corresponds to higher order modes (HOMs) of the fiber.

As mentioned in chapter 3, we numerically solved the vector wave equation to find the guided modes with transfer matrix method (TMM). In this chapter, we will discuss the results and the error of this method and compare it to finite difference method (FDM). We found an analytical expression for predicting the number of propagating modes, and then optimized the profile by calculating various modal properties such as the number of guided modes, effective group index, material and waveguide dispersions, and effective core area.

We discussed how we could optimize the vortex index profile by considering three different profile indices, all of which can guide HOMs. Their total dispersion parameters for all guided

modes were calculated. Particularly, we have identified the fiber profile that enables the propagation of LP₂₁ with minimum total dispersion. At the end of this chapter, we presented an equation that predicts the waveguide dispersion for all three fiber profiles in a good agreement with numerical solutions.

4.1 Differences between Finite Difference Method (FDM) and Transfer Matrix Method

(TMM)

As mentioned in chapter 3, we solved the full vector waveguide equation that describes the field distribution under the boundary condition set up by the fiber. Formulating the discretized equations as an eigenvalue problem, we can determine the mode or field in terms of eigenvectors for particular eigenvalues that associate with the propagation constant for corresponding guided modes of the fiber.

Since TMM is closely related to the reflection and transmission of propagating modes, it reduces the chances of failing to identify modes comparing it to other generic numerical method such as finite element method (FEM) [34,35]. This method can be easily applied for profiles with layers of constant refractive indices [5]. Previously, the eigenvalues of Vortex Fiber “*dk11OD160*” [16] (which has a cladding diameter of 160 μm) were determined with FDM [19] and found that “*dk11OD160*” fiber can support five propagating modes.

The principle of TMM is to ensure the continuity of the field at each layer interface. Numerically, we solved the vector waveguide equation for the vortex fiber by approximating the profile with step layers to find the best approximated step index profile that produced eigenvalues matching the propagation constants calculated with FDM. Each eigenvalue of the waveguide equation from TMM corresponds to the propagation constants β_{lm} where l is the azimuthal mode index and m is the radial mode index. We can represent β_{lm} as a function of the effective refractive

index n_{eff}^{lm} for the mode as $\beta_{lm} = k_0 n_{eff}^{lm}$. The solutions that satisfy the field continuity across layers are called fiber modes (defined by l , m and the mode family).

In (Figure 4.1) below, we can see the Vortex index profile fiber [5] compared with the approximated 5-Layers step index profile, and (Figure 4.2) shows us the error in the approximated profile. We found its error with respect to the vortex fiber profile using Eq. (4.1).

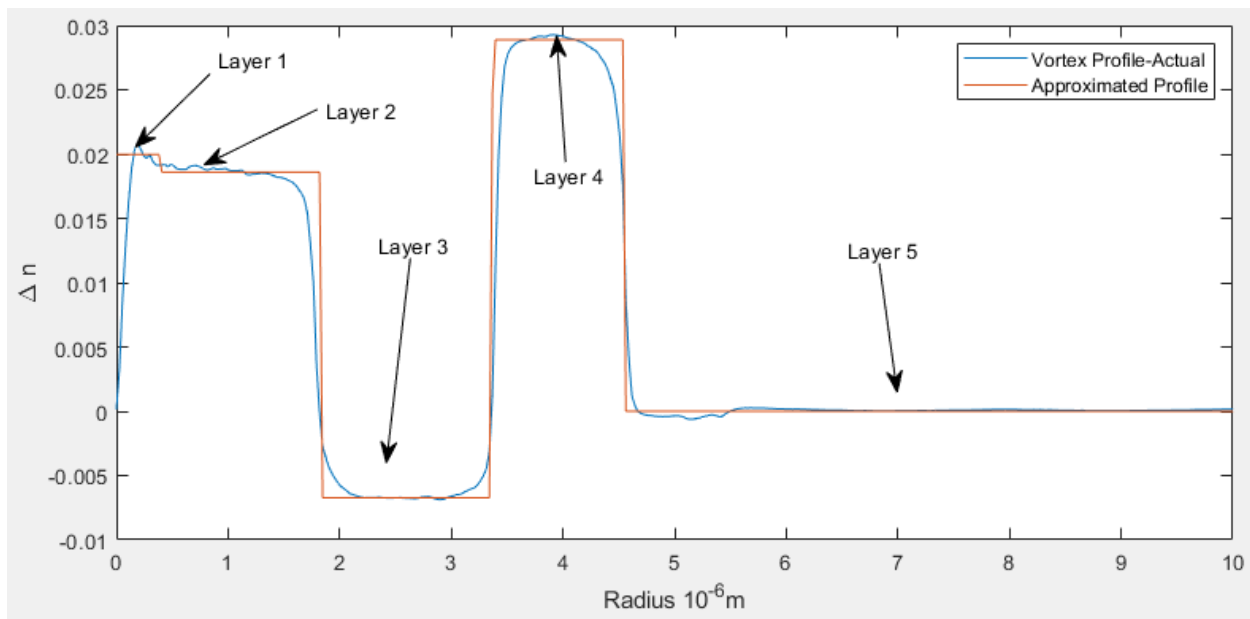


Figure 4.1: Vortex fiber refractive index profile from experiment and its approximation where the difference in index Δn is calculated with respect to the refractive index of silica

$$n_{SiO_2} = 1.444.$$

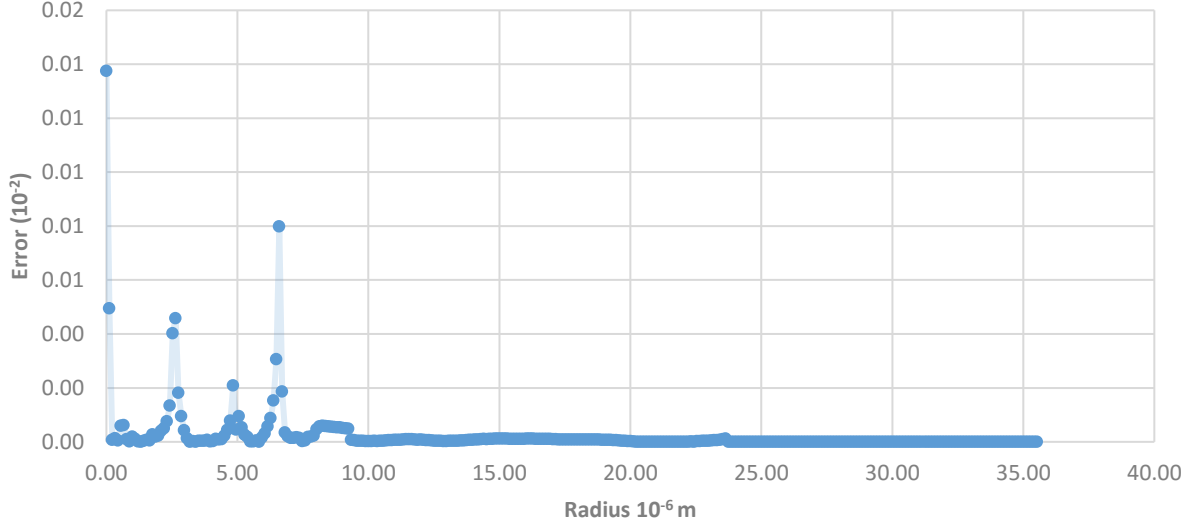


Figure 4.2: Error between the structure of the vortex profile and its approximation.

$$Error = \frac{n(vortex\ fiber) - n(approximated\ fiber)}{n(vortex\ fiber)} \quad (4.1)$$

We calculated n_{eff} for the approximated index profile with TMM and compared its results to those from FDM. (Figure 4.3) shows n_{eff} for LP₀₁, LP₁₁ and LP₂₁ modes of the approximated profile. In this case, we used weakly guided approximation since the mode profiles obtained from the full vector waveguide equation and the scalar wave equation are almost identical [4]. Table 4.1 below shows the ratio between the longitudinal and transverse component of the fields is on order of 10^{-14} from the full vector waveguide equation.

Field	$\max(\text{longitudinal}(z)) / \max(\text{abs}(\text{transverse field}))$
HE ₁₁	3.97×10^{-14}
TM ₀₁	6.69×10^{-14}
HE ₂₁	8.73×10^{-14}
TE ₀₁	4.03×10^{-14}
HE ₃₁	2.32×10^{-14}
EH ₁₁	6.72×10^{-14}

Table 4.1: Ratio between longitudinal and transverse components of the fields.

(Figures 4.3 and 4.4) show n_{eff} values of the approximated profile with 5 layers and the field distribution of LP₀₁, LP₁₁ and LP₂₁ modes respectively; the computation with Eq. (4.2) for the difference between TMM with the vector wave equation and FDM with the scalar wave equation is shown in (Figure 4.5) for LP₀₁, LP₁₁ and LP₂₁ modes.

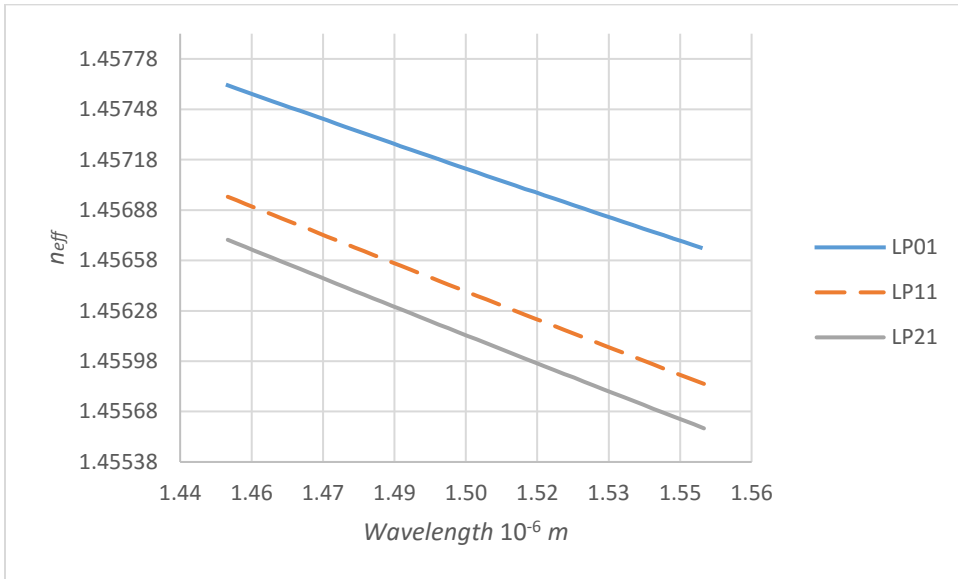


Figure 4.3: Effective index of the approximated profile with 5 layers.

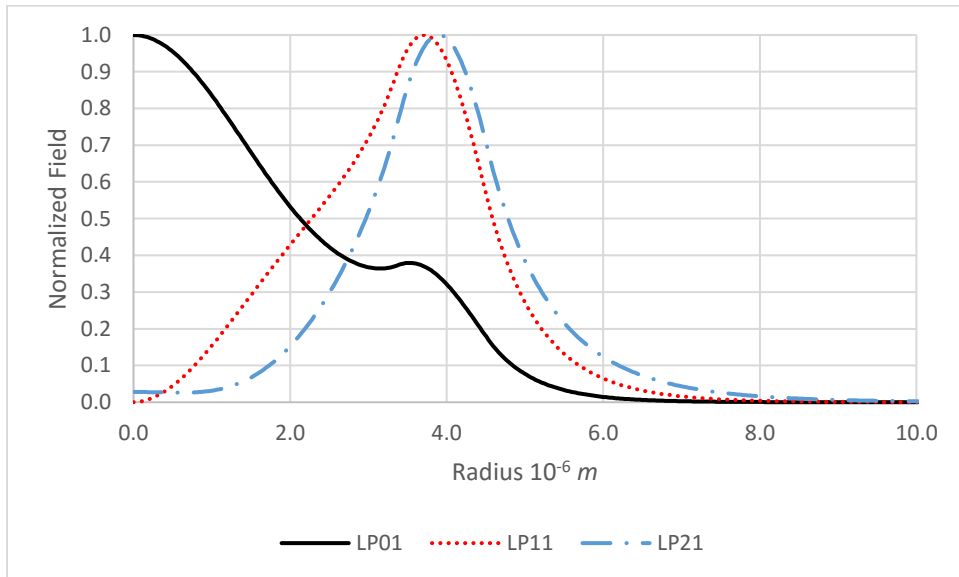


Figure 4.4: Field distribution for LP₀₁, LP₁₁ and LP₂₁ modes.

$$\text{Difference} = \frac{\text{Intensity}(\text{vector wave equation-TMM}) - \text{Intensity}(\text{Scalar wave equation-FDM})}{\text{Intensity}(\text{vector wave equation-TMM})} \quad (4.2)$$

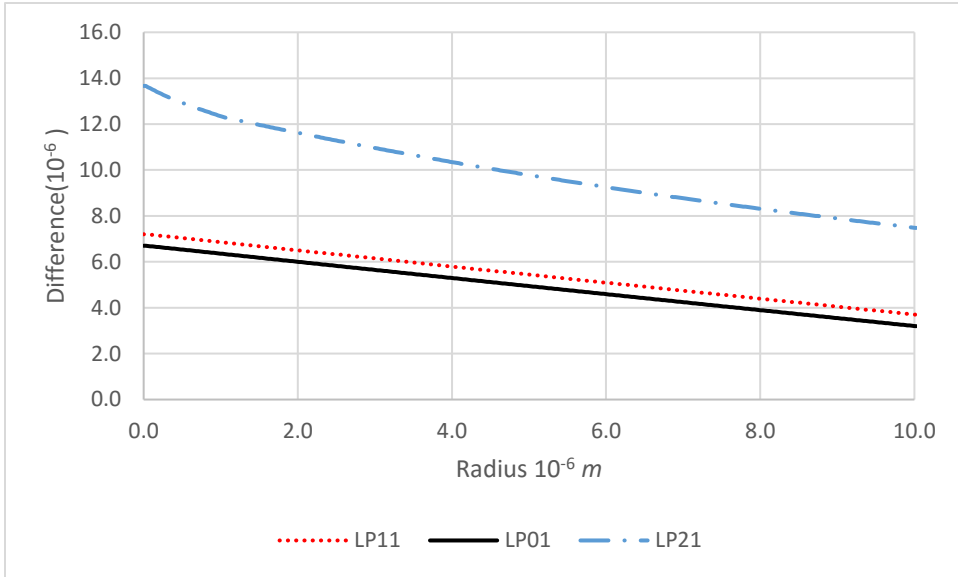


Figure 4.5: Difference among simulated fields from vector and scalar wave for LP₀₁, LP₁₁ and LP₂₁ modes.

(Figure 4.6) below shows the error in n_{eff} values for the approximated profile of 5 layers with TMM with respect to those obtained from FDM for the vortex profile.

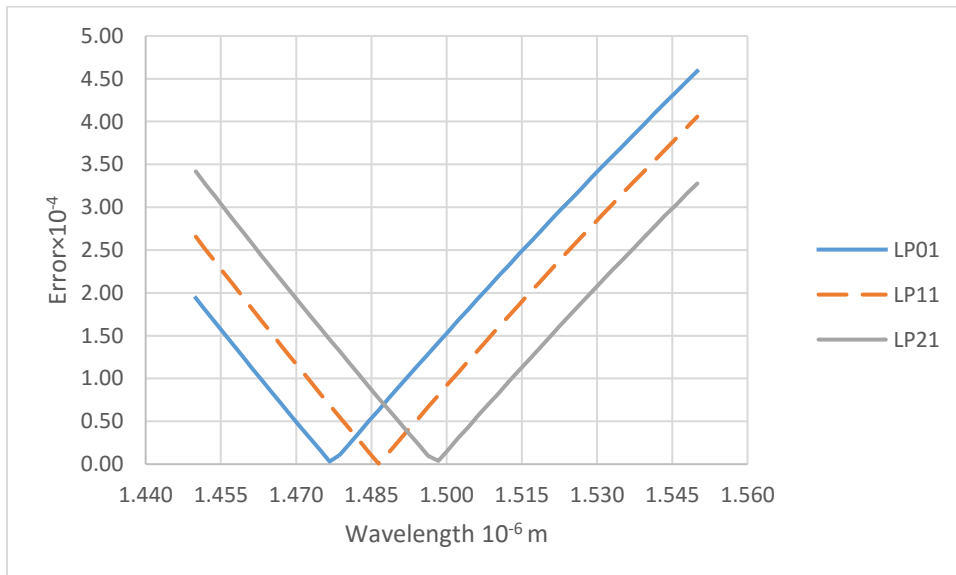


Figure 4.6: Effective index error between vortex fiber profile and approximated profile.

So far, we approximated the vortex profile with 5 layers. In order to get more accurate results, we increase the number of layers to be very close to the structure of vortex fiber and observe the convergence of n_{eff} values for LP₀₁, LP₁₁ and LP₂₁ modes to n_{eff} values for vortex fiber with FDM. We increased the number of layers starting from two layers then four, eight, eleven, fourteen, seventeen and twenty layers in the core region. The final approximation was obtained with twenty three layers in total , as shown in (Figure 4.7).

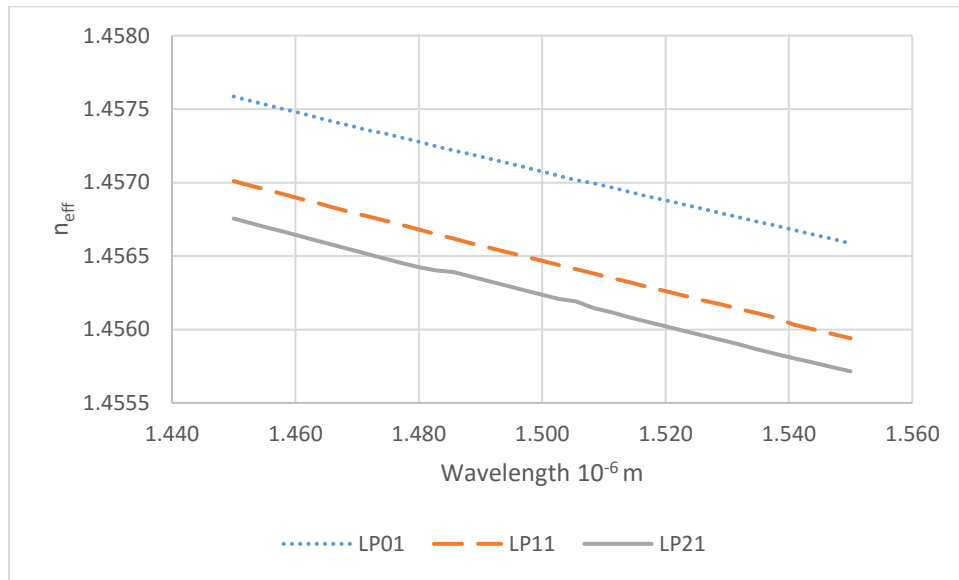


Figure 4.7: Effective index of the approximated profile with twenty layers in core region.

(Figures 4.9 and 4.10) show the differences in n_{eff} values for the approximated profile when we have a different number of layers in approximated profile. We increased number of layers in approximated profile up to 20 layers total for solving waveguide equation to get n_{eff} values. We further calculated the error based on Eq. (4.3) below for n_{eff} values from the approximated profile

with respect to those of the vortex profile. Particularly, the error value is on the order of 10^{-6} for approximated profiles with twenty layers and eighteen layers as shown in Table 4.2, it shows the differences among approximated profiles with various number of layers for LP₀₁, LP₁₁ and LP₂₁ modes. We noticed the decrease in variations of n_{eff} values obtained from TMM as the number of layers in the approximated profile increases. Therefore, we have demonstrated that TMM converges with better-approximated profiles mimicking the vortex profile, and the resulting n_{eff} values are very close to those computed by FDM.

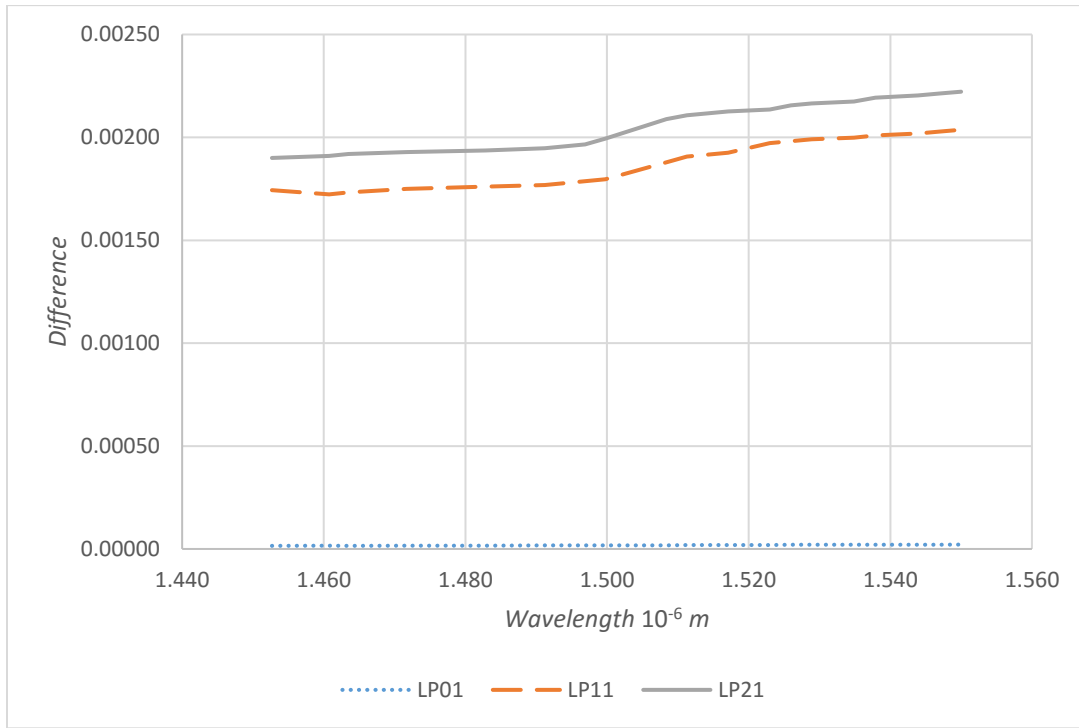


Figure 4.8: Difference between the approximated profile with six layers and the one with eight layers.

$$Difference = \frac{n_{eff}(Vortex\ Fiber - FDM) - n_{eff}(Approximated\ Fiber - TMM)}{n_{eff}(Vortex\ Fiber - FDM)} \quad (4.3)$$

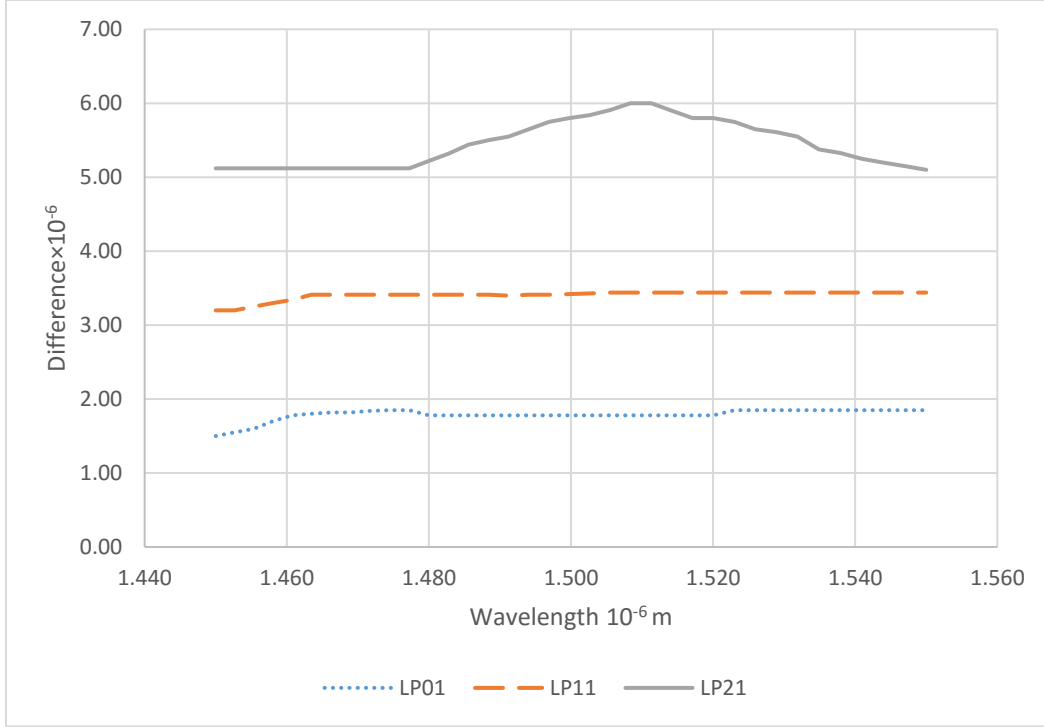


Figure 4.9: Difference between the approximated profile with fifteen layers and the one with eighteen layers.

Differences	LP ₀₁	LP ₁₁	LP ₂₁
Between 6 layers and 8 layers	4.32×10^{-5}	1.8×10^{-3}	2.10×10^{-3}
Between 8 layers and 10 layers	4.12×10^{-5}	8.00×10^{-4}	9.53×10^{-4}
Between 10 layers and 13 layers	1.65×10^{-5}	1.04×10^{-4}	2.14×10^{-4}
Between 13 layers and 15 layers	1.99×10^{-5}	6.86×10^{-6}	1.24×10^{-4}
Between 15 layers and 18 layers	1.85×10^{-6}	3.49×10^{-6}	5.44×10^{-6}
Between 18 layers and 20 layers	6.86×10^{-7}	1.37×10^{-6}	1.37×10^{-6}

Table 4.2: Differences among approximated profile at $\lambda=1.55\mu\text{m}$

4.2 Number of Guided Modes

As mentioned previously, the solution of vector wave equation is represented by modes. Mode index $l = 0$ represents meridional modes that correspond to transverse electric TE_{0m} field or transverse magnetic TM_{0m} field. When $l \neq 0$, it corresponds to hybrid mode that has longitudinal field component, and is labeled as HE_{lm} or EH_{lm} depending on which field (E or H) is more dominant.

More than one parameter controls the number of guided modes in an optical fiber such as refractive index of the core and cladding which depends on the doping, the core radius, and cladding diameter. We estimated the number of guided mode propagating in the fiber with an approximated profile (4-layers profile) and we compared it with the vortex fiber, as we see in (Figure 4.10) below. Based on the vortex profile, the cladding diameter was changed from $80\mu\text{m}$ to $160\mu\text{m}$ in order to get more guided modes.

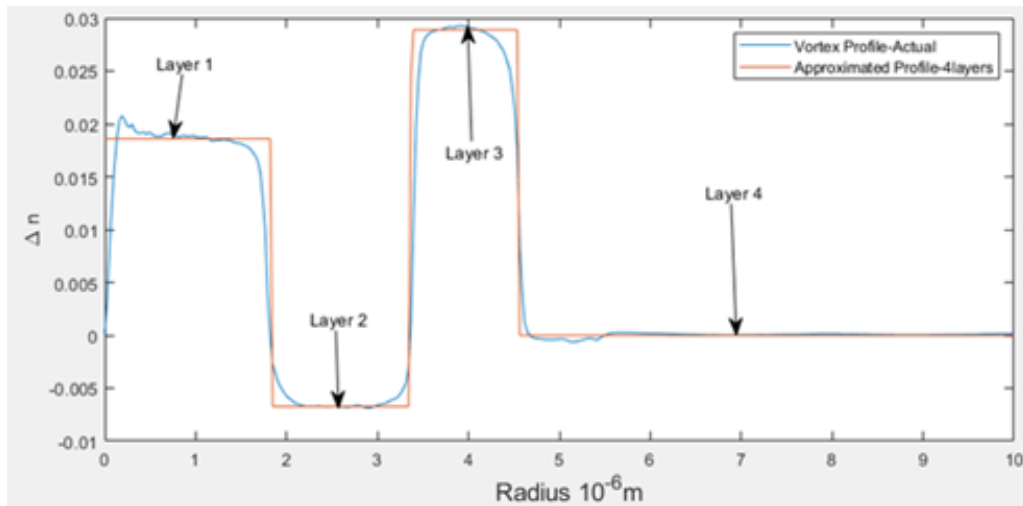


Figure 4.10: Measured and approximated profiles at $\lambda=1.55\mu\text{m}$.

Since we know that the number of modes in the step index fiber depends on more than one parameter such as refractive index of the core, cladding, and radius of the core, we formulated a fitting equation using approximated profile with 10 layers to predict the number of mode M based on various fiber parameters:

$$M = 1.8V^4 - 14V^3 + 35V^2 - 25V + 6.1 \quad (4.4)$$

where:

$$\text{the normalized frequency } V = k_0 a \sqrt{n_1^2 - n_{avg}^2} \quad (4.5)$$

$$n_{avg} = \frac{n_2 + n_3 + n_4}{3} \quad (4.6)$$

n_1 is the refractive index of the core region, and n_2 , n_3 , and n_4 are the refractive indices of cladding area. a is the radius of the core and k_0 is the wave number. Based on Eq. (4.4), we can obtain the number of guided modes when we changed the radius of the fiber expressed in terms of V as shown in (Figure 4.11) below. Eq. (4.4) is valid only for the fiber with cladding diameter within the range of $35\mu\text{m}$ to $350\mu\text{m}$ or $0.4 < V < 3.5$. (Figure 4.12) shows the error between number of guided modes M obtained from FDM (Exact M curve) and that of the fitting equation obtained from Eq. (4.4) (Approximated M) with approximated profile with 10 layers.

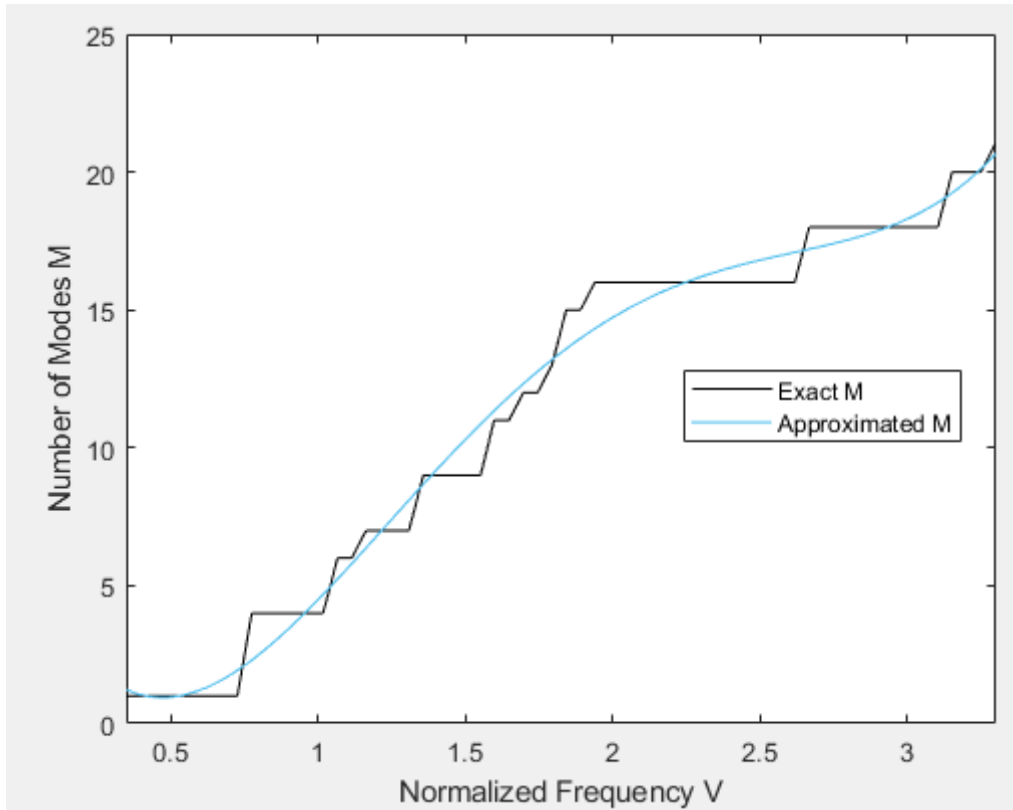


Figure 4.11: Number of guided modes (Exact M) using Eq. (4.4) and (Approximated M) with approximated profile with 10 layers at $\lambda=1.55\mu\text{m}$

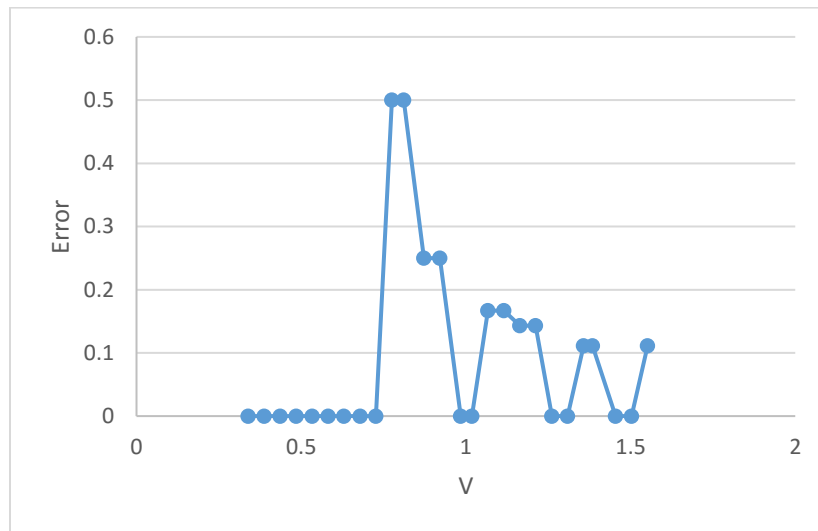


Figure 4.12: Error in M using approximated profile with 10 layers at $\lambda=1.55\mu\text{m}$.

4.3 Dispersions in Optical Fibers

In general, there are two kinds of fiber dispersion: material and waveguide dispersions. The first two types of dispersion are attributable to the frequency dependence of the propagation velocities, and constitute the group velocity dispersion (GVD).

In essence, while optimizing the vortex fiber by tweaking the structure of the profile, the main factor to define an optimizing profile is GVD. We aim to minimize the GVD of LP₂₁ mode by modifying the profile based on adjusting doping for fiber core and cladding. Since the refractive index changes with the concentration of the doped material, it enables the tuning of the material dispersion value. By playing with the fiber structure, i.e. radii of cladding and core, we can get reasonable control of the waveguide dispersion. At the end, we can get an overall minimum dispersion (GVD) if the two types of dispersion can cancel each other.

The wavelength-dependent of the refractive index can be modeled with three different models; model A is introduced by the Sellmeier formula [40]

$$n(\lambda) = \sqrt{1 + \sum_{i=1}^3 A_i \cdot \frac{\lambda^2}{\lambda^2 - \lambda_i^2}} \quad (4.7)$$

where A_i and λ_i are Sellmeier coefficients, experimentally determined [40]. This equation is typically used to characterize the dispersion in glasses by the optical science researchers and industry.

Particularly, the refractive index of fused silica (SiO₂) or fused quartz can be determined with the following Sellmeier equation [41] with the coefficients that are valid at 20°C for wavelength 0.21 μm to 3.71 μm.

$$n^2 - 1 = \frac{0.6961663\lambda^2}{\lambda^2 - 0.0684043^2} + \frac{0.4079426\lambda^2}{\lambda^2 - 0.1162414^2} + \frac{0.8974794\lambda^2}{\lambda^2 - 9.896161^2} \quad (4.8)$$

Coefficients in Eq. (4.8) need to be augmented or modified for various dopants (adding of other chemicals) in different concentrations. We add GeO_2 , P_2O_5 or TiO_2 to increase the refractive index; we can add B_2O_3 or fluorine (F) to decrease the refractive index [42]. Table 4.3 shows the coefficient of the Sellmeier equation at certain concentrations [41] of Germania (GeO_2) doping.

Sellmeier Coefficients	Silica SiO_2 (100%)	Germania (13.5% GeO_2) + Silica SiO_2 (86.5%)	Germania GeO_2 (100%)
A_1	0.69616630	0.711040	0.80686642
A_2	0.40794260	0.451885	0.71815848
A_3	0.89747940	0.704048	0.85416831
λ_1	0.06840430	0.064270	0.068972606
λ_2	0.11624140	0.129408	0.15396605
λ_3	9.8961610	9.425478	11.821931

Table 4.3: Coefficient of Sellmeier equation at certain doping concentration of GeO_2 [41,45]

Table 4.4 shows the values of the refractive indices at different concentrations of GeO_2 . Since the GeO_2 is the most common chemical dopant in glass fiber for increasing the refractive index; we consider its application in modifying the index profile of the fiber. However, it cannot be more than 21%; otherwise, the crystalline structure of the glass will be broken.

GeO_2 (mole%)	Refractive Index at $1.55\mu m$ – with Eq. (4.9)	Refractive Index at $1.55\mu m$ -with Eq. (4.10)
A) GeO_2 (3.1%)	1.4487	1.4487
B) GeO_2 (8.7%)	1.4529	1.4571
C) GeO_2 (11.2%)	1.4600	1.4608
D) GeO_2 (12.0%)		1.4620
E) GeO_2 (13.0%)		1.4634
F) GeO_2 (13.5%)	1.4656	1.4657
G) GeO_2 (14.0%)		1.4649

H) GeO ₂ (14.5%)		1.4657
I) GeO ₂ (15.0%)	1.4652	1.4664
J) GeO ₂ (19.2%)	1.4715	1.4726

Table 4.4: Refractive indices values with different doping concentrations

Fleming proposed another model, model B [45] Eq. (4.9) used to calculate the refractive index in case we have different GeO₂ doping concentrations. It is based on a simple linear relationship between the Sellmeier coefficients of silica and Germania. Table 4.3 shows the coefficients of the model B.

$$n^2 - 1 = \sum_{i=1}^3 \frac{[A_{Si} + X(A_{Gi} - A_{Si})]\lambda^2}{\lambda^2 - [\lambda_{Si} + X(\lambda_{Gi} - \lambda_{Si})]^2} \quad (4.9)$$

where A_{Si} , A_{Gi} , λ_{Si} and λ_{Gi} are Sellmeier coefficients of 100% Si and 100% GeO_2 as seen in table 4.3; X is the molar percentage concentration of GeO_2 .

The third model proposed by Claussius-Mossotti interpolation [46] is used for calculating the refractive index in case we have different percentage of Fluorine doped with Silica. This model shows in Eq. (4.10) can calculate the refractive index at $X=1\%$ or at $X=2\%$ [42], where X is the molar concentration of the dopant. Table 4.5, shows the coefficient of model C.

Material	Coefficient	$i = 1$	$i = 2$	$i = 3$
Silica	A_{Si}	0.2045154578	0.06451676258	0.1311583151
	$z_{Si}(\mu m)$	0.06130807320	0.1108859848	8.964441861
Germania	B_i	-0.1011783769	0.1778934999	-0.106 417 958 1
Fluorine	B_i	-0.05413938039	-0.1788588824	-0.07445931332

Table 4.5: Coefficients of Claussius-Mossotti interpolation [46]

$$\frac{n^2 - 1}{n^2 + 1} = \sum_{i=1}^3 \frac{[A_{Si} + XB_i]\lambda^2}{\lambda^2 - z_{Si}^2} \quad (4.10)$$

where z_{si} is the coefficient of oscillator wavelength of silica where $i = 1, 2$ and 3 as shown in Table 4.5 above [46].

4.3.1 Material Dispersion

The material dispersion is an intrinsic property of the material. It is a phenomenon where the interaction of materials with light causes the light wave to spread out in time, i.e. affecting the bandwidth of the signal carried by the wave and detriment to optical communications. Generally, material dispersion is measured in terms of the amount of pulse broadening per unit length of the fiber per bandwidth of the signal. As the refractive index of a material depends on the wavelength, each frequency component travels at a slightly different speed. The longer is the propagation distance; broader will be the pulse. After a long distance, the pulses will overlap, and the information will be corrupted. Hence, the material dispersion limits rate of data transmission.

Since glass is a dispersive medium and is a major material component for optical fibers, the material dispersion is an important topic in optical communications. Dispersion in the glass fiber depends on the doping concentrations of different material like GeO_2 , P_2O_5 , B_2O_3 , and F . By choosing a suitable level of the doping, we can control the material dispersion in optical fibers; Eq. (4.11) is applied for calculation of the material dispersion in optical fiber, where c is the speed of light, and its unit is in picoseconds per nanometer-kilometer (ps/(nm-km)):

$$D_{material} = D_m = -\frac{1}{c\lambda} \left(\lambda^2 \frac{\partial^2 n}{\partial \lambda^2} \right) \quad (4.11)$$

Table 4.6 shows D_m calculated with the refractive index of glass with various levels of doping applying the original Sellmeier equations Eq. (4.7) with coefficients from Refs. 40 and 41,

Eq. (4.9) with Fleming approximated coefficients and Eq. (4.10) with coefficients based on Claussius-Mossotti interpolation.

GeO ₂ (mole%)	D _m (ps/nm-km) Model A-Eq. (4.7) and coefficients from Ref.[40]	D _m (ps/nm-km) Model A-Eq. (4.7) and coefficients from Ref.[40]	D _m (ps/nm-km) Model B-Eq. (4.9)	D _m (ps/nm-km) Model C-Eq. (4.10)
3.1%	21.14		20.74	20.42
4.1%	19.67			
7.9%	20.08			
8.7%		18.19	18.67	17.72
11.2%		17.62	17.75	16.5
12.0%			17.46	16.11
13.0%			17.1	15.62
13.5%	10.07		16.91	15.37
14.0%			16.73	15.13
14.5%			16.55	14.88
15.0%		15.00	16.37	14.64
19.2%		13.13	14.85	12.56

Table 4.6: Material dispersion with different concentrations using A, B and C models.

4.3.2 Waveguide Dispersion

The waveguide dispersion depends on the structure of the optical fiber. In this kind of dispersion, the index change across waveguide means that different wavelengths have different delays. It can be calculated with the effective index of the mode (n_{eff}).

$$D_{waveguide} = D_{W.G} = -\frac{1}{c\lambda} \left(\lambda^2 \frac{\partial^2 n_{eff}}{\partial \lambda^2} \right) \quad (4.12)$$

Specifically, $n_{eff} = n_{eff}^{lm}$ for a certain mode with indices of l and m depends on the propagation constant β^{lm} as shown in Eq. (4.13) below. So the electric field and propagation constant depend on the waveguide structure and the angular frequency.

$$n_{eff} = \frac{c\beta^{lm}}{\omega} \quad (4.13)$$

For the mode to be guided through the fiber, the effective index of that mode is always between the core index and the cladding index in optical fiber profile. To calculate the waveguide dispersion, it can be performed with the equation below [47]:

$$\left(\frac{\partial n_{eff}}{\partial \omega}\right)_{waveguide} = \frac{1}{\omega n_{eff}} (n_2^2 + \Gamma_1 [n_1^2 - n_{avg}^2] - n_{eff}^2) \quad (4.14)$$

where n_1 is the core index, n_{avg} is the average cladding index and Γ_1

$$\Gamma_1 = \frac{\int_0^a \vec{E}^*(\rho) \cdot \vec{E}(\rho) d\rho}{\int_0^\infty \vec{E}^*(\rho) \cdot \vec{E}(\rho) d\rho} \quad (4.15)$$

is the confinement factor and

$$\vec{E}(\rho) = E_\rho(\rho) \hat{\rho} + E_\theta(\rho) \hat{\theta} + E_z(\rho) \hat{z} \quad (4.16)$$

Using Eq. (4.16) below, we can compare the numerical value of D_{WG} using Eq. (4.11) with the calculated value of D_{WG} with Eq. (4.13):

$$D_{W.G} = \frac{-2\pi}{\lambda^2} \left\{ 2 \frac{\partial n_{eff}}{\partial \omega} + \omega \frac{\partial^2 n_{eff}}{\partial \omega^2} \right\} \quad (4.17)$$

Finally, we can find the intra-modal or GVD dispersion as:

$$D_{GVD} = D_{WG} + D_m \quad (4.18)$$

4.3.3 Polarization mode Dispersion (D_{PMD})

Polarization mode dispersion (D_{PMD}) is a bit more complex; it originates from a differential arrival time of the polarization components of an input light pulse propagating in an optical fiber. Since the light pulse can always be decomposed into pairs of orthogonal polarization modes, their difference in speed leads to dispersion. The pulse broadening can be estimated from time delay ΔT between the two polarization components during propagation of the pulse. For a fiber with length L , ΔT is given by

$$\Delta T = L|\tau_{gx} - \tau_{gy}| = \left| \frac{L}{v_{gx}} - \frac{L}{v_{gy}} \right| \quad (4.19)$$

where the subscripts x and y identify the two orthogonal polarized modes, v_{gx} and v_{gy} are their group velocities [7]. The D_{PMD} in ps/km is an important factor as data rates on long distance links increases to 40 Gb/s and 100 Gb/s. The dispersion parameter PMD is

$$PMD = \frac{\Delta T}{\sqrt{L}} \quad (4.20)$$

PMD measures the strength and frequency of the imperfections; it varies from fiber to fiber in the range from 0.01 to 10 ps/km^{1/2}. Fibers installed during the 1980s have relatively large D_{PMD} such that $PMD > 0.1$ ps/km^{1/2}. In contrast, modern fibers are designed to have low PMD , typically $PMD < 0.1$ ps/km^{1/2}. The delay caused by D_{PMD} is given by

$$D_{PMD} = PMD\sqrt{L} \quad (4.21)$$

Based on data rate we estimated PMD value [58], the value of PMD is 0.02ps/km^{1/2}.

4.4 Optimizing the Fiber

So far, we approximated the Vortex fiber “*dk11OD105*” by a 5-layers index profile since in previous investigations this profile can guide the fundamental mode LP_{01} and the second order mode LP_{11} only, the total dispersion of LP_{11} is 0.6 ps/nm-km. In this section we have tested 3 different new profiles and compare all of them to decide which one will be the best based on the group velocity dispersion. In this thesis, we are interested in LP_{21} mode, so we attempt to minimize the GVD for this mode as much as possible.

In this section, we considered 3 different profiles: profile A, profile B, and profile C. Their specifications are based on the structure and dispersion.

Fiber A: 4- layers of constant index profile.

We first considered approximation profile with four layers. We increase the refractive indices of these layers by changing the concentrations of GeO_2 up to 20% in the first and third layers, or/and decrease the refractive index of the second layer by adding Fluorine with 1% or 2% concentration. Tables 4.4 and 4.6 showed the effect of the doping concentration on the refractive index and the material dispersion respectively. We calculated all possible combination values of the doping to achieve the best concentration to get better value in the GVD.

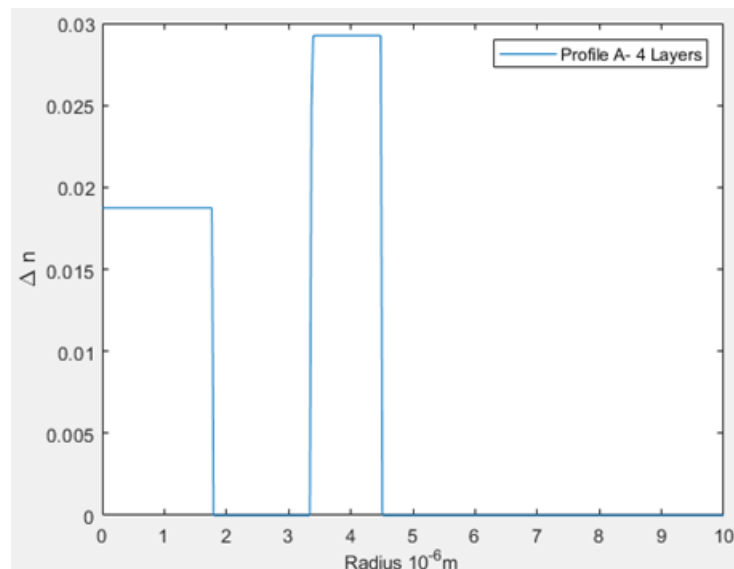


Figure 4.13: Index profile of fiber A, 4-layers step index profile.

On the other hand, we can change the radius of the core region, the radius of the second and third layers to be able to increase the number of guided modes on the optimized profile. The index profile of profile A is:

$$n(r) = \begin{cases} 1.46274 & 0 < r < r_1 \\ 1.444 & r_1 < r < r_2 \\ 1.47325 & r_2 < r < r_3 \\ 1.444 & r > r_3 \end{cases} \quad (4.22)$$

where $r_1 = 1.766\mu\text{m}$, $r_2 = 3.341\mu\text{m}$ and $r_3 = 4.51\mu\text{m}$.

For this multilayer fiber model, we consider the first layer as a core region with index n_1 and we took the average of other layers, to define an equivalent cladding layer with index of n_{avg} .

Fiber B: 4-layers index profile with a graded index core.

The idea of fiber B is to replace the step index of the first layer with a graded index profile as shown in (Figure 4.14). The index profile of fiber B is:

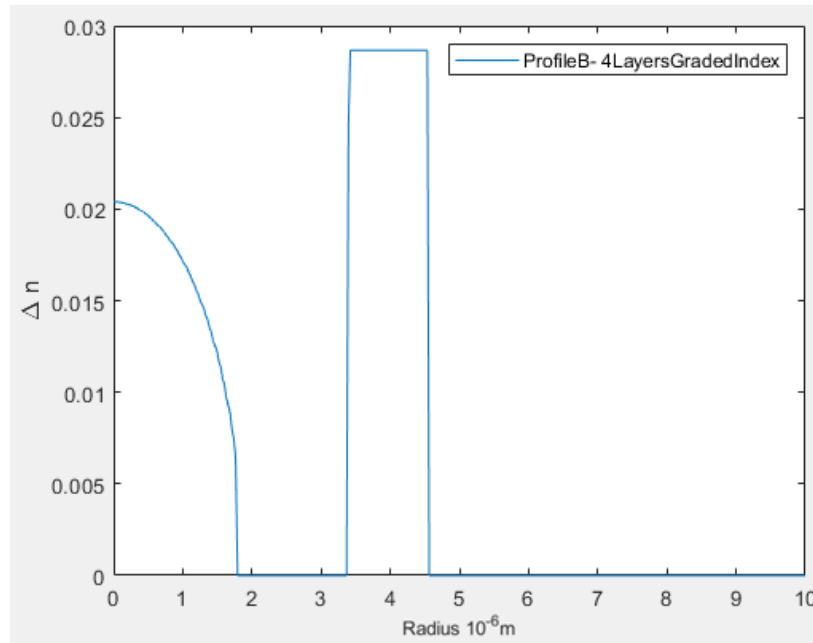


Figure 4.14: Index profile of fiber B, 4-layers index profile with a graded index core.

$$n(r) = \begin{cases} n_1 \left(1 - \Delta \left(\frac{r}{a}\right)^2\right) & 0 < r < r_1 \\ 1.444 & r_1 < r < r_2 \\ 1.4725 & r_2 < r < r_3 \\ 1.444 & r > r_3 \end{cases} \quad (4.23)$$

where

$$\Delta = \frac{(n_1^2 - n_2^2)}{2n_1^2} \quad (4.24)$$

$r_1 = a = 1.793\mu\text{m}$, $r_2 = 3.368\mu\text{m}$, $r_3 = 4.563\mu\text{m}$ and $n_1 = 1.465$.

With TMM, we numerically calculated the effective index of this profile, and then determined the waveguide dispersion with Eq. (4.12).

Fiber C: 3-layers index profile with a graded index core.

In this profile, we increased the radius of the core region to obtain an appropriate level of waveguide dispersion to achieve a lower GVD value. (Figure 4.15) shows the profile of fiber C.

The expression of the index profile of fiber C is:

$$n(r) = \begin{cases} n_1 \left(1 - \Delta \left(\frac{r}{a}\right)^2\right) & 0 < r < r_2 \\ 1.4725 & r_2 < r < r_3 \\ 1.444 & r > r_3 \end{cases} \quad (4.25)$$

where $r_2 = a = 3.368\mu\text{m}$, $r_3 = 4.536\mu\text{m}$, $n_1 = 1.465$ and $n_2 = 1.444$.

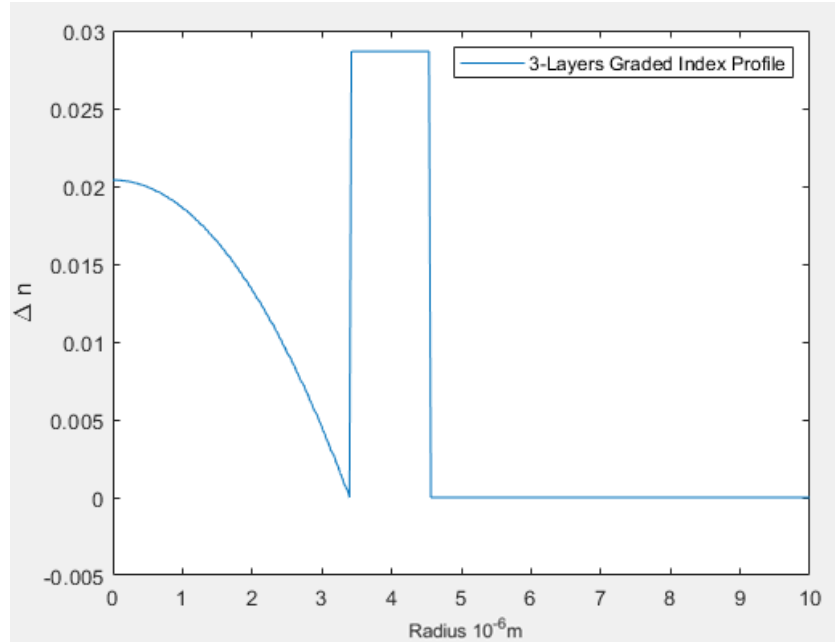


Figure 4.15: Index profile of fiber C, 3-layers with a graded index core.

We followed the same procedure for profile B for computing the dispersion of profile C.

Calculations for fiber A:

Results for fiber A under various d 's where d relates to the doping concentrations. When $d = [13.9\% \ 0\% \ 19.7\%]$ so the concentrations of GeO_2 in the first, second and third layers are 13.9%, 0 and 19.7% respectively. On another hand, we tried different percentage values for doping to calculate the minimum value for GVD, e.g. in case of $d = [13.7\%, \ 0\%, \ 19\%]$ as shown below.

	D _{WG} -numerical (ps/nm-km)	D _{WG} -calculated (ps/nm-km)	GVD (ps/nm-km)
<i>LP₀₁</i>	-0.4366	-0.5324	16.0325
<i>LP₁₁</i>	-3.1739	-2.9720	12.5648
<i>LP₂₁</i>	-28.9721	-27.3126	-12.3367
<i>D_m</i>	16.7669 (1st) 15.64 (3rd)	16.7669 (1st) 15.64 (3rd)	16.7669 (1st) 15.64 (3rd)

Table 4.7: Total dispersion in fiber A; d = [13.9% 0% 19.7%]

	D _{WG} -numerical (ps/nm-km)	D _{WG} -Calculated (ps/nm-km)	GVD (ps/nm-km)
<i>LP₀₁</i>	1.8484	1.58014	18.29156
<i>LP₁₁</i>	-2.2911	-1.6747	12.9161
<i>LP₂₁</i>	-34.8014	-33.5739	-19.2439
<i>D_m</i>	16.8397 (1st) 14.92 (3rd)	16.8397 (1st) 14.92 (3rd)	16.8397 (1st) 14.92 (3rd)

Table 4.8: Total dispersion in fiber A; d = [13.7%, 0%, 19%].

Calculations for fiber B:

	D _{WG} -numerical (ps/nm-km)	D _{WG} -calculated (ps/nm-km)	GVD (ps/nm-km)
<i>LP₀₁</i>	-4.6141	-4.2475	12.3191
<i>LP₁₁</i>	-4.6221	-4.3321	11.1039
<i>LP₂₁</i>	-33.9089	-33.7918	-18.3018

D_m	16.7669(1st) 15.64 (3rd)	16.7669(1st) 15.64 (3rd)	16.7669(1st) 15.64 (3rd)
-------	--------------------------------	--------------------------------	--------------------------------

Table 4.9: Total dispersion in fiber B; $d = [13.9\% \ 0\% \ 19.7\%]$.

	D _{WG} -numerical (ps/nm-km)	D _{WG} -Calculated (ps/nm-km)	GVD (ps/nm-km)
LP_{01}	-2.2742	-2.1541	14.6015
LP_{11}	-3.7268	-3.2139	11.3951
LP_{21}	-39.8503	-39.5286	-25.0191
D_m	16.8397(1st) 14.92 (3rd)	16.8397(1st) 14.92 (3rd)	16.8397(1st) 14.92 (3rd)

Table 4.10: Total dispersion in fiber B; $d = [13.7\%, \ 0\%, \ 19\%]$.

Calculations for fiber C:

	D _{WG} -numerical (ps/nm-km)	D _{WG} -calculated (ps/nm-km)	GVD (ps/nm-km)
LP_{01}	13.6764	13.1943	29.8915
LP_{11}	10.0177	9.5788	25.4124
LP_{21}	-15.3615	-15.1998	0.3432
D_m	16.7669 (1st) 15.64 (3rd)	16.7669 (1st) 15.64 (3rd)	16.7669 (1st) 15.64 (3rd)

Table 4.11: Total dispersion in fiber C; $d = [13.9\% \ 13.9\% \ 19.7\%]$.

	D _{WG} -Numerical (ps/nm-km)	D _{WG} -Calculated (ps/nm-km)	GVD (ps/nm-km)
<i>LP₀₁</i>	14.6273	14.2351	29.9551
<i>LP₁₁</i>	10.6490	10.1249	25.2449
<i>LP₂₁</i>	-19.3555	-18.9829	4.1629
<i>D_m</i>	16.8397 (1st) 14.92 (3rd)	16.8397 (1st) 14.92 (3rd)	16.8397 (1st) 14.92 (3rd)

Table 4.12: Total dispersion in fiber C; $d = [13.7\%, 13.7\%, 19\%]$.

The merit for the best fiber is based on the minimum value of GVD calculated with Eq. (4.18).

Table 4.13, shows us the results of GVD; based on that, fiber C is the best profile to guide the third mode since the GVD is 0.3432 (ps/nm-km).

	Fiber A – GVD (ps/nm-km)		Fiber B – GVD (ps/nm-km)		Fiber C - GVD (ps/nm-km)	
	$d = [13.9\%, 0\%, 19.7\%]$	$d = [13.7\%, 0\%, 19\%]$	$d = [13.9\%, 0\%, 19.7\%]$	$d = [13.7\%, 0\%, 19\%]$	$d = [13.9\%, 13.9\%, 19.7\%]$	$d = [13.7\%, 13.7\%, 19\%]$
<i>LP₀₁</i>	16.3303	18.6881	12.1528	14.4927	29.8915	29.9551
<i>LP₁₁</i>	12.4661	12.6289	11.0179	11.9132	25.4124	25.2449
<i>LP₂₁</i>	-13.3321	19.8814	-18.2689	-24.2103	0.3432	4.1629

Table 4.13: GVD in fiber A, B and C.

4.4.1 Dispersion - Profile A

In this section, we determine a modeling equation for the waveguide dispersion of fibers under consideration as a function of core radius, refractive index, and wavelength. This equation based on approximating the waveguide dispersion in Eq. (4.14) with a simplified expression of the field in Eq. (4.16). Then the approximated equation is obtained by fitting the plot of Eq. (4.17), it's

calculated with approximated Eq. (4.14) with a regression function in terms of normalized frequency V for each fiber and each mode as below.

	D _{WG} computed with Eq. (4.12) (ps/nm-km) d = [13.9% 0% 19.7%]	D _{WG} computed with Eq. (4.17) (ps/nm-km) d = [13.9% 0% 19.7%]	Error 1	D _{WG} computed with (Eqs. (4.28) - (4.30)) (ps/nm-km) d = [13.9% 0% 19.7%] V=1.1598015*10 ⁻³	Error 2
LP ₀₁	-0.4366	-0.3	0.31287	-0.17952	0.588
LP ₁₁	-3.1739	-3.3428	0.05321	-3.241	0.0211
LP ₂₁	-28.9721	-29.86	0.0306	-29.8664	0.0308

Table 4.14: Calculated and approximated waveguide dispersion for fiber A.

$$Error\ 1 = \frac{D_{WG}(Eq.4.11) - D_{WG}(Eq.4.16)}{D_{WG}(Eq.4.11)} \quad (4.26)$$

$$Error\ 2 = \frac{D_{WG}(Eq.4.11) - D_{WG1,2}}{D_{WG}(Eq.4.11)} \quad (4.27)$$

$$\text{where } D_{WG1,2} = \begin{cases} D_{WG1} & \text{for } LP_{01}, LP_{11} \\ D_{WG2} & \text{for } LP_{21} \end{cases}$$

4.4.2 Dispersion - Profile B

	D _{WG} computed with Eq. (4.12) (ps/nm-km) d = [13.9% 0% 19.7%]	D _{WG} computed with Eq. (4.17) (ps/nm-km) d = [13.9% 0% 19.7%]	Error 1	D _{WG} computed with (Eqs. (4.28) - (4.30)) (ps/nm-km) V=1.1598015×10 ⁻³ d = [13.9% 0% 19.7%]	Error 2
LP ₀₁	-4.6141	-4.7335	0.0258	-4.6	0.0305
LP ₁₁	-4.6221	-4.7224	0.0217	-4.62	0.00454
LP ₂₁	-33.9089	-33.8872	0.00064	-34	0.0026

Table 4.15: Calculated and approximated waveguide dispersion for fiber B.

4.4.3 Dispersion - Profile C

	D _{WG} computed with Eq. (4.17) (ps/nm-km) d = [13.9% 13.9% 19.7%]	D _{WG} computed with Eq. (4.17) (ps/nm-km) d = [13.9% 13.9% 19.7%]	Error 1	D _{WG} computed with (Eqs. (4.28) - (4.30)) (ps/nm-km) V = 2.2271 × 10 ⁻³ d = [13.9% 13.9% 19.7%]	Error 2
LP ₀₁	13.6764	13.5971	0.00579	13.60	0.0055
LP ₁₁	10.0177	9.91025	0.0107	10	0.00177
LP ₂₁	-15.3615	-15.375175	0.00089	-15.36	0.000976

Table 4.16: Calculated and approximated waveguide dispersion for fiber C.

The waveguide dispersion equation for Fiber A, B and C of LP₀₁ and LP₁₁ modes is:

$$D_{WG1} = h V + b \quad (4.28)$$

$$V = k_0 a \sqrt{(n_1^2 - n_{avg}^2)} \quad (4.29)$$

Where V is the normalized frequency, a is the core radius, n_1 is the refractive index of the core and n_{avg} is the average refractive index of the second, third and fourth layers, k_0 is the wave number.

The waveguide dispersion equation for Fiber A, B and C is LP₂₁:

$$D_{WG2} = h V^2 + b V + c \quad (4.30)$$

where the parameters or constants h , b and c as below:

	H	b	c
LP ₀₁ –Fiber A	-1.5494×10^5	179.56	
LP ₁₁ –Fiber A	-1.1831×10^5	134.01	
LP ₂₁ –Fiber A	-1.0034×10^9	2.4891×10^6	-156
LP ₀₁ –Fiber B	-97806	189.63	
LP ₁₁ –Fiber B	-68199	130.83	
LP ₂₁ –Fiber B	-4.1045×10^8	1.7449×10^6	-1880.3
LP ₀₁ –Fiber C	-60226	147.83	
LP ₁₁ –Fiber C	-53504	129.21	

LP ₂₁ –Fiber C	$- 2.0766 \times 10^8$	9.8752×10^5	$- 1184.7$
---------------------------	------------------------	----------------------	------------

Table 4.17: Constants of waveguide dispersion for fibers A, B and C.

4.5 Bandwidth of Fiber C

In optical fiber, the maximum transmission distance is limited not only by the length of the fiber but also by total dispersion. From Eq. (4.32), the bandwidth of optical fiber depends on the total dispersion, this means the larger the total dispersion and the longer the distance, the lower the transmittable bit rate. For fiber C, the GVD of the third group LP₂₁ is equal to $0.3432 \text{ psec.nm/km}$.

The total dispersion of the optical fiber is given by:

$$D_{total}^2 = D_{GVD}^2 \Delta\lambda^2 + D_{PMD}^2 / L^2 \quad (4.31)$$

where $\Delta\lambda$ is the linewidth (in nm) of the light source. For an external cavity laser (ECL), $\Delta\lambda$ can be as narrow as 0.4nm. The total dispersion is used for characterizing the fiber's transmission bandwidth. The pulse broadening arising from GVD is proportional to the fiber length L; The fiber bandwidth is defined as:

$$B_{fiber} = \frac{1}{D_{total} L} \quad (4.32)$$

In case if the length of the fiber is 2 km, the expected transmitted bit rate would be equal to 3.6 Tb/sec , compare to the bandwidth in reference [5], they achieved 1.6 Tb/sec using their fiber.

Chapter 5

Computer Generated Hologram

We tout the holographic displays as the ultimate 3-D display because they are the method that can reproduce the exact light wave with the correct wave front from a 3-D object. Using computer-generated holograms (CGH), we can mimic the wave front from any object based on a mathematical description. To capture an actual object onto a hologram, we essentially record the interference pattern between the light scattered by the object and a reference wave. The interference pattern encodes the phase information of the object wave, in addition to its intensity. With the same reference wave, one can play back the recorded 3-D image of the object. For the accurate phase recording, a coherent light source, such as a laser, is required to be the source for both the reference wave and the wave illuminating the object.

5.1 Computer Generated Hologram (CGH)

A practical and versatile method for generating these arbitrary complex fields is based CGHs [6,20-22,29,34-36,55-58]. In particular, the use of phase CGHs is especially convenient because of their relatively high efficiency. It is important to distinguish cell-oriented and point-oriented holograms for encoding complex fields. In general, point-oriented approaches [29,49,50] are more convenient when holograms are implemented with low-resolution pixelated modulators.

In this chapter, we focus on one of the methods for mode generation, CGH. It is a hologram fabricated with digitally generated interference patterns that are printed onto a mask or film. During playback stage, an image of the 3D object can be projected when the CGH is subsequently

illuminated by a suitable light source. In other words, unlike a photograph, a CGH contains both amplitude and phase information of the object [3]. Thus, it can be used to encode phase information to an input beam [2].

The consideration of using CGH to introduce a phase ramp to a Gaussian beam and hence, produces higher order structured beams, i.e. Laguerre-Gaussian beams. The interference of the desired beam structure of a vortex wave (as the object) with a reference plane wave results in an interferogram exhibiting a diffractive forked pattern which carries a phase ramp of $l\theta$ where l is the order of forked pattern or topological charge of the vortex or azimuthal index. Physically, l is the number of twists or spirals the light traveling in complete cycle per wavelength and is always an integer. Its polarity signifies the direction (clockwise or counter-clockwise) of rotation. (Figure 5.1) shows different modes with zero radial index ($m=0$) which relates to the number of dark rings. In (Figure 5.1), the first column is the helical structures, the second one is the phase-front, and the last one is the intensity of the beams [48]. The four rows with nonzero l correspond to optical vortices. As shown by the Figure, a large topological charge leads to a fast spinning of the light around the axis and an increase of the vortex size.

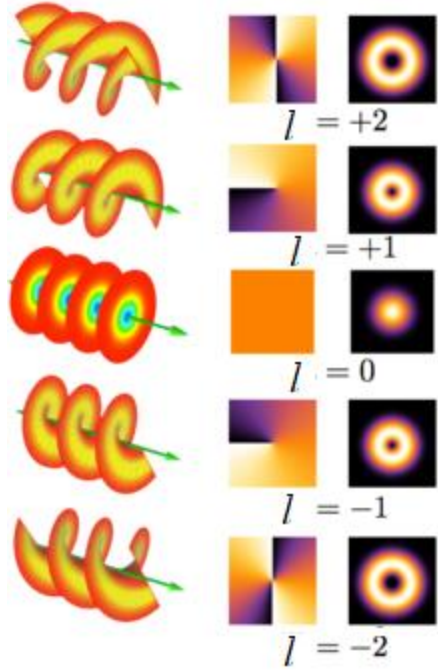


Figure 5.1: Diagram of different modes [51].

The phase profile of the vortex beams as shown in (Figure 5.1). Clearly, for $l = 0$, phase is constant i.e. 0. For $l = 1$ phase goes one complete rotation from $-\pi$ to π in clockwise. For $l = 2$, phase goes one complete rotation from -2π to 2π in clockwise.

(Figure 5.2) shows holograms for different topological charges. The shape of fork depends on the value of l . Hence, the forked pattern is very useful in determining the charge of the optical vortex since we can count the number of missing fringes. For example, for $l = 0$ grating, there is no missing fringe; for $l = 1$ and $l = 2$, one fringe is missing, and two fringes are missing respectively. For a dynamical generation of the vortex with various charges, researchers use spatial light modulators.

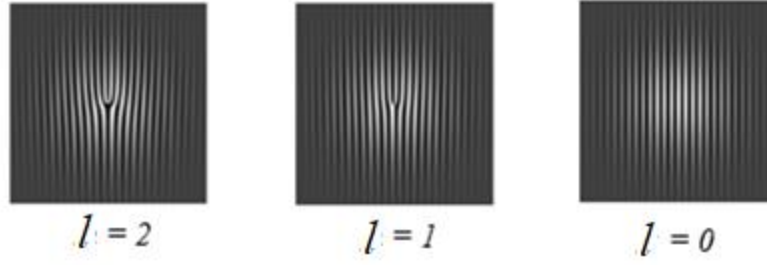


Figure 5.2: Computer generated holograms for $l=0,1$ and 2

In this chapter, we encoded the second mode of the Laguerre-Gaussian beam (LG_{21}) using CGH technique. To see the performance of pixelated CGHs by employing two types of holograms to encode LG_{21} beam. LG_{21} beam can be expressed in polar coordinates (ρ, θ) as:

$$u(\rho, \theta) = C \left(\frac{\sqrt{2}\rho}{w_0} \right)^{|l|} L_m^{|l|} \left(2 \frac{\rho^2}{w_0^2} \right) \exp \left(-\frac{\rho^2}{w_0^2} \right) \exp(jl\theta) \quad (5.1)$$

where $L_m^{|l|}$ is an associated Laguerre polynomial, w_0 is the beam waist radius and C is a normalization constant. In the numerical simulation, the waist radius is $w_0 = 40 \delta x$, and the beam support is a circle of radius $R=128 \delta x$; To be able to encode LG_{21} beam, we can express the complex optical field Eq. (5.1) as:

$$s(x, y) = a(x, y) \exp(j\theta(x, y)) \quad (5.2)$$

where $a(x, y)$ is the amplitude and $\theta(x, y)$ is the phase of the complex field. We have to normalize the amplitude field; the phase range is changing from $-\pi$ to π . The transmittance of the CGH phase expressed as a function of $a(x, y)$ and $\phi(x, y)$ of the encoded field is given as:

$$h(x, y) = \exp(j\Psi(a, \theta)) \quad (5.3)$$

where $\Psi(a, \theta)$ is the phase modulation of the CGH. The good performance of these CGHs is enabled by a significant reduction in the relative intensity of the high-order diffraction field contributions that share the spatial frequency domain of the encoded field [1].

There are two classes of CGHs [1] for encoding LG_{2l} field. To determine the hologram phase modulation $\Psi(a, \theta)$ is based on the representation of $h(x,y)$ with a Fourier series in the domain of θ , so we can represent the CGH transmittance as:

$$h(x, y) = \sum_{q=-\infty}^{\infty} h_q(x, y) \quad (5.4)$$

where:

$$h_q(x, y) = c_q^a \exp(jq\theta) \quad (5.5)$$

$$c_q^a = \frac{1}{2\pi} \int_{-\pi}^{\pi} \exp(j\Psi(\theta, a)) \exp(-jq\theta) d\theta \quad (5.6)$$

After we calculated the integration in Eq. (5.6), we notice the answer of c_q^a is explicitly dependent on the amplitude a and implicitly dependent on the coordinates (x,y) . The signal $s(x,y)$ is recovered from the first-order term $h_1(x,y)$ in the series of Eq. (5.4), if the identity

$$c_q^a = Aa \quad (5.7)$$

is fulfilled for a positive constant A [1]. The necessary conditions to fulfill Eq. (5.7) are given by the following equations:

$$\int_{-\pi}^{\pi} \sin[\Psi(\theta, a) - \theta] d\theta = 0 \quad (5.8)$$

$$\int_{-\pi}^{\pi} \cos[\Psi(\theta, a) - \theta] d\theta = 2\pi Aa \quad (5.9)$$

Based on (Eqs. (5.8) – (5.9)), we determine the appropriate CGHs. Below are the results of testing two classes of CGHs to encode LG_{2l} field are discussed in next section.

5.2 Encoding LP_{21} Beam with CGH Technique

Our main goal is to encode LP_{21} mode, we started with LG_{21} beam, since we assumed LG_{21} to be closer to LP_{21} mode, since both of them have a doughnut shape; in this section, we discussed the construction of CGH of type 2 and 3 for LG_{21} . The phase modulation of type 2 CGH is given by:

$$\psi(a, \theta) = \theta + f(a)\sin(\theta) \quad (5.10)$$

Where $f(a)$ is a factor, it can be determined under the condition of encoding LP_{21} , after we substitute Eq. (5.10) into Eq. (5.3), the phase CGH transmittance is:

$$h(x, y) = \exp(i\theta)\exp(if(a)\sin(\theta)) \quad (5.11)$$

The encoding condition for second mode LG_{21} when:

$$J_1[f(a)] = Aa(x, y) \quad (5.12)$$

where $J_1(x)$ is the first-order Bessel function and $A=0.5819$ corresponds to the maximum value.

From numerical analysis, we plotted the relationship between $a(x, y)$ and $f(a(x, y))$ in (Figure 5.3).

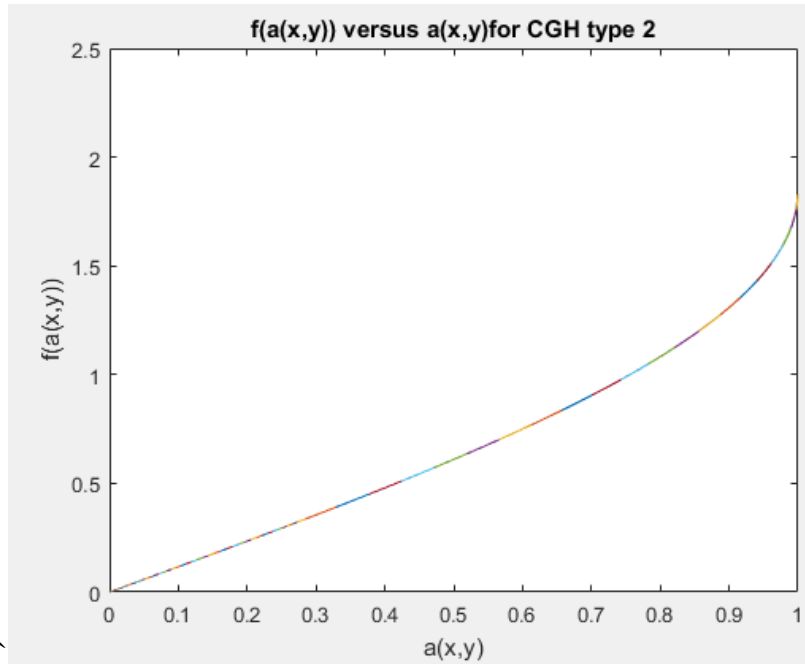


Figure 5.3: Function $f(a)$ versus a for the type 2 CGH of a LG_{21} beam

The corresponding phase distribution for CGH type 2 is shown in (Figure 5.4)

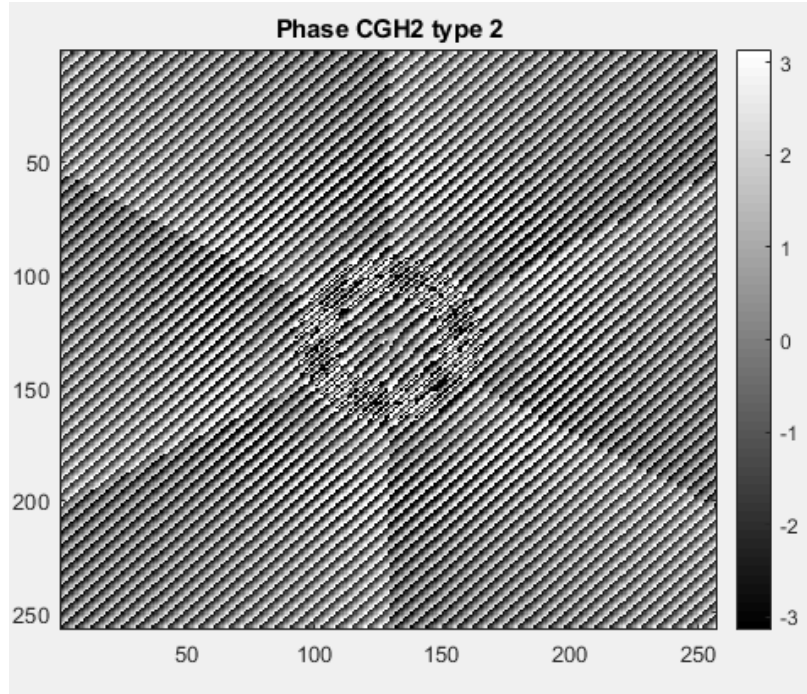


Figure 5.4: Phase distribution of type 2 CGH for LG_{21} beam

The encoded field of the LG_{21} with CGH-type 2 is shown below:

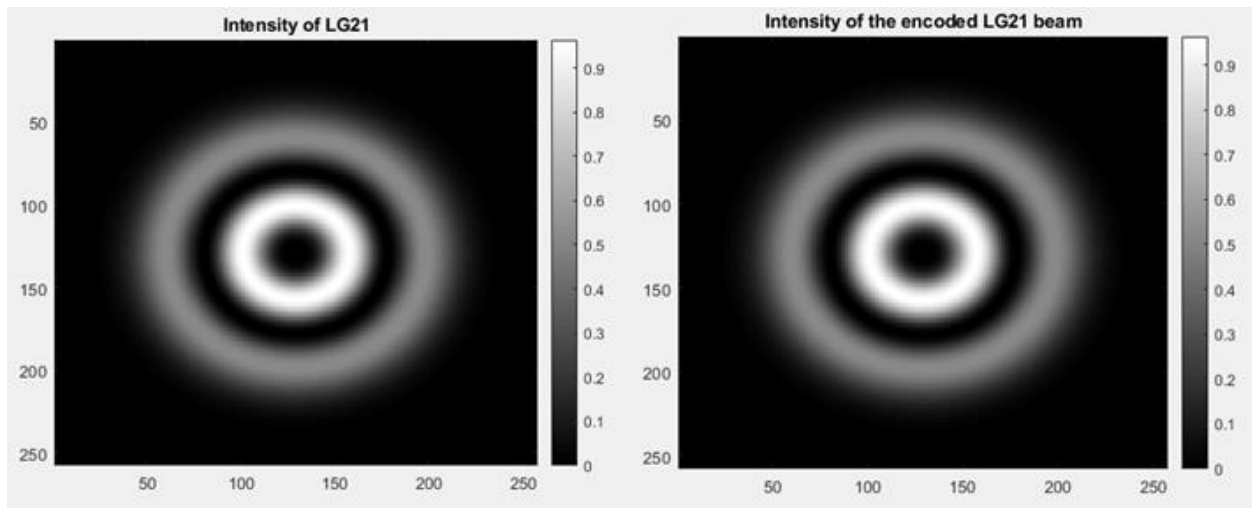


Figure 5.5: Intensity of LG_{21} and intensity distribution of the encoded LG_{21} beam

With numerical data results from TMM for LP₂₁ beam of profile C in chapter 4, we wrote the expression for the beam in form of Eq. (5.2) with amplitude $a(x,y)$ and phase $\theta(x,y)$. We then fitted the numerical data with spline interpolation with low-degree polynomials in each of the intervals, and chose the polynomial pieces such that they fit smoothly together. We used the type 2 CGH to encode the LP₂₁ beam, the phase distribution of the type 2 CGH in this case is shown in (Figure 5.6).

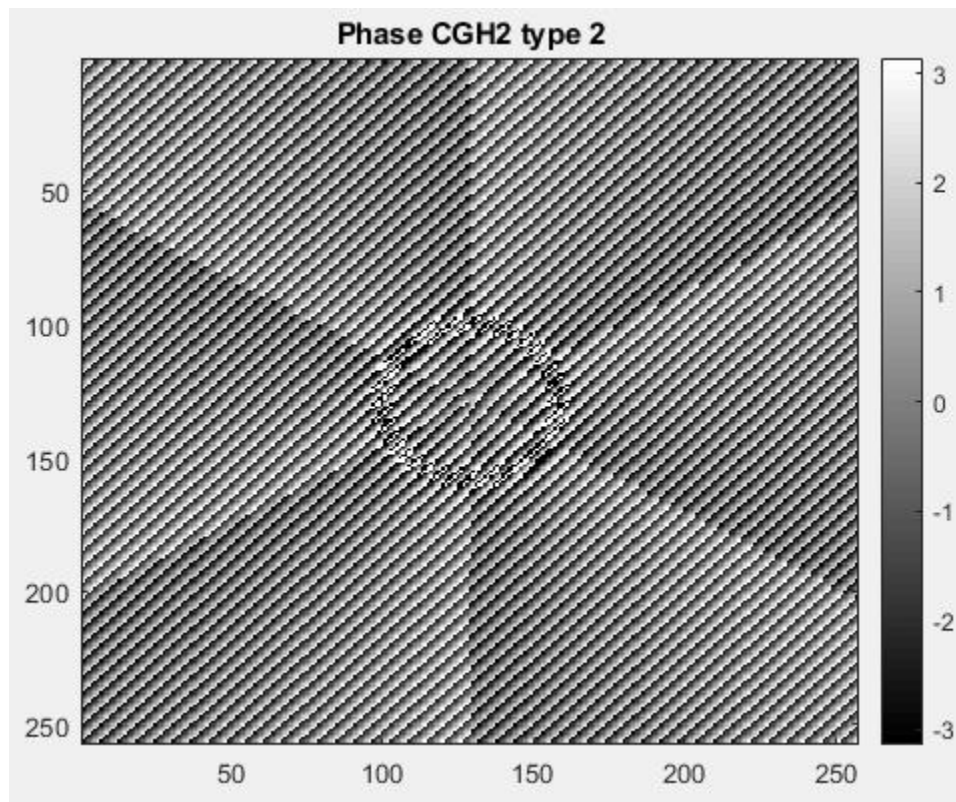


Figure 5.6: Phase distribution of the type 2 CGH that encodes LP₂₁ beam

The original LP₂₁ intensity is shown along with its replicate from the type 2 CGH in (Figure 5.7):

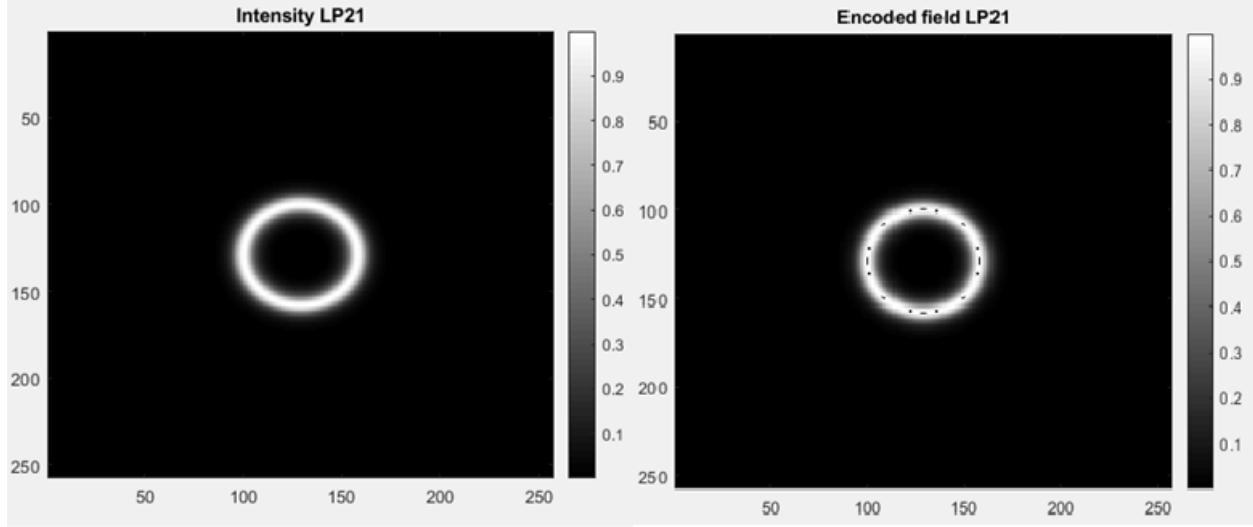


Figure 5.7: Intensity of the LP₂₁ beam and its replicate with the type 2 CGH

From (Figure 5.7), we can see the beam was not exactly encoded, we can also see some distortions. In Section 5.3, we will calculate the signal to noise ratio (SNR) of the encoded beam to quantify the quality of the encoding in terms of matching the original or ideal beam. We tried another type of CGH for encoding the beam; i.e. the type3 CGH. In this case, the phase modulation of the type 3 CGH is given by:

$$\Psi(\theta, a) = f(a)\sin(\theta) \quad (5.13)$$

Similar to the type2 CGH-, we started with the LG₂₁ beam to see if we can encode it with the type3 of CGH. We calculated the encoding condition for LG₂₁ by substituting Eq. (5.13) into Eq. (5.3) and obtained:

$$J_2[f(a)] = Aa(x, y) \quad (5.14)$$

where $A = 0.33$ corresponds to the maximum value of second-order Bessel function $J_2(x)$. In (Figure 5.8), we plot $f(a)$ versus a .

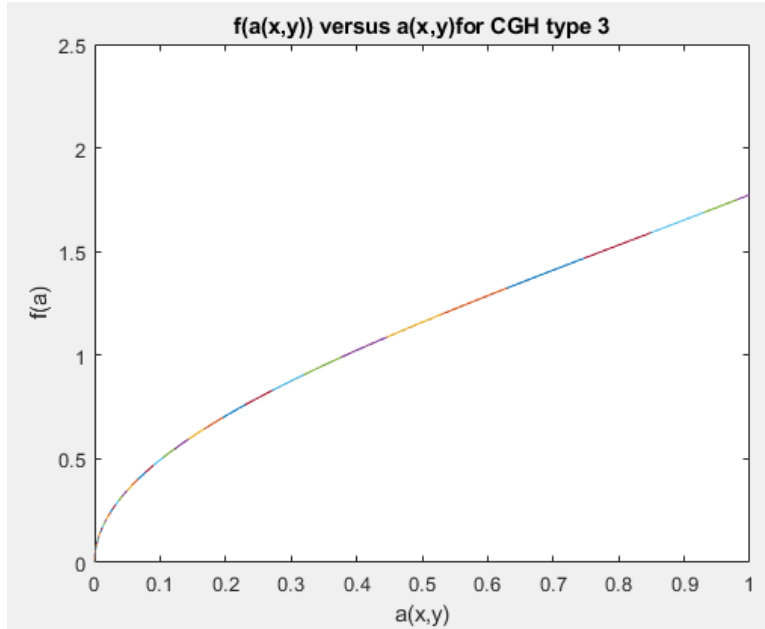


Figure 5.8: Function $f(a(x,y))$ versus $a(x,y)$ of the type3 CGH for a LG_{21} beam

The phase transmittance of the type3 CGH is

$$h(x, y) = \exp(jf(a)\sin(\theta)) \quad (5.15)$$

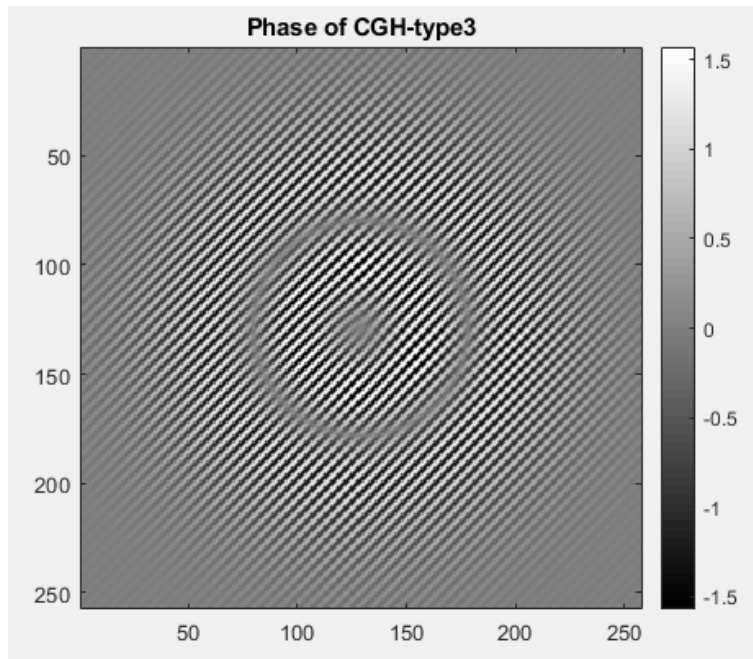


Figure 5.9: Phase distribution of the type3 CGH for encoding LG_{21} beam

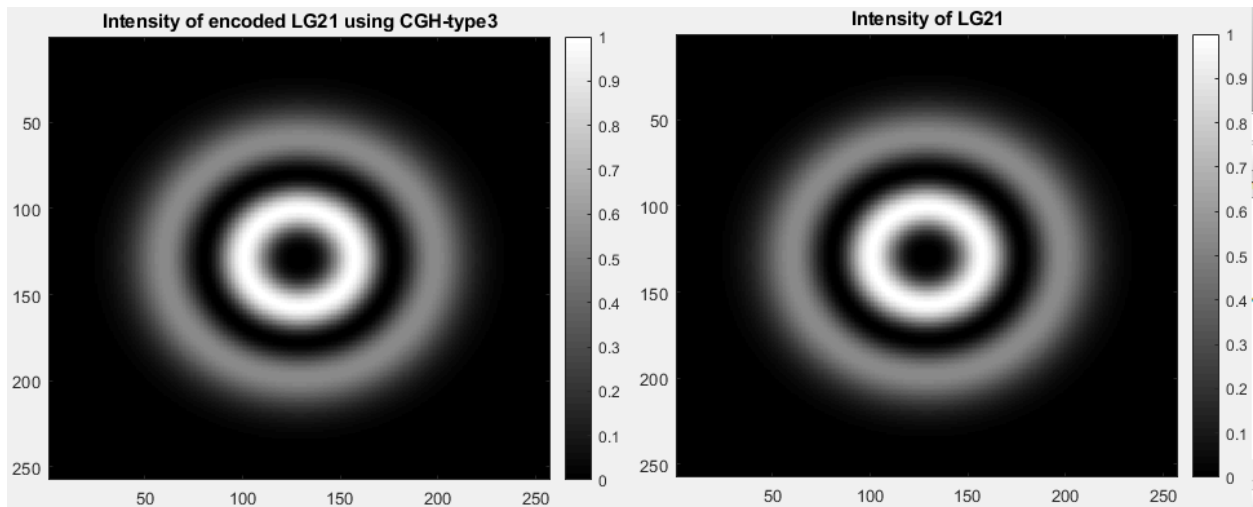


Figure 5.10: Intensity of LG_{21} beam and Intensity of the encoded LG_{21} with the type3 CGH

In (Figures 5.9 and 5.10) we depicted the phase of the CGH and intensity of the encoded beam respectively. Now, we tried to encode the desired beam LP_{21} with the type3 CGH. Its phase distribution for LP_{21} mode was shown in (Figure 5.11):

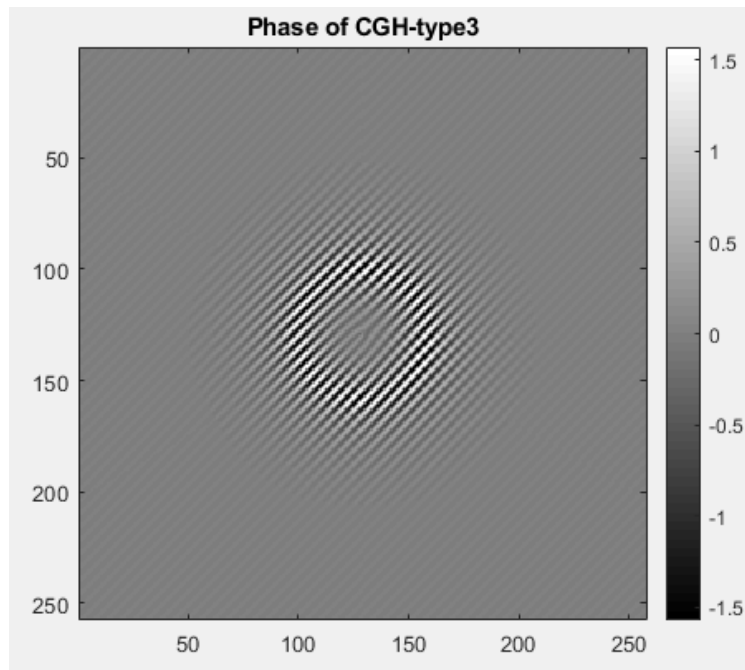


Figure 5.11: Phase distribution of the type3 CGH for encoding the LP_{21} beam

The encode LP₂₁ beam from the type3 CGH is shown in (Figure 5.12):

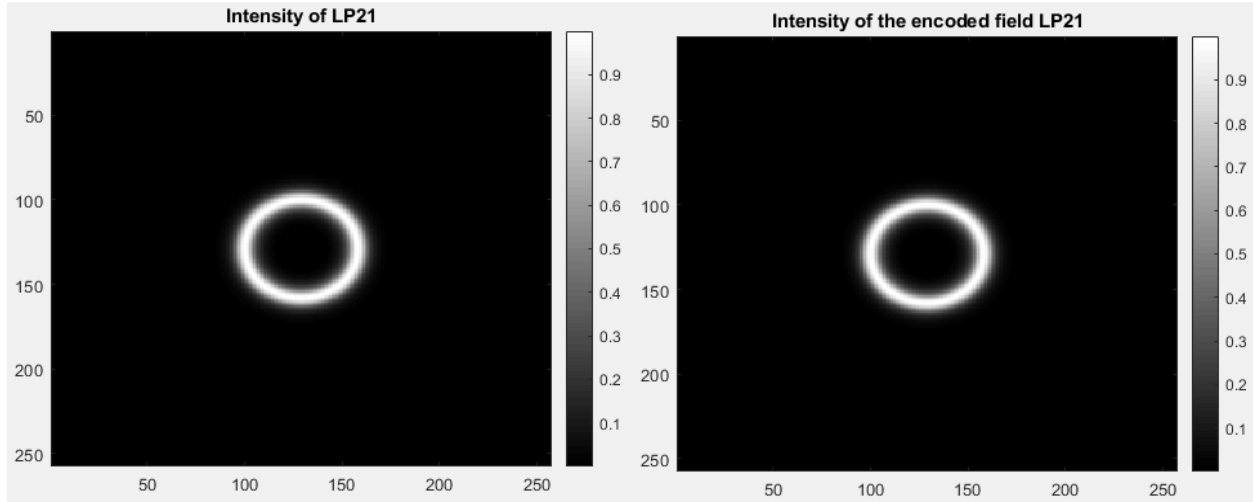


Figure 5.12: Intensity of original LP₂₁ beam and intensity of the encoded LP₂₁ with type3 CGH

5.3 Signal to Noise Ratio (SNR)

The signal-to-noise ratio (SNR) measures the ratio between the minimum intensity of the pixels that form the desired beam and the maximum intensity of the pixels that form the background. It is defined as:

$$SNR = \frac{\int \int_{D_s} |s(x, y)|^2 dx dy}{\int \int_{D_s} |s(x, y) - \beta s_t(x, y)|^2 dx dy} \quad (5.16)$$

where $s_t(x, y)$ is the field of the encoded beam formed by the CGH, $s(x, y)$ is the ideal or original beam, i and j are indices for each pixel in the horizontal and vertical directions respectively, D_s is the domain where encoding is performed, and β is defined as [55]:

$$\beta = \frac{\int \int_{D_s} Re\{s(x, y)s_t^*(x, y)\} dx dy}{\int \int_{D_s} |s_t(x, y)|^2 dx dy} \quad (5.17)$$

where β is a constant that is determined to minimize the error power, $Re\{.\}$ represents the real part of the function within brackets. SNR determines the robustness of the representational method under test. A high SNR indicates that for a wide range of exposure times, the encoded beam will

match exactly with the ideal beam. An $\text{SNR} \leq 1$ means either areas of the encoded beam will remain underexposed or areas of the background will be exposed; hence, a CGH with a low SNR value is unsuitable for masking or encoding the beam since any errant features appearing on the CGH could ruin the operation of encoding. (Figure 5.13) shows the result of SNR for type2 and type3 CGHs.

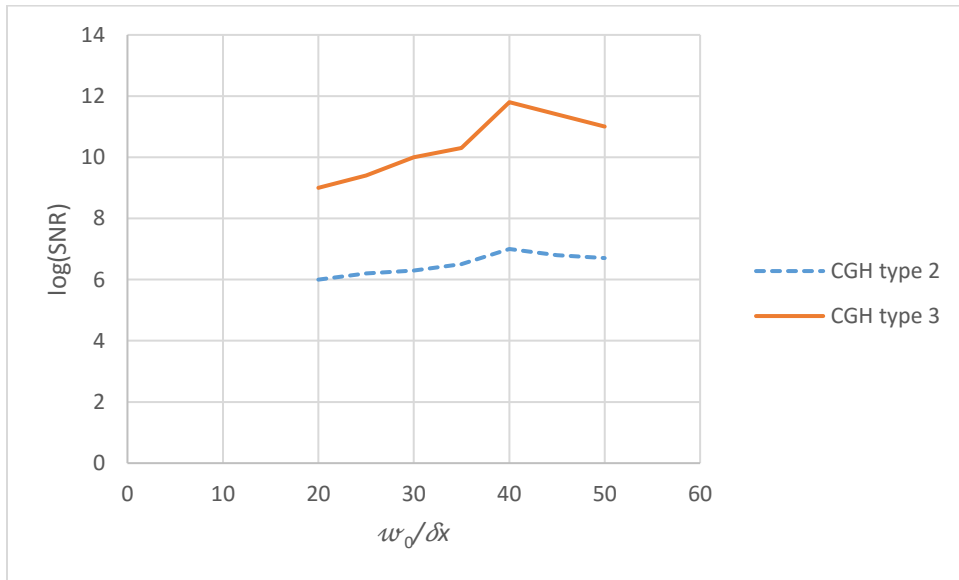


Figure 5.13: SNR versus the normalized waist $w_0/\delta x$ for type 2 and 3 CGHs for encoding LP_{21} beam

After we calculated the SNR for the reconstructed beam with type2 and type3 CGHs for the LP_{21} beam at different value of normalized waist $w_0/\delta x$ from 20 to 50 as shown in (Figure 5.13), we noticed a higher SNR values for CGH type3.

Since the CGHs are implemented with a pixelated phase spatial light modulator (SLM), we simply assume that the SLM pixel pitch δx is the same in the horizontal and the vertical axes with

squared pixels of side b . The reconstruction efficiency of CGH represents the power reduction in the CGH reconstructed signal due to pixelated SLM structure; it's given by

$$\eta = \frac{\int \int_{D_S} |s_t(x, y)|^2 dx dy}{\int \int_{D_S} |s(x, y)|^2 dx dy} \quad (5.18)$$

After we substitute the value of the reconstructed beam at $w_0/\delta x = 40$, the efficiency of CGH-type3 is found to be 0.87.

Chapter 6

Performance of the Vortex Modes Based Optical Communication System

A fiber optical system has components similar to those of optical communication systems. The optical source is either a semiconductor laser (LD) or light emitting diode (LED) that performs the electrical to optical conversion. The channel is an optical fiber cable while the receiver is a photodetector which converts an optical signal back to an electrical one and then further signal processing is carried out to demodulate into a baseband signal.

The choice for optical source mainly depends on application requirements for the optical communication systems (Long-haul communication or local area network). LDs have the advantage of high speeds, narrow spectral width, and high power. LEDs have the advantages of reliability, lower cost, long lifetime, and simplicity of design but they have a lower bandwidth compared to that of LD. In this section, we consider a 100kHz narrowband tunable continuous wave (CW) external cavity laser (ECL) as the transmitter.

At the receiver end, the main component is the photodetector, typically made of semiconductors. It converts light into electricity with the photoconduction. Several types of photodiodes include avalanche photodiodes or p-i-n photodiodes. Here, we consider (22 and 38-GHz) Photoreceivers [68]; (Figure 6.1) shows the overall diagram of a typical multi-channel optical communication system. As shown in the figure below, the overall diagram consists of five components: optical transmitters/receivers, dense wavelength division multiplexing (DWDM) multiplexer and demultiplexer for combining multichannel signals into a channel (the fiber C in Chapter 4), CGH for encoding and decoding signals onto the spatial carrier (LP_{21} mode), modulator and demodulator encoding and decoding signals onto the temporal carrier.

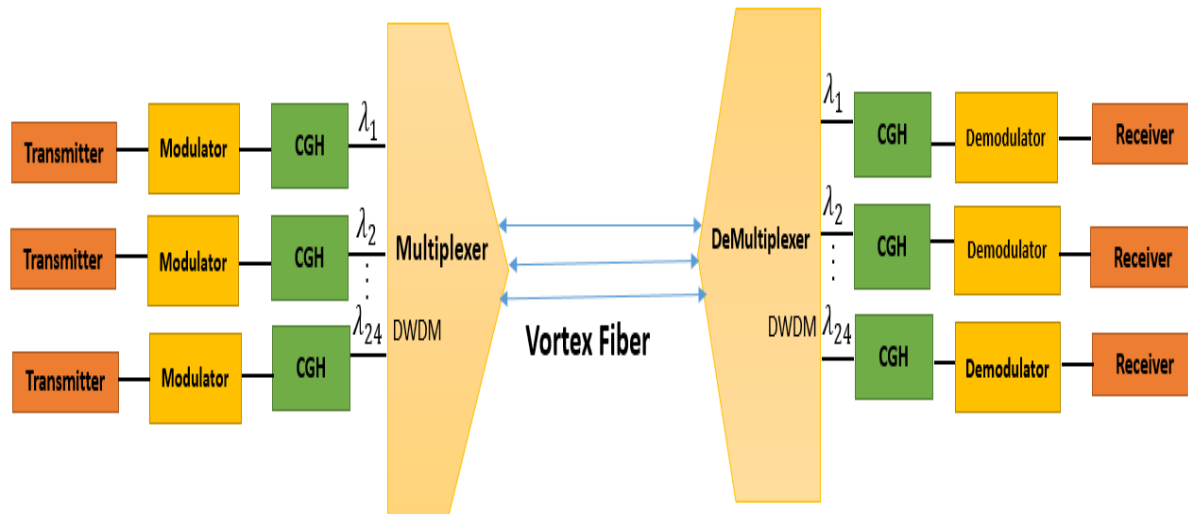


Figure 6.1: System diagram of a multi-channel optical communication system

6.1 Dense Wavelength Division Multiplexing (DWDM) technique

Dense wavelength division multiplexing (DWDM) technique is an optical technique for transmitting multiple channels into a fiber by multiplexing and demultiplexing signals of different wavelengths and hence a full utilization of the data capacity of a fiber. As DWDM system uses optical fiber for data transmission, it is more secure from tapping compared with other data transmission systems, e.g. satellite communication. According to ITU-T G.694-1 (a standard for the DWDM wavelength grid) [47], we can have 24 channels with 50GHz spacing, and the range of the channel would be from 1544.72nm to 1555.28nm. Based on the bandwidth of vortex fiber (fiber C), the total data rate of LP₂₁ mode is 3.6Tb/sec through 2km long, which can be supported by 24 channels with each channel carrying 150Gb/sec of data with 8 quadrature amplitude modulation (QAM) technique.

6.2 Mode Coupling

Mode coupling is caused by imperfections in the waveguide, such as changes in diameter, elliptical core deformations and random bends of the axis. These imperfections enable the transfer of energy from one ideal mode to another during propagation. This phenomenon has two important consequences. First, the spatial intensity profile inside the fiber changes along the length of the fiber as different mode groups are excited. Second, since power is transferred among modes with different velocities, the temporal response of the fiber changes [37,38,102,103] and signal power lost from one mode group appears as noise in another mod group.

Although Eq. (6.1) models the bend loss for a fiber with step index profile [42], it is useful to provide rough estimate the coupling losses caused by the bending in fiber C:

$$2\alpha = \frac{\pi^{1/2}\kappa^2 \exp\left[-\frac{2\gamma^3 R_{eff}}{3\beta^2}\right]}{2R_{eff}^{1/2}\gamma^{3/2}V^2 K_{m-1}(\gamma a)K_{m+1}(\gamma a)} \quad (6.1)$$

where $\gamma = \sqrt{\beta^2 - k_{clad}^2}$ and $\kappa = \sqrt{k_{core}^2 - \beta^2}$ are the field decay rates, in our case $\beta = 5.865 \times 10^6 \text{ rad/sec}$, $\gamma = 0.37 \times 10^6 \text{ rad/sec}$ and $\kappa = 0.818 \times 10^6 \text{ rad/sec}$; the effective bend radius $R_{eff} \approx 0.31 \text{ cm}$ [99], The K terms are modified Bessel functions, where $K_1(\gamma a) = 0.4$ and $K_3(\gamma a) = 4$, and the normalized frequency $V = 3.034$ for LP_{21} mode.

6.3 Optical Power Budget

The purpose of the power budget is to ensure that enough power will reach the receiver to maintain certain SNR for reliable communication. The optical power budget in an optical fiber communication system is the allocation of available optical power (launched into a given fiber by a certain source) among various loss mechanisms, such as coupling loss from fiber to CGH, and the fiber bending, fiber attenuation, and insertion losses from demultiplexer and multiplexer. In order to ensure that adequate signal strength (optical power) is available at the receiver [56]. Table 6.1 shows various loss sources for one channel only assuming that losses do not depend on frequency.

Parameter	Losses
Fiber Attenuation[7]	0.2 dB/km
Multiplexing + DeMultiplexing [96]	5.7 dB
Coupling Loss from CGH (both sides)	8 dB
Coupling Loss	0.665 dB/km

Table 6.1: Losses for the DWDM system

We analyzed below the projected performance for each channel of such a system with the vortex fiber (fiber C). In the receiver, in case if we use Ge APD, the received power is -1.78 dBm to

maintain the BER=10⁻⁶ using the NRZ coding format [41,67]; at the transmitter using neodymium laser, the transmitted power is -10dBm. Using Eq. (6.2), the length of the fiber is 20.9 km.

$$L(km) = \frac{P_t - P_r - \alpha_{de/mux} - \alpha_{CGH}}{\alpha_{total}} \quad (6.2)$$

$$\alpha_{total-fiber} (dB/km) = \alpha_{attenuation} + \alpha_{coupling loss} \quad (6.3)$$

where P_t and P_r are the transmitted and received power, respectively. $\alpha_{de/mux}$ is the losses from de/multiplexing, α_{CGH} is the losses from CGH, $\alpha_{attenuation}$ is the fiber attenuation and $\alpha_{coupling loss}$ is the loss from coupling, L is the length of the fiber.

The maximum data rate can be found by:

$$B_{max} = \frac{1}{4(\tau_{rx}^2 + \tau_{tx}^2)^{1/2}} \quad (6.4)$$

where τ_{tx} and τ_{rx} are the rise time of the transmitter and receiver, respectively. The rise time of the receiver and transmitter are both at 12.5 ps [68] and 1 ps [69,5]. Hence, the equivalent rise time for the receiver/transmitter pair is 0.43 ns. The value of $B_{max} = 19.936$ Gb/s, B based on the fiber is 18.75Gb/s, the maximum length would be 0.70623 km based on Eq. (6.6)

$$L_{max} = \frac{1}{4D_{channel}} \left(\frac{1}{B^2} - \frac{1}{B_{max}^2} \right)^{1/2} \quad (6.5)$$

where $D_{channel}$ is the total dispersion per each channel, the maximum length of the fiber is 20.9 km, based on the rise time of the receiver and transmitter, the length of the fiber is

Chapter 7

Conclusion

7.1 Conclusion

In this research project, we investigated one kind of novel fibers, known as vortex fiber, that has the potential to increase the capacity of future communication links. We first theoretically studied modes of MMF with a step index profile. Then we used the transfer matrix method (TMM) for finding the eigenvalues and eigenvectors of this vortex fiber to study its modes theoretically. We then compared results from TMM to those from the finite difference method (FDM) and calculated the differences in their effective indices (n_{eff}) for three mode groups. Their differences are on the order of 10^{-6} for approximated profiles with twenty layers and eighteen layers. We showed how many propagating modes in this fiber by formulating a fitting equation for the number of modes as a function of the fiber size from $35\mu m$ to $350\mu m$. Then we optimized the profile by considering 3 different profiles (fibers A, B, and C) and controlling the doping, i.e. changing the types and concentrations of materials in the core and cladding layers, with the objective of minimizing the material dispersion. We tweaked also the structure, e.g. shape of the profile, to minimize the waveguide dispersion by increasing the radius of the core region for guiding LP_{21} mode. Finally, we obtained the minimum overall GVD (the sum of material and waveguide dispersions) for LP_{21} mode in fiber C at $0.3432 ps/nm\cdot km$.

For fibers A, B, and C, we investigated fitting equations for the waveguide dispersion in LP_{01} , LP_{11} and LP_{21} modes and obtained reasonably small errors between numerical results and fitting equations.

In the second part of the project, we encoded the desired mode (LP_{21}) that can be propagated in the optimized profile (fiber C) by CGH technique and calculated encoded beams with type 2 and type 3 CGHs for LG_{21} and LP_{21} modes. Finally, we compared the encoded field to the original field for evaluating the effectiveness of CGHs in generating a vortex mode and found the efficiency of the type 3 CGH for encoding LP_{21} mode to be 0.87.

In the last part of this project, we considered DWDM as a technique for fully exploiting the huge fiber bandwidth by transmitting in a data rate of 3.15 Tb/sec with 32 channels. Then we estimated the power budget that accounted for various losses for the whole system and obtained the actual length of the fiber where we can apply $L=1.19\text{km}$.

7.2 Future Research

In this section, we address some of the limitations of multiplexing technique, as well as offer some of the ideas for the future investigations regarding reducing D_{modal} , thorough investigation of mode coupling, and simulations of the propagation of various mode groups.

One of the limitations of current results was that the value of D_{modal} was comparable to GVD, particularly for low GVD. To alleviate this constraint, the future work should be focused on investigating the reduction of the D_{modal} by enhancing the fiber.

On another side, if the fiber bending is considered, some other modes might be generated e.g. higher ordered modes (HOMs). In this case, we need to calculate both the inner mode couplings and the leakage due to the bending.

More ideas for future work is to propagate more than one mode rather than propagating the third mode only.

REFERENCES

- [1] Arrizón, Victor, et al. "Pixelated phase computer holograms for the accurate encoding of scalar complex fields." *JOSA A*, Vol. 24, No. 11, (2007): 3500-3507.
- [2] Alicia V. Carpentier, Humberto Michinel and Jose R. Salguero, "Making optical vortices with computer-generated holograms", *Am. J. Phys.* Vol. 76, No. 10: 916-921, October 2008.
- [3] Collier, R. J., Burckhardt, C. B., Lin, L. H., & Leith, E. N, "Optical holography", *Physics Today*, 1972.
- [4] N. Bozinovic, "Orbital angular momentum in optical fibers," Ph.D. dissertation, College of Engineering, Boston University, United States, 2013.
- [5] N. Bozinovic, Y. Yue, Y. Ren, M. Tur, P. Kristensen, H. Huang, A. E. Willner, S. Ramachandran, "Terabit-scale orbital angular momentum mode division multiplexing in fibers", *Science* 340, 2013, 1545–1548.
- [6] A. W. Lohmann and D. P. Paris, "Binary Fraunhofer holograms generated by computer", *Appl. Opt.* 6, 1967, 1739–1748.
- [7] Agrawal, Govind P. "Fiber-optic communication systems", Vol. 222. John Wiley & Sons, 2012.
- [8] Kao, K. C., and George A. Hockham. "Dielectric-fibre surface waveguides for optical frequencies." *Proceedings of the Institution of Electrical Engineers*. Vol. 113. No. 7: 1151–1158. IET Digital Library, 1966.
- [9] Marcuse, Dietrich, Andrew R. Chraplyvy, and R. W. Tkach. "Effect of fiber nonlinearity on long-distance transmission." *Journal of lightwave technology* Vol. 9, No. 1 (1991): 121-128.
- [10] Hecht, Eugene, "Physics: algebra/trig", Brooks/Cole Publishing Company, 2003.
- [11] Essiambre, René-Jean, and Robert W. Tkach. "Capacity trends and limits of optical communication networks." *Proceedings of the IEEE* 100.5 (2012): 1035-1055.
- [12] Sakaguchi, Jun, et al. "Space division multiplexed transmission of 109-Tb/s data signals using homogeneous seven-core fiber." *Journal of Lightwave Technology* 30.4 (2012): 658-665.
- [13] Berdagué, S., and P. Facq. "Mode division multiplexing in optical fibers." *Applied optics* 21.11 (1982): 1950-1955.
- [14] Gloge, D. "Optical power flow in multimode fibers." *Bell System Technical Journal* 51.8 (1972): 1767-1783.
- [15] Ryf, Roland, et al. "Mode-Division Multiplexing Over 96 km of Few-Mode Fiber Using Coherent 6 \times 6 MIMO Processing." *Journal of Lightwave technology* 30.4 (2012): 521-531.
- [16] Ramachandran, Siddharth, Poul Kristensen, and Man F. Yan. "Generation and propagation of radially polarized beams in optical fibers." *Optics letters* 34.16 (2009): 2525-2527.
- [17] Snyder, Allan W., and John Love. *Optical waveguide theory*. Springer Science & Business Media, 2012.
- [18] Saleh, Bahaa EA, and Malvin Carl Teich. *Fundamentals of photonics*. John Wiley & Sons, 2019.

- [19] Pedersen, Martin Erland Vestergaard, et al. "Impact of the scalar approximation on the prediction of the group velocity dispersion." *Journal of Lightwave Technology* 29.21 (2011): 3129-3134.
- [20] W. J. Dallas, "Computer-generated holograms", *The Computer in Optical Research*, B. R. Frieden, ed. (Springer-Verlag, 1980), pp. 4156–4165.
- [21] C. K. Hsueh and A. A. Sawchuk, "Computer-generated double-phase holograms", *Appl. Opt.* 17, 1978, 3874–3883.
- [22] N. Mait and K.-H. Brenner, "Dual-phase holograms: improved design", *Appl. Opt.* 26, 1987, 4883–4892.
- [23] Khonina, S. N., et al. "The phase rotor filter." *Journal of modern optics* 39.5 (1992): 1147-1154.
- [24] Padgett, M., et al. "An experiment to observe the intensity and phase structure of Laguerre–Gaussian laser modes." *American Journal of Physics* 64.1 (1996): 77-82.
- [25] He, H., N. R. Heckenberg, and H. Rubinsztein-Dunlop. "Optical particle trapping with higher-order doughnut beams produced using high efficiency computer generated holograms." *Journal of Modern Optics* 42.1 (1995): 217-223.
- [26] McGloin, David, Neil B. Simpson, and Miles J. Padgett. "Transfer of orbital angular momentum from a stressed fiber-optic waveguide to a light beam." *Applied optics* 37.3 (1998): 469-472.
- [27] Karimi, Ebrahim, et al. "Time-division multiplexing of the orbital angular momentum of light." *Optics letters* 37.2 (2012): 127-129.
- [28] Berkhout, Gregorius CG, et al. "Efficient sorting of orbital angular momentum states of light." *Physical review letters* 105.15 (2010): 153601.
- [29] R. W. Cohn and M. Liang, "Approximating fully complex spatial modulation with pseudorandom phase-only modulation", *Appl. Opt.* 33, 1994, 4406–4415.
- [30] Song, Rencheng, Jianxin Zhu, and Xuecang Zhang. "Full-vectorial modal analysis for circular optical waveguides based on the multidomain Chebyshev pseudospectral method." *JOSA B* 27.9 (2010): 1722-1730.
- [31] Yu-Chun, et al. "Improved Full-Vector Finite-Difference Complex Mode Solver for Optical Waveguides of Circular Symmetry." *Journal of lightwave technology* 26.13 (2008): 1868-1876.
- [32] Murshid, Syed, B. Grossman, and P. Narakorn. "Spatial domain multiplexing: A new dimension in fiber optic multiplexing." *Optics & Laser Technology* 40.8 (2008): 1030-1036.
- [33] Richardson, D. J., J. M. Fini, and Lynn E. Nelson. "Space-division multiplexing in optical fibres." *Nature Photonics* 7.5 (2013): 354.
- [34] Kettunen, Ville, et al. "Zeroth-order coding of complex amplitude in two dimensions." *JOSA A* 14.4 (1997): 808-815.
- [35] Mendlovic, David, et al. "Encoding technique for design of zero-order (on-axis) Fraunhofer computer-generated holograms." *Applied optics* 36.32 (1997): 8427-8434.
- [36] Arrizón, Victor. "Optimum on-axis computer-generated hologram encoded into low-resolution phase-modulation devices." *Optics letters* 28.24 (2003): 2521-2523.

- [37] Olshansky, Robert. "Mode coupling effects in graded-index optical fibers." *Applied optics* 14.4 (1975): 935-945.
- [38] D. Marcuse, "Theory of dielectric optical waveguides", Academic Press, 1991.
- [39] P. Yeh, A. Yariv, and E. Marom, "Theory of bragg fiber", *J. Opt. Soc. Am.*, vol. 68, no. 9, 1978, pp. 1196–1201.
- [40] P. Solarik, Z. Burian, I. Kasik, V. Matejec, J. Mrazek, and M. Hayer, "Dielectric annular core fiber for optical sensing", *Proc. SPIE*, vol. 6189, 2006, pp. 61 891R–61 891R–10.
- [41] Mikhailova, M. P., et al. "Sensitivity of a receiver using GaInAsSb/AlGaAsSb SAM avalanche photodiode for long-wavelength optical communication systems in the mid-infrared spectral range." *Photon Counting Applications, Quantum Optics, and Quantum Information Transfer and Processing II*. Vol. 7355. International Society for Optics and Photonics, 2009.
- [42] Schermer, Ross T., and James H. Cole. "Improved bend loss formula verified for optical fiber by simulation and experiment." *IEEE Journal of Quantum Electronics* 43.10 (2007): 899-909.
- [43] Yue, Yang, et al. "Mode properties and propagation effects of optical orbital angular momentum (OAM) modes in a ring fiber." *IEEE Photonics Journal* 4.2 (2012): 535-543.
- [44] Andrews, David L. *Structured light and its applications: An introduction to phase-structured beams and nanoscale optical forces*. Academic press, 2011.
- [45] Malitson, I. H. "Interspecimen comparison of the refractive index of fused silica." *Josa* 55.10 (1965): 1205-1209.
- [46] J. W. Fleming and D. L. Wood, "Refractive index dispersion and related properties in fluorine doped silica", *Appl. Opt.*, vol. 22, no. 19, Oct 1983, pp. 3102–3104.
- [47] ITU-T Recommendation G.694.1, (06/2002) "Spectral grids for WDM applications: DWDM frequency grid", <https://www.itu.int/rec/T-REC-G.694.2-200312-I>
- [48] Brückner, Volkmar. "To the use of Sellmeier formula", *Senior Experten Service (SES) Bonn and HfT Leipzig, Germany* 42, 2011, 242-250.
- [49] J. W. Fleming, "Dispersion in GeO₂–SiO₂ glasses", *Appl. Opt.*, vol. 23, no. 24, Dec 1984, pp. 4486– 4493.
- [50] H. Sunak and S. Bastien, "Refractive index and material dispersion interpolation of doped silica in the 0.6-1.8 μ m wavelength region", *Photonics Technology Letters, IEEE*, vol. 1, no. 6, June 1989, pp. 142–145.
- [51] A. Yariv, P. Yeh, "Photronics: Optical Electronics in Modern Communications", *Oxford Series in Electrical and Computer Engineering* (Oxford Univ. Press, New York, 2006)
- [52] E. Leith and J. Upatnieks, "Wavefront reconstruction with diffused illumination and three-dimensional objects", *J. Opt Soc. Am.*, vol. 54, 1964, p. 1295.
- [53] J. Goodman, "Introduction to Fourier Optics", 2nd ed. McGraw Hill Companies Inc., 1996.
- [54] J. G. D. Chu, J. Fienup, "Multiemulsion on-axis computer generated hologram", *Appl Opt*, vol. 12, no. 7, 1973, pp. 1386-1388.
- [55] Wikipedia, "vortex fiber", https://en.wikipedia.org/wiki/Optical_vortex

- [56] B. Mukherjee, "Optical Communication Networks", McGraw-Hill, New York, 2003.
- [57] Sharma, A. B., A-H. Al-Ani, and S. J. Halme. "Constant-curvature loss in monomode fibers: an experimental investigation." *Applied optics* 23.19 (1984): 3297-3301.
- [58] Bulow, H., et al. "Measurement of the maximum speed of PMD fluctuation in installed field fiber." OFC/IOOC. Technical Digest. Optical Fiber Communication Conference, 1999, and the International Conference on Integrated Optics and Optical Fiber Communication. Vol. 2. IEEE, 1999.
- [59] Arrizón, Victor, Guadalupe Méndez, and David Sánchez-de-La-Llave. "Accurate encoding of arbitrary complex fields with amplitude-only liquid crystal spatial light modulators." *Optics Express* 13.20 (2005): 7913-7927.
- [60] Yabre, G. "Comprehensive theory of dispersion in graded-index optical fibers." *Journal of lightwave technology* 18.2 (2000): 166.
- [61] Halil T. Eyyuboğlu "Mode coupling in vortex beams", *Optics & Laser Technology*, Elsevier, May 2018.
- [62] M. A. A. Neil, T. Wilson, and R. Juškaitis, "A wavefront generator for complex pupil function synthesis and point spread function engineering", *J. Microsc.* 197, 2000, 219–223.
- [63] Richardson, David J. "Filling the light pipe." *Science* 330.6002 (2010): 327-328.
- [64] Sakaguchi, Jun, et al. "Space division multiplexed transmission of 109-Tb/s data signals using homogeneous seven-core fiber." *Journal of Lightwave Technology* 30.4 (2012): 658-665.
- [65] Andrews, David L. *Structured light and its applications: An introduction to phase-structured beams and nanoscale optical forces*. Academic press, 2011.
- [66] Ryf, Roland, et al. "Mode-Division Multiplexing Over 96 km of Few-Mode Fiber Using Coherent 6×6 MIMO Processing." *Journal of Lightwave technology* 30.4 (2012): 521-531.
- [67] Trifkovic, Dragan. *Comparison of APD macromodels for accuracy, speed and implementation issues*. Diss. Carleton University, 2012.
- [68] "High-Speed Receivers Models 1591, 1592, 1580-A, 1544-A, 1580-B, 1544-B, 1484-A, and 1474-A High-Speed Detectors Models 1480-S, 1481-S, 1414,1004, 1014, 1444, and 1024", https://www.newport.com/medias/sys_master/images/images/h68/hba/8797113122846/High-Speed-Detectors-and-Receivers-User-s-Manual.pdf
- [69] Hora, Heinrich. *Plasmas at high temperature and density: applications and implications of laser-plasma interaction*. Vol. 1. Springer Science & Business Media, 2008.

Dua Al-Zaleq

Ph.D.

Electrical Engineering

University of Wisconsin Milwaukee

Interests: Optical Communication, Fiber and Quantum Optics, Electromagnetics, Antennas, Microwave Engineering, Optics and Photonics, Laser

Education

- 2014 - Feb 2019 **Ph.D. Electrical Engineering** – University of Wisconsin Milwaukee
Dissertation: “Spatial Multiplexing of Vortex Mode”
- 2012 - 2014 **M.Sc. Electrical Engineering** - University of Wisconsin Milwaukee
Thesis: “Orbital Angular Momentum Generation and Encoding of Optical Vortices using Computer Generated Hologram”
- 2004 - 2009 **B.Sc. Electrical Engineering** – Yarmouk University
Thesis: “Microstrip Elliptic-Function Low-Pass Filters Using Distributed Elements”

Teaching Experience

- Jan. 2017 – Jan. 2018 **Lecturer** - University of Wisconsin Milwaukee
EE150- Electronic Technology in the World around Us
EE335- Electronics 2
- 2012 - Present **Teaching Assistant** – University of Wisconsin Milwaukee

Course Name	Number	Teaching experience
Electrical Circuit 2	EE305	Lecture and Lab
Electrical Circuit 1	EE301	Lecture and Lab
Introduction to Electrical Engineering	EE306	Lecture and Lab
Electronics 1	EE330	Lecture and Lab
Electronics 2	EE335	Lecture and Lab
Digital Logic	EE354	Lecture & designed quizzes, assignments and exams
Introduction to Control System	ME 474	Lecture and Lab
Analytical Methods in Engineering	EE234	Lecture & designed quizzes, assignments and exams
Signals and Systems	EE310	Lecture
Fundamentals of Engineering	ME101	Lecture

Administrative Experience

- 2017 - Current **President of Optical Society of America (OSA)**
University of Wisconsin Milwaukee
- 2014 - 2017 **Vice President of Optical Society of America (OSA)**
University of Wisconsin Milwaukee
- 2016 - 2018 **Vice President of AAAEA, University of Wisconsin Milwaukee Chapter**
University of Wisconsin Milwaukee
- 2012- Current **Member of IEEE Association** - University of Wisconsin Milwaukee
- 2012 - Current **American Association for University Women - UW Milwaukee Chapter**
University of Wisconsin Milwaukee

Professional Experience

- 2009 - 2010 **Engineer in GSM and Wimax Department,**
Umniah telecommunication network
- 2010 - 2012 **Communication Engineer in Computer and Information Center,**
Networking Department, Jordan University of Science and Technology

Publications

- 2019 Du'a Alzaleq, Chiu Law. **"Increase Data Traffic Capacity by Designing a Novel Optical Vortex."** Journal of Lightwave Technology (Under Review)
- 2019 Du'a Alzaleq, Chiu Law. **"Spatial Multiplexing of Vortex Mode"** Journal of Optical Communications and Networking (Under Review)

Awards and Honors

- 2012 **Chancellor's Graduate Student Award** - University of Wisconsin Milwaukee
- 2013 **Chancellor's Graduate Student Award** - University of Wisconsin Milwaukee
- 2014 **Chancellor's Graduate Student Award** - University of Wisconsin Milwaukee

Computer Proficiencies:

System Programming - DSP programming using MathCAD, Digital Image programming using C++, Control systems designs using MATLAB.

Platforms- Worked on Linux and Windows Environment.

Languages- C, C++, and FORTRAN

Scripting Languages: HTML

Packages/Tools: COMSOL, MATLAB, MathCAD, AutoCAD, 3D Game Studio, LabVIEW, StressCheck, ModelSim SE, IPerf, and Microsoft Office.

Schematic Capture and PCB layout Software: LTspice/SwitcherCAD III, CircuitMaker, Altium Designer, ExpressPCB, ExpressSCH.

Professional References

- 1 **Dr. Chiu Law, Professor**
Department of Electrical Engineering and Computer Science
University of Wisconsin Milwaukee, 3200 N Cramer
st, Milwaukee, WI 53211, USA Phone: (414) 229-6203
Email: lawc@uwm.edu
<https://uwm.edu/engineering/people/law-ph-d-chiu/>
- 2 **Dr. Arash Mafi, Professor of Physics and Astronomy**
Department of Physics and Astronomy
CHTM 105A, MSC07 4220
1 University of New Mexico
Albuquerque, New Mexico 87131
Phone: (+1) 505 272-7942
Email: mafi@unm.edu
<http://mafi.unm.edu/>
- 3 **Dr. Suboh Alkushayni**
Department of Computer Science and Software
Engineering
University of Wisconsin Platteville, 241 MSB,
Platteville, WI 53818, USA Phone: 414-334-4069
Email: alkushaynis@uwplatt.edu